Summer 2020

Theoretical Investigation of the Biomass Conversion on Transition Metal Surfaces Based on Density Functional Theory Calculations and Machine Learning

Wenqiang Yang

THEORETICAL INVESTIGATION OF THE BIOMASS CONVERSION ON TRANSITION METAL SURFACES BASED ON DENSITY FUNCTIONAL THEORY CALCULATIONS AND MACHINE LEARNING

by

Wenqiang Yang

Bachelor of Engineering
Nanjing University of Science and Technology, 2012

Master of Engineering
University of Science and Technology of China, 2015

Submitted in Partial Fulfillment of the Requirements

For the Degree of Doctor of Philosophy in

Chemical Engineering

College of Engineering and Computing

University of South Carolina

2020

Accepted by:

Andreas Heyden, Major Professor

John R. Regalbuto, Committee Member

Gabriel A. Terejanu, Committee Member

Donna A. Chen, Committee Member

Salai C. Ammal, Committee Member

Melissa A. Moss, Committee Member

Cheryl L. Addy, Vice Provost and Dean of the Graduate School

DEDICATION

To my dear wife, my father, my mother, my sister and my son.

ACKNOWLEDGEMENTS

I want to thank my advisor, Prof. Andreas Heyden, who is the greatest advisor I have ever been working with. He knows how to advise a graduate student and how to make things go to the right direction when it is not going well. From him, I have learned a lot on writing, presenting and ways to smartly conduct research, without which, I could not this thesis. Most importantly, his passion on science, work ethics, hard-working spirit, profound knowledge and critical thinking set a great example of a good scientist. All I have learned from him will benefit my future career and shape me into a good researcher as him. I also want to show my sincerely thanks to my committee members: Dr. John R. Regalbuto, Dr. Dona A. Chen, Dr. Gabriel A. Terejanu, Dr. Salai C. Ammal and Dr. Melissa A. Moss, for their time and help in preparing my thesis. Besides, I am also grateful to all my project collaborators: Dr. Jesse Q. Bond from the Syracuse University who gave me a lot of good ideas from an experimental side, and Dr. Asif J. Chowdhury from Computer Science and Engineering at UofSC who built the machine learning model for adsorption energies prediction that was used in the chapter 4 of this thesis. A special thanks to Dr. Kareem Abdelfatah also from Computer Science and Engineering at UofSC for his great help in setting up the machine learning cycle which is the core of the work shown in chapter 4, and for his patient explanation in the working mechanism of the models.

I would also like to acknowledge my group members, Dr. Osman Mamun, Dr. Mohammad Saleheen, Dr. Yongjie Xi and Dr. Rajadurai Vijay Solomon, who helped me

in building the microkinetical modeling, liquid phase calculations and surface models for my project. I also extend my thanks to Charles Fricke, Dia Sahsah, Kyung-Eun You, Adam Yonge, Subrata Kundu and Nicholas Szaro for their support. I really enjoy working with them.

Great thanks to the Chemical Engineering Department staffs, Marcia Rowen, Loretta Hardcastle, Vernon Dorrell and Shawn Hagan, for their technical and administrative help.

Lastly, I would like to thank my dear wife Wen Xiong who is the greatest support behind me, and without whom I cannot overcome all the difficulties and hard times that I have met during my study here. I also thank my parents and sisters for their great support and encouragement. Specially, I want to thank my newborn baby, my little boy Leo, who gives me the power to face any difficulties and be prepared for the future.

ABSTRACT

During the past decades, heterogenous catalyzed conversion of biomass to hydrocarbons with similar or identical properties to conventional fossil fuels has gained significantly academic and industrial interest. However, the conventional heterogeneous catalysts such as sulfided $NiMo/Al_2O_3$ and $CoMo/Al_2O_3$ used have various drawbacks, such as short catalyst lifetime and high sulfur content of product. To overcome the limitations of the conventional sulfided catalysts, new catalysts must be developed, which requires a better understanding of the reaction mechanism of the biomass conversion. Based on density functional theory, in this thesis, we reported a computational calculation study of the reaction mechanism of the hydrodeoxygenation of propionic acid (our choice of model biomass molecules). For most of the times, however, biomass conversion is a very complicated process which usually have a very large reaction network, and thousands of intermediates and reaction steps are involved. Therefore, to theoretically identify the energy of those species by computational calculations is not realistic. We therefore also reported the potential of a combination of computational calculations and machine learning method to address the large reaction network of biomass conversion.

Based on first principles calculations, a full microkinetic model have been developed for the vapor and liquid phase hydrodeoxygenation of propionic acid over a Pt (111) surface. Calculations suggest that decarboxylation does not occur at an appreciable rate. In the vapor phase, decarbonylation products, propionaldehyde and propanol are all

produced at similar rates. However, in both liquid water and 1,4-dioxane, propanol and propionaldehyde are favored over decarbonylation products. While a condensed phase can shift the reaction rate and selectivity significantly, the dominant pathways towards the various products are hardly affected. Only for propionaldehyde production do we observe a shift in mechanism. A similar study was also conducted on the vapor and liquid phase hydrodeoxygenation of propionic acid on Rh (111) surface. Calculations suggest that both decarboxylation and decarbonylation do not occur at an appreciable rate in all reaction environments. Propanol and propionaldehyde are the main products and produced at similar rates in both vapor and liquid phases. Although a condensed phase can shift the reaction rate, the dominant pathways and selectivity towards the various products are hardly affected.

In a combination of density functional theory calculations and machine learning method, we proposed a retraining cycle to predict the reaction mechanism of the hydrodeoxygenation of propionic acid on transition metal surfaces and the catalyst activity. With proper metal descriptors and species descriptors being used, our model predicts almost the same rate controlling species and reaction rates as that from models based on DFT calculations. We conclude that the approach we proposed can be readily used to address the complicated biomass conversion chemistry at a DFT accuracy without the need to do full DFT calculations for the large reaction network involved.

TABLE OF CONTENTS

LIST OF TABLES

LIST OF FIGURES

CHAPTER 1

INTRODUCTION

During the past decades, many efforts have been devoted to renewable energy resources, such as wind, solar, geothermal, hydropower and biomass. Among them, biomass is the only renewable carbon source and thus one of the most promising alternative energy sources for liquid fuel and chemical production. But biomass have their own disadvantages, such as high viscosity, poor oxidation stability, low energy density, and high cloud point temperature. Therefore, conversion of biomass to hydrocarbons with similar or identical properties to conventional fossil fuels, known as "green diesel", is of significant academic and industrial interest. In recent years, hydrodeoxygenation (HDO), a process to convert triglycerides or fatty esters/acids obtained from lipid-rich biomass feedstock into liquid hydrocarbon fuels, has gained attention. However, the conventional heterogeneous catalysts used for the HDO process such as sulfided $NiMo/Al_2O_3$ and $CoMo/Al_2O_3$ have various drawbacks. For instance, short catalyst lifetime and high sulfur content in the final product have been found. To overcome the limitations of using conventional sulfided catalysts in biomass processing, new catalysts must be developed, which requires a better understanding of the HDO mechanism of triglycerides and organic esters/ acids on metal catalysts. The objective of my research is to understand the reaction mechanisms from an atomic level via density functional theory (DFT) calculations aiming to help design novel catalyst for biomass conversion.

This dissertation has been written in a manuscript style format which means that each chapter in this dissertation is an independent scientific publication. In chapter 2, based on microkinetic modeling and density functional theory calculations, we systematically investigated the hydrodeoxygenation of propionic acid on Pt (111) surface under both vapor and liquid phases. This article has recently (January 2020) been published as fully scientific article in Journal of Catalysis. In this work, both the dominant reaction pathways and the key rate controlling species has been identified for the hydrodeoxygenation of propionic acid on Pt (111) surface under both vapor and liquid phases. In all reaction environments, decarboxylation is not favored. In the gas phase, both decarbonylation products and propanol and propionaldehyde can be produced. However, propanol and propionaldehyde production is favored over decarbonylation products in liquid phase. Under both vapor and liquid phase conditions, the dominant pathway for decarbonylation is the direct path which starts with dehydroxylation of adsorbed propionic acid, followed by α-carbon dehydrogenation and then either direct decarbonylation or further dehydrogenation prior to decarbonylation. Propanol and propionaldehyde production also favor a direct formation pathway which starts with direct dehydroxylation and hydrogenation of the carbonyl group. Only the propionaldehyde production mechanism changes in liquid phase. Here, the propanol production is significantly favored such that propionaldehyde is primarily produced from dehydrogenated surface alcohol species. In liquid 1,4-dioxane and at 473 K, the conversion rate of propionic acid is predicted to increase by one order of magnitude. Higher temperatures further increase the solvent acceleration on the turnover frequency. In liquid water and at 473 K, the propionic acid consumption rate is not significantly

increased, primarily because of strong adsorption of propionic acid which leads to the surface being partially blocked by propionic acid. With increasing temperature, however, the TOF is dramatically increased in liquid water and becomes even larger than that in liquid 1,4-dioxane as the surface is much less covered by propionic acid at these temperatures. The rate of the reaction is solely controlled by the dehydroxylation of adsorbed propionic acid under both vapor and liquid phase conditions. The rate of the decarbonylation mechanism is barely affected by the solvents and the increase in propionic acid conversion due to the presence of a solvent primarily originates from an increase in the rate of propanol and propionaldehyde production. Thus, solvents can be designed to manipulate the selectivity of the HDO of organic acids.

In chapter 3 (second publication), based on the similar method we used in chapter 2, we systematically investigated the hydrodeoxygenation of propionic acid on Rh (111) surface under both vapor and liquid phases. In all reaction environments, both decarbonylation and decarboxylation are not favored demonstrating that Rh (111) surface may not be the active site for DCN and DCX reaction. Propanol and propionaldehyde production dominantly occur during the HDO of propionic acid on Rh (111) surface, and the dominant pathways for propanol and propionaldehyde production favor a direct formation pathway which starts with direct dehydroxylation and followed by the hydrogenation of the carbonyl group. The dominant pathways of the reaction remain unchanged in the liquid phase while the rate of the reaction was slightly increased by the solvent. Larger Rh cavity radius used in the liquid phase calculations further increase the solvent acceleration on the turnover frequency. Generally, the promotion effect of water is much stronger than 1,4-dioxane on the rate of the reaction. The rate of the reaction is

solely controlled by the dehydroxylation of adsorbed propionic acid under both vapor and liquid phase conditions. The selectivity of the main products (propanol and propionaldehyde) is almost the same in all reaction environments. Thus, solvents (at least water and 1,4-dioxane) cannot be designed to manipulate the selectivity of the HDO of organic acids over Rh (111) surface.

In chapter 4 (third publication), in a combination of density functional theory calculations and machine learning method, we proposed a retraining cycle to predict the rate of the reactions without the need to fully calculated the energies of all the reaction intermediates at a DFT level of accuracy. After several cycles, the key species that control the reaction rate has been accurately identified and recalculated at a DFT accuracy. With the key species included in the model, we predicted a reaction rate that agrees very well with the value from the models that based on pure DFT calculations.

In chapter 5, we made our conclusion on the work of this dissertations.

CHAPTER 2

UNRAVELING THE MECHANISM OF THE HYDRODEOXYGENATION OF PROPIONIC ACID OVER A PT (111) SURFACE IN VAPOR AND LIQUID PHASES[1]

[1] W. Yang, R.V. Solomon, J. Lu, O. Mamun, J.Q. Bond and A. Heyden. Journal of Catalysis, 2020, 381, 547-560.

Reprinted here with permission of publisher.

`

2.1 Abstract

Microkinetic models based on first principles calculations have been developed for the vapor and liquid phase hydrodeoxygenation of propionic acid over a Pt (111) surface. Calculations suggest that decarboxylation does not occur at an appreciable rate. In the vapor phase, decarbonylation products, propionaldehyde and propanol are all produced at similar rates. However, in both liquid water and 1,4-dioxane, propanol and propionaldehyde are favored over decarbonylation products. While a condensed phase can shift the reaction rate and selectivity significantly, the dominant pathways towards the various products are hardly affected. Only for propionaldehyde production do we observe a shift in mechanism. At 473 K, the propionic acid conversion rate is increased by one order of magnitude in liquid 1,4-dioxane relative to the gas phase. In liquid water, the conversion rate is similar to the vapor phase since adsorbed propionic acid blocks a large fraction of the surface sites.

Keywords: Propionic acid, Hydrodeoxygenation mechanism, Propanol, Propionaldehyde, Microkinetic modeling, Solvent effect, Lateral interaction

2.2 Introduction

During the past decades, increasing consumption of fossil fuels has caused growing environmental and climate concerns. As a result, many efforts have been devoted to renewable energy resources, such as wind, solar, geothermal, hydropower and biomass. Among them, biomass is the only renewable carbon source and thus one of the most promising alternative energy sources for liquid fuel and chemical production[1, 2]. Triglycerides, the main constituent of vegetable oils and animal fats, can be used to produce first generation biofuels such as fatty acid methyl and ethyl esters (FAMEs)

`

through a process called transesterification[3-5]. But FAMEs have their own disadvantages, such as high viscosity, poor oxidation stability, low energy density, and high cloud point temperature[3, 4]. Therefore, conversion of triglycerides and their fatty acids to hydrocarbons with similar or identical properties to conventional fossil fuels, known as "green diesel", is of significant academic and industrial interest[6]. In recent years, hydrodeoxygenation (HDO), a process to convert triglycerides or fatty esters/acids obtained from lipid-rich biomass feedstock into liquid hydrocarbon fuels, has gained attention[2, 7]. However, the conventional heterogeneous catalysts used for the HDO process such as sulfided $NiMo/Al_2O_3$ and $CoMo/Al_2O_3$ have various drawbacks[5, 8]. For instance, short catalyst life times and high sulfur content in the final product have been found[5, 8]. To overcome the limitations of using conventional sulfided catalysts in biomass processing, new catalysts must be developed, which requires a better understanding of the HDO mechanism of triglycerides and organic esters/ acids on metal catalysts.

Recently, we have studied the HDO of an organic acid model molecule (propionic acid) to C_2 hydrocarbons on different Pd and Ru transition metal surfaces based on first-principle calculations[9-14]. We found that the HDO of propionic acid is mainly associated with two major reaction mechanisms: (1) decarbonylation (DCN) and (2) decarboxylation (DCX). For all the metal surfaces investigated in our previous studies, the DCN path is favored over the DCX pathway. Besides DCN and DCX pathways, alcohols and aldehydes can also be produced during the HDO of propionic acid. For example, Chen et al.[15] found that Ru/C has a high selectivity to propanol in the HDO of propionic acid at a temperatures of around 400 K and high H_2 partial pressure (>20 bar). Unfortunately, to the best of our knowledge, there is little work reporting the mechanisms of alcohol and

`

aldehyde production in the HDO of propionic acid. In order to gain more insights into the mechanisms of the HDO of organic acids (such as propionic acid) on transition metal surfaces and to guide the design of metal catalysts, it is necessary to study multiple metal surfaces and include as many reaction mechanisms as possible in the reaction network. Pt catalysts have long been shown to have a high activity towards HDO reactions[16-19]. Interestingly, production of multiple reaction products appears favorable. For instance, Rachmady and Vannice have studied the vapor phase acetic acid hydrogenation over supported Pt catalysts and observed various products such as CO, CH_4, ethanol, ethane and ethyl acetate [19]. Similarly, Olcay et al. studied the aqueous-phase hydrogenation of acetic acid over transition metal catalysts and observed both ethanol and alkane products over Pt catalysts [20]. In contrast, Lugo-José et al. studied the vapor phase HDO of propanoic acid over Pt catalysts and found essentially 100% selectivity towards DCN and DCX products [21]. Clearly, the reaction conditions and environment appear to strongly affect the product selectivity and thus, Pt metal catalysts are an ideal model system for identifying rate and selectivity determining steps for the HDO of propionic acid towards DCN, DCX, alcohol and aldehyde production in various reaction environments.

In regards to solvent effects, a few studies have reported a significant effect of a solvent on the reaction mechanism, activity and selectivity of HDO reactions [10, 14, 22, 23]. For instance, Hoelderich et al. studied the deoxygenation of oleic acid (C18) over Pd/C catalyst in liquid water and found that water can change the selectivity towards C17 hydrocarbons by up to 20% [24]. Similarly, Behtash et al. found that in liquid water the rate of DCX is increased for the HDO of propionic acid and becomes competitive to the DCN over both Pd (111) and Pd (211) surfaces [10, 14]. Due to the increased activity of the Pd

`

surface in liquid water for C-CO_2 bond cleavage, activation of the C-C bond by dehydrogenation (C-H bond cleavage) prior to C-C bond cleave (a necessary step in the vapor phase) was found to be unnecessary in liquid water. Finally, Mamun et al. studied the solvent effect on the hydrodeoxygenation of levulinic acid over Ru catalysts and observed rate increases of 2-4 orders of magnitude in liquid water relative to 1,4-dioxane [25]. Thus, in this paper, we investigated the HDO mechanisms of propionic acid over Pt (111) under both gas and liquid phase conditions. Water and 1,4-dioxane have been selected as solvents as they are among the most often used solvents in both the academic and industrial communities. We aimed at determining the dominant reaction pathways and identifying the rate- and selectivity-controlling steps for the HDO of propionic acid under both vapor and liquid phase conditions. The solvent effect on the full microkinetic modelling results, such as reaction orders, apparent activation energies and turnover frequencies (TOFs) have also been discussed.

2.3 Method

2.3.1 Computational Methods.

All gas phase calculations were carried out using the Vienna Ab Initio Simulation Package (VASP)[26, 27] based on density functional theory (DFT) with the projector augmented wave (PAW) method[28]. The generalized gradient approximation (GGA) with the Perdew and Wang 1991 functional (PW91) was used to treat exchange correlation effects[29, 30]. An energy cutoff of 400 eV is used for all DFT calculations and the energy convergence criterion was set to 10^{-7} eV. All structures were relaxed until the Hellmann-Feynman force on each atom were smaller than 0.01 eV $Å^{-1}$. The optimized lattice constant of a Pt unit cell (3.976Å) is in good agreement with the reported experimental

`

value of 3.912 Å[31] and has been used for the construction of the Pt (111) surface model. To simulate the Pt surface, a $3 \times 2\sqrt{3}$ Pt (111) surface model was constructed with four Pt atom layers separated by a 15 Å vacuum gap. The dipole correction was applied to the direction perpendicular to the surface. For all surface calculations, the bottom two layers were fixed to their bulk positions while the top two layers were fully relaxed in all directions. In the vibrational frequency calculations, however, all metal atoms were fixed at their optimized positions. The Brillouin zone integration was sampled by 4×4×1 k-points for the surface using the Monkhorst-Pack scheme[32]. In order to precisely locate the transition states of the elementary reactions, a combination of the climbing image nudged elastic band (CI-NEB) method and the dimer method was used[33-36]. It should be noted that frequencies below 100 cm^{-1} were shifted to 100 cm^{-1} for the calculation of partition functions in order to minimize the errors associated with the harmonic approximation for small frequencies[12].

The solvent effect of a liquid is investigated using the implicit solvation model for solid surfaces (iSMS) method. Information about the iSMS method has recently been published, [23] and a convergence plot of the iSMS method with system size is provided in Fig. A.9 in the appendix A. The key point of this model is to include the long-range metal interactions through periodic-slab calculations within the framework of DFT calculations in the absence of a solvent and to consider the effect of the liquid as a localized perturbation that can be described by cluster models embedded in an implicit continuum solvent. We define a free energy function for an adsorbed surface intermediate on a periodic metal slab in liquid, $G^{liquid}_{surface+intermediate}$, using a simple subtraction scheme as follows:

`

$$G^{liquid}_{surface+intermediate} = G^{vacuum}_{surface+intermediate} + (G^{liquid}_{cluster+intermediate} - E^{vacuum}_{cluster+intermediate}) \quad (2.1)$$

where $G^{vacuum}_{surface+intermediate}$ is the DFT free energy (harmonic approximation for vibrational contributions) of the surface slab model in the absence of a solvent, $G^{liquid}_{cluster+intermediate}$ is the free energy of a metal cluster in the liquid built by removing selected metal atoms from the periodic slab model and removing the periodic boundary conditions (vibrational contributions are not considered), while $E^{vacuum}_{cluster+intermediate}$ is the DFT energy of the same cluster model without the solvent. The COSMO-RS implicit solvation model was used to compute $G^{liquid}_{cluster+intermediate}$ through the COSMOtherm program. Thermodynamic properties of the solvents are obtained from the COSMOtherm database at the BP/TZVP level of theory. For all the remaining structures, COSMO-RS input files have been generated from the COSMO calculations at the same level of theory. Given the uncertainty in the solvent parameters for the Pt metal atoms, the solvent calculations were repeated with a cavity radius that is ± 10% of the default Pt cavity. In this way, we study the sensitivity of our liquid phase results with respect to the most important Pt solvent parameter.

2.3.2 Microkinetic Modeling

Adsorption free energies of all intermediates, G_{ads}, have been calculated with a universal reference based on the following equations:

$$G_{ads} = G_{slab+intermediate} - G_{slab} - N_C \times E_C - N_H \times E_H - N_O \times E_O \quad (2.2)$$

$$E_H = 0.5 \times E_{H2} \quad (2.3)$$

`

$$E_C = E_{CH4} - 2 \times E_{H2} \quad (2.4)$$

$$E_O = E_{H2O} - E_{H2} \quad (2.5)$$

where $G_{slab+intermediate}$ is the free energy of the intermediate on the surface slab, G_{slab} is the free energy of the clean surface slab, and E_{CH4}, E_{H2O}, E_{H2} are the energy of the CH_4, H_2O and H_2 molecules, respectively. N_C, N_H and N_O are the number of C, H and O atoms in the intermediate. Based on the adsorption free energy defined above, the reaction energy and activation energy barrier can be calculated using the following equations:

$$\Delta G_i^{rxn} = \Sigma_j \nu_{ij} \times G_{ads,j}^{i} \quad (2.6)$$

$$\Delta G_i^{\ddagger} = G_{ads,i}^{\ddagger} - \Sigma\, G_{ads,i}^{R} \quad (2.7)$$

with ΔG_i^{rxn} and $\Delta G_i^{\ddagger}$ being the reaction free energy and activation free energy of reaction step i, respectively. While ν_{ij} and $G_{ads,j}^{i}$ are the stoichiometry coefficient and adsorption free energy of intermediates j in reaction step i, respectively. Finally, $G_{ads,i}^{\ddagger}$ and $G_{ads,i}^{R}$ are the adsorption free energy of the transition state and the sum of the adsorption free energies of the reactant of reaction step i, respectively.

For surface reactions, the forward reaction rate constant (k_{for}) can be calculated according to the transition state theory as,

$$k_{for} = \frac{k_B T}{h} e^{-\frac{\Delta G\ddagger}{k_B T}} \quad (2.8)$$

where k_B is the Boltzmann constant, h is Planck constant, T is the reaction temperature in Kelvin, and $\Delta G\ddagger$ is the zero-point corrected activation barrier for the forward reaction

`

obtained from DFT calculations. For adsorption processes, the reaction rate constant can be approximated by collision theory with a sticking coefficient of 1,

$$k_{for} = \frac{1}{N_0\sqrt{2\pi m_A k_B T}} \tag{2.9}$$

where N_0 is the number of sites per surface area (1.454×10^{19} m^{-2}) and m_A denotes the molecular weight of adsorbent A. The reverse reaction rate constant (k_{rev}) is determined from the thermodynamic equilibrium constant K,

$$K = \frac{k_{for}}{k_{rev}} \tag{2.10}$$

In the presence of solvents, the free energy of reaction and activation barrier were calculated as,

$$\Delta G^{\ddagger}_{solvent,i} = G^{\ddagger}_{gas,i} + G_{TS}(solv) - G_{IS}(solv) \tag{2.11}$$

$$\Delta G^{rxn}_{solvent,i} = G^{rxn}_{gas,i} + G_{FS}(solv) - G_{IS}(solv) \tag{2.12}$$

where $G_{IS}(solv)$, $G_{FS}(solv)$, and $G_{TS}(solv)$ are the solvation free energies of the reactants, transition state and products of reaction step i, respectively, which were obtained from the COSMO-RS calculations.

With all the forward and reverse reaction rate constants specified, a mean-field microkinetic model was built for the normalized number of surface species i per surface metal atoms[37]. The surface coverage of each species is equal to the number of sites occupied by the species (see Table A.3 in the appendix A) times the normalized number of surface species i per surface metal atoms. Steady state surface coverages and rates are

`

obtained by using the Matlab ODE solver ode15s. No assumptions were made regarding the rate controlling steps in building our models.

2.3.3 Lateral interaction effects

The mean-field approximation of microkinetic models is typically derived under the assumption of no lateral adsorbate-adsorbate interactions. In particular, strong adsorbate-adsorbate attraction can lead to island formation which leads to an overestimation of the rate predicted by the mean-field approximation. At the same time, slight adsorbate-adsorbate repulsion can still be accommodated by mean-field models that consider the repulsive interaction within the free energy expression[38]. Without considering any lateral interactions, results from our mean-field microkinetic model showed that CO and H cover more than 95% of the Pt surface and the fraction of available free sites becomes exceedingly small. Since both adsorbed CO and H display significant lateral (repulsive) interactions, we should consider these interactions in our models. Here, we used a linear lateral interaction model for describing the effects of any high-coverage surface species (i.e., CO and H) on the free energy of any surface species in the microkinetic model. To describe the lateral interaction effect on activation barriers, we assumed that the transition states are affected as half the reactant and half the product:

$$G^i_{ads}(\theta_j) = G^i_{ads}(0) + a_{i,j} * \theta_j \quad (2.13)$$

$$G^i_{ads}(\theta_1, \dots, \theta_n) = G^i_{ads}(0) + \sum_{j \neq i}^{n} a_{i,j} * \theta_j \quad (2.14)$$

$$G^k_a(\theta_1, \dots, \theta_n) = G^k_a(0) + 0.5(G^k_{rxn}(0) - G^k_{rxn}(\theta_1, \dots, \theta_n) \quad (2.15)$$

where $G^i_{ads}(0)$ and $G^i_{ads}(\theta_j)$ are adsorption energies of species i on the clean surface and surface with θ_j sites covered by species j, respectively. $a_{i,j}$ is the lateral interaction

`

coefficient of species j to species i, and $G_a^k(\theta_1, \ldots, \theta_n)$ and $G_{rxn}^k(\theta_1, \ldots, \theta_n)$ are the activation and reaction free energy of step k with a surface covered by species i with coverage θ_i, respectively. All adsorption energies are calculated for all species at zero coverage and a coverage of 0.25 ML of CO and H. Table A.4 in the appendix A lists all the $a_{i,j}$ parameters.

2.4 Results and Discussion

A detailed reaction network for the HDO of propionic acid on Pt (111) along with the intermediates involved in various elementary reaction steps is shown in Fig. 2.1. The reaction network of the DCN and DCX in Fig. 2.1a is identical to our previous study on the HDO of propionic acid over Pd and Ru catalysts[9, 12, 13] while Fig. 2.1b shows the reaction network of propanol and propionaldehyde production. It is to be noted that we did not include the water-gas shift reaction in our reaction network that is able to reduce the CO partial pressure in the reactor. The water-gas shift reaction hardly occurs on Pt (111) but is believed to be catalyzed by Pt-oxide support interface sites[39, 40]. Thus, in the absence of a meaningful active site model for the water-gas shift, we are required to set the CO partial pressure to a practical value that leads to CO surface coverages and modeling results comparable to experimental observations. Fortunately, we found that our microkinetic modeling results are not very sensitive to the CO partial pressure due to the inclusion of lateral surface species interactions with CO in our microkinetic models (see section 3.2). Table 2.1 gives the reaction free energies and activation free energy barriers at a temperature of 473 K. The solvent effects of water and 1,4-dioxane are treated as corrections to the reaction and activation free energies, which are also provided in Table 2.1. In the following section, we will discuss the effects of solvents on various

`

elementary reaction steps. Then, we will discuss the results of our microkinetic reactor model under both gas phase and liquid phase conditions, which includes the turnover frequency (TOF), the dominant pathways for various products, selectivity towards different products and the effects of solvent on them. Results from our sensitivity analysis, which includes degree of rate control, degree of thermodynamic rate control, and degree of selectivity control, will be discussed thereafter. Finally, reaction orders and apparent activation energies under both gas and liquid phases will be reported.

2.4.1 Solvent effects on various elementary reaction steps

Water and 1,4-dioxane are chosen as solvents because they are usually used in experimental studies. The free energies at a temperature of 473 K of various steps are shown in Table 2.1 with the effects of solvents being shown as corrections to the reaction and activation free energies. Generally, solvents stabilize the adsorption of gas phase species in the range of 0.05 eV to 0.26 eV, and water has a stronger effect than 1,4-dioxane. For example, water stabilizes the adsorption of propionic acid and propionaldehyde adsorption by 0.26 and 0.22 eV, respectively, while the stabilization is 0.20 and 0.16 eV in 1,4-dioxane, respectively. However, solvents have a weaker effect on the reaction and activation free energies for surface reaction steps. Only for a few steps do we observe changes in free energy larger than 0.10 eV as a result of the presence of liquid water. For decarbonylation steps that produce CO, the reaction energies in water are around 0.1 eV more exergonic than in the gas phase as a result of CO adsorption being stabilized in water by 0.15 eV. For the CH_3CH_2COO α-carbon dehydrogenation step in water, the reaction and activation free energies decrease by 0.10 eV and 0.17 eV, respectively. Stabilization is a result of the carboxylate group changing its exposure to the

`

liquid phase during reaction (in the reactant state the carboxylate group points to the surface while in the product state it points at least partially to the liquid phase). For decarboxylation of CH_3CCOO in water, the reaction and activation free energies increase by 0.11 eV and 0.18 eV, respectively. Again, the solvent effect can be understood from the change in exposure of the carboxylate group to the liquid phase during reaction (in the reactant state the carboxylate group points to the liquid phase since the dehydrogenated α-carbon is strongly bound to the surface while in the product state CO_2 species is not partially charged anymore). For almost all other surface reactions, the change in free energy is smaller than 0.10 eV in liquid 1,4-dioxane. The free energies calculated at ± 10% of the default COSMO Pt cavity are shown in Table A.1 and A.2 in the appendix A. Overall, the observed trends are very similar to those shown in Table 2.1. Interestingly, a larger Pt cavity radius leads to a larger solvent effect for adsorption processes and a smaller solvent effect for processes involving a change in exposure of the carboxylate group to the liquid phase. A more detailed discussion of the effects of solvents on the observed kinetics is presented in the following sections.

2.4.2. Models and Activity Results

The microkinetic model based on the reaction network shown in Fig. 2.1 was solved until steady state at temperatures of 473, 498, and 523 K. The gas phase partial pressure was set to 1 bar for propionic acid, 0.001 bar for CO gas, 0.1 bar for hydrogen and zero for all other gas phase molecules, i.e., low conversion conditions. We note that the partial pressures of H_2O and CO_2 have no effect on our results except that they might promote the water-gas shift reaction, which is not explicitly considered in our models. Also, the solvent fugacity of 1,4-dioxane and water was found not to affect our results

since the surface coverage of localized water and 1,4-dioxane was found to be small (Table A.3 in the appendix A). In the following, the reported turnover frequency (TOF) corresponds to the rate of consumption of propionic acid per surface Pt atom. Table 2.2 shows the TOFs and coverages of the most abundant intermediates at different temperatures under both gas phase and liquid phase conditions.

Under gas phase conditions and 473 K, the coverages of CO*, H* and free site are 26%, 32% and 42%, respectively. Surface coverages are not a strong function of temperature, although the CO* coverage decreases somewhat with increasing temperature. In the presence of liquid 1,4-dioxane, CO*, H* and free site remain the dominant surface species; although at 473 K, the propionic acid coverage becomes 16%, somewhat reducing the hydrogen and free site coverage. The surface coverage of CO* is increased to 47% in liquid 1,4-dioxane mainly due to solvent stabilization of CO* as discussed in section 3.1. This effect is even more pronounced in the presence of liquid water. Here, H is not an abundant surface intermediate with a surface coverage less than 10% at all investigated temperatures. In contrast, CO* covers nearly 50% of the surface sites. Due to the strong stabilization effect of water on adsorbed propionic acid, the coverage of propionic acid becomes 40% at 473 K, which leads to a decreasing coverage of free sites (7%). With increased temperature, the coverage of propionic acid decreases and more free sites become available for surface reactions to take place in water.

Under gas phase conditions, DFT predicts that the reaction has a low TOF of 1.79×10^{-6} s^{-1} at 473 K on a Pt (111) surface. This TOF increases significantly in liquid 1,4-dioxane with the acceleration increasing with temperature (factor 25 to 50 increase). At 523 K, we predict a TOF in liquid 1,4-dioxane of 8.93×10^{-4} s^{-1}. In contrast, liquid

`

water does not change the TOF significantly at 473 K relative to the gas phase (less than factor 3 increase) because CH_3CH_2COOH* and CO* block 89% of the surface sites (the free site coverage is only 7%). However, at higher temperatures in liquid water, the CH_3CH_2COOH* coverage is significantly reduced, and liquid water starts to accelerate the consumption of propionic acid. For instance, at 523 K the TOF is increased by two orders of magnitude (factor 154) compared to the gas phase, which is even three times larger than that computed in 1,4-dioxane. These results suggest that solvents can significantly affect the reaction kinetics of propionic acid HDO on a Pt (111) surface; however, the selection of an optimal solvent is strongly temperature dependent since solvents affect many processes, some of which accelerate while others decelerate the overall kinetics.

2.4.3 Dominant Pathways

2.4.3.1 Dominant Pathways for the DCN mechanism

There are basically two types of reaction pathways involved in the DCN mechanism as shown in Fig 1a, 2a and 3a: (1) pathways that start with dehydroxylation, CH_3CH_2COOH* + 3* -> CH_3CH_2CO*** + OH* and followed by either direct decarbonylation or one step of dehydrogenation prior to the decarbonylation, which will be denoted as direct-DCN-path1 and direct-DCN-path2, respectively, and (2) pathways that involve α–carbon dehydrogenation prior to the dehydroxylation step that precedes the decarbonylation, which will be named as indirect-DCN-path. The rates (in s^{-1}) of all elementary reaction steps involved in the DCN mechanism under both gas and liquid phases environments (calculated with default COSMO Pt cavity) are shown in Fig. 2.1a, 2.2a and 2.3a, respectively.

`

As shown in Fig. 2.1a, under vapor phase conditions, the direct-DCN-path2 has a rate of 8.21×10^{-7} s^{-1} which is more than two orders of magnitude larger than that of the indirect-DCN-path and around 8 orders of magnitude larger than that of the direct-DCN-path1, i.e., the direct-DCN-path2 is the dominant DCN path. According to the rates shown in Fig. 2.1a, the DCN path starts with the direct dehydroxylation of adsorbed propionic acid ($CH_3CH_2COOH^*$ -> $CH_3CH_2CO^{***} + OH^*$), followed by one step of α–carbon dehydrogenation of $CH_3CH_2CO^{***}$ ($CH_3CH_2CO^{***}$ -> $CH_3CHCO^{**} + H^*$) forming CH_3CHCO^{**}, which will go in three possible reaction directions: (1) one step of dehydrogenation of β–carbon prior to the decarbonylation (CH_3CHCO^{**} -> $CH_2CHCO^{***} + H^*$) step followed by hydrogenation of the decarbonylation product CH_2CH^{***} to yield CH_2CH_2, (2) one more dehydrogenation step at the α–carbon of CH_3CHCO^{**} (CH_3CHCO^{**} -> $CH_3CCO^{***} + H^*$) followed by decarbonylation of CH_3CCO^{***} and hydrogenation/dehydrogenation of the DCN product CH_3C^* to the final product CH_2CH_2, or (3) decarbonylation of CH_3CHCO^{**} to CH_3CH^{**} (CH_3CHCO^{**} -> $CH_3CH^{**} + CO^*$) followed by hydrogenation of CH_3CH^{**} to the final product CH_3CH_3. These three reactions happen competitively on the surface with a rate of the same order of magnitude.

In liquid 1,4-dioxane, the rate of the direct-DCN-path2 is increased slightly (~20%) over the gas phase while the rate of the indirect-DCN-path is increased by almost a factor 6. However, the direct-DCN-path2 is still much faster than indirect-DCN-path and direct-DCN-path1, and no matter whether water or dioxane is presented as solvent, the rate of the direct-DCN-path1 is always negligible. Therefore, the dominant pathway of the DCN is not changed by 1,4-dioxane except that the decarbonylation of

`

CH_3CHCO^{**} (CH_3CHCO^{**} -> CH_3CH^{**} + CO^*), which is the product of the dehydroxylation step of the direct -DCN-path2, is slightly faster than the two competitive dehydrogenation steps (CH_3CHCO^{**} -> CH_2CHCO^{***} + H^*, CH_3CHCO^{**} -> CH_3CCO^{***} + H^*). Interestingly, the rate of the direct-DCN-path2 is decreased from 8.21×10^{-7} s^{-1} in the gas phase to 2.82×10^{-8} s^{-1} when water is present as solvent, while the rate of the indirect-DCN-path is increased to 6.25×10^{-9} s^{-1}, i.e., it becomes nearly competitive to the direct-DCN-path2. So, the dominant pathway of the DCN remains unchanged by the presence of liquid water, except that the decarbonylation of CH_3CHCO^{**} to CH_3CH^{**} (CH_3CHCO^{**} -> CH_3CH^{**} + CO^*) is faster than CH_3CHCO^{**} -> CH_2CHCO^{***} + H^* and CH_3CHCO^{**} -> CH_3CCO^{***} + H^*. Surprisingly, even though the TOF is increased in liquid, the rate of the DCN pathways does not increase significantly and even becomes smaller in water. This is because propanol and propionaldehyde production dominate the HDO of propionic acid in the liquid phase, and around 98% of the adsorbed propionic acid is hydrogenated to propanol and propionaldehyde, which will be further discussed in the following section 3.2.2.2.

Overall, under both vapor and liquid phase conditions, the dominant pathway of the DCN is the direct-DCN-path2, which first involves direct dehydroxylation of propionic acid, followed by α-carbon dehydrogenation, and then dependent on the reaction environment, either direct decarbonylation or dehydrogenation of the α- or β-carbon prior to decarbonylation. Finally, hydrogenation of the decarbonylation product will occur to finish the DCN path.

`

2.4.3.2 Dominant Pathways for Propanol and Propionaldehyde Production

As shown in Fig. 2.1b, 2.2b and 2.3b, we mainly considered three possible pathways for propanol production: (1) direct dehydroxylation of the adsorbed CH_3CH_2COOH*, followed by hydrogenation of the carbonyl group of CH_3CH_2CO*** to form propanol, which will be referred to as direct-propanol-path, (2) a dehydrogenation step (either α- or β-carbon) taking place prior to dehydroxylation, followed by a couple of hydrogenation steps after dehydroxylation forming propanol, which will be denoted as the indirect-propanol-path, and (3) hydrogenation of the produced propionaldehyde to propanol. We intentionally neglect this third pathway in our discussion here since it is much slower than the other two pathways according to Fig. 2.1b, 2.2b and 2.3b. Similarly, we also considered three possible pathways for propionaldehyde production: (1) direct dehydroxylation of the adsorbed CH_3CH_2COOH forming a single hydrogen deficient aldehyde (CH_3CH_2CO***), followed by one hydrogenation step to form propionaldehyde on the surface, which will be referred as direct-aldehyde-path, (2) dehydrogenation of one hydrogen deficient propanol that is produced in the direct-propanol-path to form propionaldehyde, i.e., CH_3CH_2COOH* -> CH_3CH_2CO*** -> CH_3CH_2COH* -> CH_3CH_2CHOH* -> CH_3CH_2CHO*, which will be called indirect-aldehyde-path, and (3) dehydrogenation prior to dehydroxylation, followed by hydrogenation to propionaldehyde, which will also be neglected as it is much slower than the other two pathways as shown in Fig. 2.1b, 2.2b and 2.3b.

Under vapor phase conditions, the dominant pathways for propanol and propionaldehyde production are both direct formation pathways, which start with dehydroxylation of the adsorbed propionic acid (CH_3CH_2COOH* -> CH_3CH_2CO*** +

`

OH*). About 46% of the produced $CH_3CH_2CO^{***}$ follows a decarbonylation mechanism while the rest goes into two competing directions: (1) one carbon atom hydrogenation step to produce propionaldehyde on the surface and (2) hydrogenation of the oxygen atom of the carbonyl group of $CH_3CH_2CO^{***}$ forming a propanol-like intermediate $CH_3CH_2COH^*$ on the surface. The rates for these processes are 4.12×10^{-7} s^{-1} and 5.60×10^{-8} s^{-1}, respectively. $CH_3CH_2COH^*$ can be further hydrogenated to $CH_3CH_2CHOH^*$. About 33% of $CH_3CH_2CHOH^*$ is further hydrogenated to propanol while about 67% of $CH_3CH_2CHOH^*$ is dehydrogenated to propionaldehyde ($CH_3CH_2CHO^*$). As shown in Table 2.3, the overall selectivity of the DCN, propanol and propionaldehyde production pathways in the vapor phase are predicted to be 46%, 18% and 36%, respectively, indicating that propanol and propionaldehyde can be produced during the HDO of propionic acid over Pt (111) surface. This observation agrees very well with our preliminary experimental results.

In both liquid water and 1,4-dioxane, the dominant pathway for propanol production is always the direct-propanol-path, while that for propionaldehyde is changed from the direct pathway to the indirect pathway. As shown in Fig. 2.2b and 2.3b, the first step for propanol and propionaldehyde production is still the direct dehydroxylation of adsorbed $CH_3CH_2COOH^*$ forming $CH_3CH_2CO^{***}$ on the surface. In the following, however, hydrogenation of $CH_3CH_2CO^{***}$ to propionaldehyde can no longer compete with hydrogenation of $CH_3CH_2CO^{***}$ to $CH_3CH_2COH^*$. In liquid water, the rates of these processes are 5.73×10^{-9} s^{-1} and 2.22×10^{-6} s^{-1}, respectively, while they are 1.29×10^{-6} s^{-1} and 4.25×10^{-5} s^{-1}, respectively, in 1,4-dioxane. Then, $CH_3CH_2COH^*$ will go through one hydrogenation step to form $CH_3CH_2CHOH^*$, which will partly be dehydrogenated to

`

propionaldehyde (from 23% to 30% depending on the solvent and the cavity of Pt as demonstrated by the selectivity shown in Table 2.3) with the remainder being hydrogenated to propanol. What's more, unlike in the gas phase where 46% of the CH_3CH_2CO*** species is decarbonylated, almost all the produced CH_3CH_2CO*** (around 98% in both liquid water and 1,4-dioxane) will be hydrogenated to CH_3CH_2COH*. Due to this change in dominant pathway, the selectivity of propanol increased dramatically in the condensed phase from 18% to around 70-75%, while the selectivity of DCN products dramatically dropped from 46% to around 2%. The selectivity of propionaldehyde is less sensitive to the reaction environment and 23 to 36% of the reaction flux goes towards propionaldehyde.

In summary, while the dominant pathway for propanol production remains unchanged in both gas and liquid phase environments, the dominant pathway for propionaldehyde production changed from a direct formation pathway to an indirect pathway. What's more, the solvent greatly promotes the rate of propanol production, which leads to a dramatic increase in the selectivity towards propanol and a decrease in selectivity of DCN products.

2.4.3.3 Dominant Pathways for the DCX

There are at least five potentially relevant reaction pathways identified from our earlier research on Pd and Ru catalysts: (1) dehydrogenation of the carboxyl group in adsorbed propionic acid prior to decarboxylation followed by hydrogenation steps to the final products ethane or ethene (CH_3CH_2COOH* → CH_3CH_2COO** → CH_3CH_2* → CH_3CH_3*), (2) same carboxyl group dehydrogenation as in pathway 1 followed by α-

`

carbon dehydrogenation before decarboxylation and hydrogenation of the decarboxylation product to ethane ($CH_3CH_2COOH^*$ → $CH_3CH_2COO^*$ → CH_3CHCOO^{***} → CH_3CH^{**} → $CH_3CH_2^*$ → $CH_3CH_3^*$), (3) this pathway is almost the same as pathway 2 except that the α-carbon is fully dehydrogenated prior to decarboxylation ($CH_3CH_2COOH^*$ → $CH_3CH_2COO^{**}$ → CH_3CHCOO^{***} → CH_3CCOO^{***} → CH_3C^* → $CH_3CH_2^*$ → $CH_3CH_3^*$), (4) in this pathway, one or two α-carbon dehydrogenation steps occur before dehydrogenation of the carboxyl group and decarboxylation ($CH_3CH_2COOH^*$ → $CH_3CHCOOH^{**}$ → CH_3CCOOH^{***} → CH_3CCOO^{***} → CH_3C^* →$CH_3CH_2^*$ → $CH_3CH_3^*$), (5) both α- and β-carbon dehydrogenation prior to dehydrogenation of the carboxyl group and decarboxylation.

No matter the reaction environment (vapor or liquid water or 1,4-dioxane), the dominant pathway for the DCX is always pathway 1. The rate of the DCX is very small and at least 3 orders of magnitude smaller than the DCN, propanol, and propionaldehyde production pathways, which agrees well with our preliminary experimental results. In condensed water and 1,4-dioxane, the DCX rate increases by at least one order of magnitude relative to the vapor phase but overall remains much smaller than the rate for propanol and propionaldehyde production. Thus, the selectivity towards DCX remains negligible in all reaction environments. Our prediction that the DCX pathway is not favored during the HDO of propionic acid, but that the rate increases in condensed phases agrees very well with previous studies on the HDO of propionic and acetic acid on other metal surfaces[10, 14, 20, 22, 41].

`

2.4.4 Sensitivity Analysis

To carry out a sensitivity analysis of our results, we computed Campbell's degree of kinetic rate control, DRC_i, and selectivity control, DSC_i, where i can be either a transition state or stable adsorbed intermediate[42, 43]. This enables discovery of the rate- and selectivity controlling steps and surface intermediates in the HDO of propionic acid over Pt (111). The degree of rate control and selectivity control can be calculated using the following equations.

$$DRC_i = \left(\frac{\partial \ln r}{\partial \frac{-G_i^0}{RT}}\right)_{G_{j\neq i}^0} \tag{2.16}$$

$$DSC_i = \left(\frac{\partial(\ln rP/rR)}{\partial \frac{-G_i^0}{RT}}\right)_{G_{j\neq i}^0} = \left(\frac{\partial(\ln rP)}{\partial \frac{-G_i^0}{RT}}\right)_{G_{j\neq i}^0} - \left(\frac{\partial(\ln rR)}{\partial \frac{-G_i^0}{RT}}\right)_{G_{j\neq i}^0} = DRC_{i,P} - DRC_{i,R} \tag{2.17}$$

where the partial derivative is taken holding constant the standard-state free energy of all other species G_j^0 (intermediates, transition states, reactants, and products). The value of DRC_i describes the relative increase in net rate due to the (differential) stabilization of the standard-state free energy for species i, holding all the other species' energies constant. $DRC_{i,P}$ and $DRC_{i,R}$ are the degrees of rate control of species i for the rates of making product P and consuming reactant R, respectively. The value of DSC_i describes the relative increase in net selectivity to product P from reactant R due to the (differential) stabilization of the standard-state free energy for species i (either a transition state or stable adsorbed intermediate state), holding all other species' energies constant.

`

2.4.4.1 Degrees of Rate Control

As shown in Table 2.4, reaction step 1 ($CH_3CH_2COOH^* + 3^* \rightarrow CH_3CH_2CO^{***} + OH^*$) solely controls the rate of the reaction (the rate of consumption of propionic acid) under both vapor and liquid phase conditions. The C-OH bond scission has also previously been identified as the rate controlling step in the HDO of propionic acid over Pd (111) and Ru (0001). Similarly, Olcay et al. and Pallassana and Neurock suggested that C-OH bond cleavage is rate controlling in the HDO of acetic acid on Pt (111), Pd (111) and Rh (111) surfaces[20, 44].

The degrees of thermodynamic rate control of the three most abundant surface intermediates H*, CO* and $CH_3CH_2COOH^*$ are listed in Table 2.5. In the gas phase, the values of the degrees of thermodynamic rate control for CO* and $CH_3CH_2COOH^*$ are 1.84 and 0.96, respectively, demonstrating that stabilizing the adsorption of CO* and $CH_3CH_2COOH^*$ can increase the rate of the reaction. In the case of CO*, this observation can be explained by the lateral interactions of CO* with other adsorbates. In contrast, H* has a large negative value of the degree of rate control (-3.04), which indicates that destabilizing the adsorption of H* and creating more free sites for the rate controlling reaction step 1 facilitates the HDO of propionic acid over Pt (111). In the condensed phase, the thermodynamic degrees of rate control change significantly. In liquid water, the H* coverage is small, and a small positive degree of thermodynamic rate control is observed. Also, the CO* and $CH_3CH_2COOH^*$ coverages are high such that negative degrees of thermodynamic rate control are computed. Somewhat similarly, in condensed 1,4-dioxane, both H* and CO* have negative degrees of thermodynamic rate control due to the significant surface coverage of these species while $CH_3CH_2COOH^*$

`

has a small positive degree of rate control that is sensitive to the Pt cavity radius in the solvation calculations, given the small but significant propionic acid coverage on the surface.

2.4.4.2 Degrees of Selectivity Control

The degrees of selectivity control of various key reaction steps for DCX, DCN, propanol, and propionaldehyde production are shown in Table 2.6, 2.7 and 2.8, respectively, and corresponding degrees of selectivity control of various key surface intermediates are shown in Table A.5, A.6, A.7, A.8, respectively, in the appendix A. Results shown in Table 2.6 indicate that the selectivity to the DCX path is solely determined by step 1 ($CH_3CH_2COOH^* + 3^* \rightarrow CH_3CH_2CO^{***} + OH^*$), i.e., deceleration of the dehydroxylation step increases the selectivity towards DCX most in all reaction environments. From the results of the degrees of thermodynamic selectivity control shown in Table A.5 in the appendix A, $CH_3CH_2COO^{**}$, $CH_3CH_2COOH^*$, H* and CO* are the key surface intermediates that have an apparent effect on the DCX path selectivity. Generally, stabilization of the adsorption of $CH_3CH_2COO^{**}$, which is the key species in the DCX path, can increase the DCX path selectivity. For the other three species, the effect varies dependent on the reaction environment. For instance, stabilization of the CO* adsorption in gas phase will decrease the DCX path selectivity, while in liquid phase, it will increase the selectivity towards the DCX path.

For DCN products, under gas phase conditions, stabilizing the transition state of reaction step 4 ($CH_3CH_2CO^{***} \rightarrow CH_3CHCO^{**} + H^*$), which competes with steps that lead to propanol and propionaldehyde production, increases the selectivity most.

`

Similarly, destabilizing the transition states for propanol and propionaldehyde formation (reaction step 51, 59 and 66) increases the selectivity towards DCN products. In liquid phase, the reaction flux through step 51 (direct-aldehyde-path) becomes small, so this transition state has a negligible effect on selectivity. In contrast, the propanol and propionaldehyde formation steps (steps 59 and 66) have an even more negative selectivity control towards DCN products in condensed phase. Also, stabilizing the transition state of step 4 continues to increase the selectivity towards DCN in liquid phase. This effect is even more pronounced in liquid 1,4-dioxane. Finally, steps 1 ($CH_3CH_2COOH^* + 3^* \rightarrow CH_3CH_2CO^{***} + OH^*$), 5 ($CH_3CHCOOH^{**} + * \rightarrow CH_3CHCO^{**} + OH^*$), and 8 ($CH_3CHCO^{**} + * \rightarrow CH_3CH^{**} + CO^*$) also affect the selectivity to DCN products somewhat in liquid water. The origin for the selectivity control of these steps is that the indirect-DCN-path (which involves dehydrogenation steps) becomes competitive against the direct-DCN-path in water. As shown in Table A.6 in the appendix A, stabilizing the adsorption of H*, $CH_3CH_2CO^{***}$ and CH_3CHCO^{**} will increase the selectivity towards the DCN path, while stabilizing the adsorption of those alcohol and aldehyde like intermediates ($CH_3CH_2CHOH^*$, $CH_3CH_2CH_2OH^*$ and $CH_3CH_2CHO^*$) will decrease the DCN path selectivity since it will promote the propanol and propionaldehyde production. The effect of CO adsorption on the selectivity varies depending on the reaction environment and the Pt cavity used in the solvent calculations such that we are unable to determine it reliably.

Next, for propanol production, Table 2.8 summarizes the degrees of selectivity control. Stabilizing reaction step 66 ($CH_3CH_2CH_2OH^* + * \rightarrow CH_3CH_2CHOH^* + H^*$) and decelerating step 59 ($CH_3CH_2CHOH^* + * \rightarrow CH_3CH_2CHO^* + H^*$) leads to increased

`

propanol production in all reaction environments. Step 66 facilitates direct propanol production and step 59 determines the relative reaction flux going towards propionaldehyde versus propanol. In the vapor phase, decelerating steps 4 and step 51 also increases the selectivity towards propanol. Step 4 is a key reaction step to produce DCN products while step 51 is instrumental for propionaldehyde production. The stability of these transition states plays only a minor role in condensed phases where the main reaction flux goes to propanol production. Table A.7 in the appendix A shows the thermodynamic selectivity control of various key species on propanol production. In the gas phase, stabilization of H* adsorption changes the selectivity towards alcohol production, while it has a much smaller effect in the condensed phase. In contrast, stabilization of CO* decreases the propanol selectivity in vapor phase, while it increases the selectivity towards alcohols in condensed phase. Stabilization of key intermediates in the DCN and aldehyde mechanism, $CH_3CH_2CO^{***}$ and $CH_3CH_2CHO^*$, decrease the selectivity towards propanol in the vapor phase. Given that in condensed phase the decarbonlyation and aldehyde production is less dominant, these species do not display a selectivity control in condensed phases. Also, stabilizing adsorbed propanol, $CH_3CH_2CH_2OH^*$, increases the selectivity towards propanol production in all reaction environments as it increases the reaction flux for the hydrogenation of $CH_3CH_2CHOH^*$ towards $CH_3CH_2CH_2OH^*$.

Finally, for propionaldehyde production, Table 2.8 summarizes the degrees of selectivity control. Again, step 59 and 66 are the key rate controlling steps in all reaction environments determining the relative reaction flux going towards propionaldehyde versus propanol. In the vapor phase, where DCN products are also produced, decelerating

`

step 4 ($CH_3CH_2CO^{***}$ -> CH_3CHCO^{**} + H*) and accelerating the direct aldehyde production step 51 ($CH_3CH_2CHO^*$ + 3* -> $CH_3CH_2CO^{***}$ + H*) also favors production of propionaldehyde. For the surface intermediates that have a significant effect on propionaldehyde selectivity, shown in Table A.8 in the appendix A, the stability of adsorbed H*, CO*, $CH_3CH_2CHOH^*$ and $CH_3CH_2CH_2OH^*$ are most relevant. Stabilizing H* adsorption increases the selectivity to propionaldehyde in vapor phase while it has practically no effect in the condensed phase. Stabilizing CO* reduces the selectivity in the vapor phase while it increases it in liquid water and 1,4-dioxane. Next, stabilizing $CH_3CH_2CHOH^*$ increases the selectivity in all environments, while stabilizing $CH_3CH_2CH_2OH^*$ decreases the selectivity in all environments, given that these species determine the relative reaction flux going towards alcohol and aldehyde.

2.4.5 Apparent Activation Barrier & Reaction Orders

In order to understand the temperature dependence of the rate of the reaction, apparent activation barriers (E_a) have been calculated using the following equation with a temperature range from 473K to 523K in all reaction environments.

$$E_a = k_B T^2 \left(\frac{dln(TOF)}{dT}\right)_{P,T} \tag{2.18}$$

To gain insights into the pressure dependence of the HDO of propionic acid on Pt (111) surface, reaction orders of H_2 and propionic acid have also been calculated using,

$$\alpha_i = \left(\frac{dln(TOF)}{dln(P_i)}\right)_{T,P_{j\neq i}} \tag{2.19}$$

`

Fig. 2.4a illustrates the reaction order with respect to H_2 in the vapor phase (-1.08), liquid 1,4-dioxane (-0.21) and liquid water (0.04). These reaction orders correlate (as expected) very well with the degrees of thermodynamic rate control of H* in the different reaction environments (see Table 2.5). Similarly, the reaction orders of propionic acid shown in Fig. 2.4b, 1.00 in the vapor phase, 0.15 in 1,4-dioxane, and -0.44 in liquid water, correlate with the degree of thermodynamic rate control of adsorbed propionic acid. While in the vapor phase the propionic acid coverage is very low, the coverage increases in condensed phase with a high coverage in liquid water, where adsorbed propionic acid blocks active sites for reaction. Fig. 2.5 illustrates the change in propionic acid reaction order with temperature in liquid water. With increasing temperature, the surface coverage of propionic acid decreases and thus, the reaction order increases until it reaches close to one at 573 K.

Finally, Fig. 2.6 displays Arrhenius plots for the consumption of propionaldehyde in various reaction environments. We compute apparent activation barriers of 0.99 eV, 1.28 eV and 3.03 eV in the gas phase, and liquid 1,4-dioxane and water, respectively. The large apparent activation barrier in water can again be explained by propionic acid inhibition at low temperatures which disappears with increasing temperature when the free site coverage increases (see Table 2.2 and the change in reaction order with respect to propionic acid as displayed in Fig. 2.4c).

2.5 Conclusions

Microkinetic models based on transition state theory and DFT have been developed for the investigation of the HDO of propionic acid over Pt (111) surface under

both vapor and liquid phase conditions. In all reaction environments, decarboxylation is not favored. In the gas phase, both decarbonylation products and propanol and propionaldehyde can be produced. However, propanol and propionaldehyde production is favored over decarbonylation products in liquid phase. Under both vapor and liquid phase conditions, the dominant pathway for decarbonylation is the direct path which starts with dehydroxylation of adsorbed propionic acid, followed by α-carbon dehydrogenation and then either direct decarbonylation or further dehydrogenation prior to decarbonylation. Propanol and propionaldehyde production also favor a direct formation pathway which starts with direct dehydroxylation and hydrogenation of the carbonyl group. Only the propionaldehyde production mechanism changes in liquid phase. Here, the propanol production is significantly favored such that propionaldehyde is primarily produced from dehydrogenated surface alcohol species. In liquid 1,4-dioxane and at 473 K, the conversion rate of propionic acid is predicted to increase by one order of magnitude. Higher temperatures further increase the solvent acceleration on the turnover frequency. In liquid water and at 473 K, the propionic acid consumption rate is not significantly increased, primarily because of strong adsorption of propionic acid which leads to the surface being partially blocked by propionic acid. With increasing temperature, however, the TOF is dramatically increased in liquid water and becomes even larger than that in liquid 1,4-dioxane as the surface is much less covered by propionic acid at these temperatures. The rate of the reaction is solely controlled by the dehydroxylation of adsorbed propionic acid under both vapor and liquid phase conditions. The rate of the decarbonylation mechanism is barely affected by the solvents and the increase in propionic acid conversion due to the presence of a solvent primarily originates from an

increase in the rate of propanol and propionaldehyde production. Thus, solvents can be designed to manipulate the selectivity of the HDO of organic acids.

2.6 ACKNOWLEDGMENTS

We gratefully acknowledge financial support from the U.S. Department of Energy, Office of Basic Energy Science, Catalysis Science program under Award DE-SC0007167 (most of the liquid phase calculations and models and some of the gas phase data) and the National Science Foundation under Grant No. DMREF-1534260 (some of the gas phase data and models). J.Q.B. acknowledges financial support from the National Science Foundation DMREF-1534269. Computational resources have been provided by the National Energy Research Scientific Computing Center (NERSC) which is supported by the Office of Science of the U.S. Department of Energy and in part by XSEDE under grant number TG-CTS090100. Computational resources from CASCADE cluster from Environmental Molecular Sciences Laboratory (EMSL) under Pacific Northwest National Laboratory (PNNL) are also used for the DFT calculations. Finally, computing resources from the USC High Performance Computing Group are gratefully acknowledged. We also gratefully thank the Writing Center of the University of South Carolina for providing suggestions in preparing this paper.

`

2.7 Tables and figures

Table 2.1: Reaction free energies in eV of all elementary reaction steps in the HDO of PAc on a Pt (111) surface at a temperature of 473 K in the vapor phase and in the presence of liquid water and 1, 4-dioxane.

#	Reaction		Gas		Water	1-4-dioxane	
		ΔG_{rxn}	$\Delta G^{\ddagger}$	$\Delta\Delta G_{rxn}$	$\Delta\Delta G^{\ddagger}$	$\Delta\Delta G_{rxn}$	$\Delta\Delta G^{\ddagger}$
0	CH_3CH_2COOH (g) + * -> CH_3CH_2COOH*	0.79	N/A	-0.26	N/A	-0.20	N/A
1	CH_3CH_2COOH* + 3* -> CH_3CH_2CO*** + OH*	0.52	0.70	0.08	0.06	0.08	0.05
2	CH_3CH_2COOH* + 2* -> $CH_3CHCOOH$** + H*	-0.21	0.72	-0.03	-0.06	0.02	-0.02
3	CH_3CH_2CO*** -> CH_3CH_2* + CO* + *	-0.74	1.47	-0.11	-0.06	-0.08	-0.05
4	CH_3CH_2CO*** -> CH_3CHCO** + H*	-0.29	0.71	-0.05	-0.09	-0.02	-0.04
5	$CH_3CHCOOH$** + * -> CH_3CHCO** + OH*	0.44	0.78	0.06	0.11	0.04	0.06
6	$CH_3CHCOOH$** + 2*-> $CH_2CHCOOH$*** + H*	-0.29	0.67	0.03	-0.02	0.02	0.01
7	$CH_3CHCOOH$** + 2* -> CH_3CCOOH*** + H*	-0.10	0.74	0.01	0.02	-0.01	-0.01
8	CH_3CHCO** + * -> CH_3CH** + CO*	-0.54	0.84	-0.10	0.01	-0.05	0.01
9	CH_3CHCO** + 2* -> CH_3CCO*** + H*	-0.31	0.65	-0.01	-0.02	0.01	0.00
10	CH_3CHCO** + 2* -> CH_2CHCO*** + H*	0.06	0.87	-0.03	-0.09	0.00	-0.04
11	$CH_2CHCOOH$*** + * -> CH_2CHCO*** + OH*	0.78	1.47	0.00	0.07	0.02	0.05
12	$CH_2CHCOOH$*** + * -> $CHCHCOOH$*** + H*	-0.07	0.77	-0.04	-0.09	-0.03	-0.04
13	CH_3CCOOH*** + * -> CH_3CCO*** + OH*	0.23	0.77	0.04	0.06	0.06	0.06
14	CH_3CCO*** -> CH_3C* +CO* + *	-1.18	0.75	-0.09	0.04	-0.07	0.01
15	CH_2CHCO*** + * -> CH_2CH*** + CO*	-0.89	0.69	-0.09	0.00	-0.06	0.00
16	CH_2CHCO*** + 2* -> $CHCHCO$**** + H*	-0.20	0.61	-0.01	-0.05	0.00	-0.01
17	$CHCHCOOH$*** + 2* -> $CHCHCO$**** + OH*	0.65	1.09	0.04	0.06	0.06	0.07
18	$CHCHCO$**** -> $CHCH$*** + CO*	-0.82	0.51	-0.11	0.02	-0.07	0.01
19	CH_2CH*** + * -> $CHCH$*** + H*	-0.13	0.69	-0.03	-0.07	-0.01	-0.04
20	CH_2CH_2** + 2* -> CH_2CH*** + H*	-0.05	0.69	-0.03	-0.08	-0.01	-0.04
21	CH_2CH*** -> CH_2C** + H*	-0.38	0.38	0.00	-0.03	0.00	-0.01
22	CH_3C* + 2* -> CH_2C** + H*	0.27	1.06	-0.02	-0.09	0.00	-0.05
23	CH_3CH** + 2* -> CH_2CH*** + H*	-0.29	0.51	-0.01	-0.11	-0.01	-0.07
24	CH_3CH** -> CH_3C* + H*	-0.94	0.25	0.00	-0.03	0.00	-0.02
25	CH_3CH_2* + 2* -> CH_3CH** + H*	-0.10	0.66	-0.03	-0.07	0.00	-0.03
26	CH_3CH_3* + *-> CH_3CH_2* + H*	-0.11	0.64	-0.01	-0.07	0.01	-0.02
27	CH_3CH_2* + 2* -> CH_2CH_2** + H*	-0.34	0.57	-0.01	-0.09	0.01	-0.04
28	CH_3CH_2COOH* + 2* -> CH_3CH_2COO** + H*	-0.41	0.31	0.11	0.07	0.07	0.03
29	CH_3CH_2COO** -> CH_3CH_2* + CO_2*	-0.09	1.49	-0.01	-0.01	0.00	0.02
30	CH_3CH_2COO** + 2* -> CH_3CHCOO*** + H*	0.47	1.24	-0.10	-0.17	-0.02	-0.05
31	$CH_3CHCOOH$** + 2* -> CH_3CHCOO*** + H*	0.27	0.75	0.04	0.01	0.03	0.01
32	$CH_3CHCOOH$** + 2* -> CH_3CH** + $COOH$**	-0.04	1.42	-0.04	-0.01	-0.02	-0.02
33	CH_3CHCOO*** -> CH_3CH** + CO_2*	-0.66	0.95	0.06	0.09	0.02	0.04
34	CH_3CHCOO*** + * -> CH_3CCOO*** + H*	-0.22	1.04	-0.05	-0.02	-0.02	-0.01
35	CH_3CCOOH*** + * -> CH_3CCOO*** + H*	0.15	0.90	-0.02	0.05	0.03	0.06
36	CH_3CCOOH*** + * -> CH_3C* + $COOH$**	-0.89	1.06	-0.05	0.02	-0.01	0.04
37	$CH_2CHCOOH$*** + 2*->CH_2CH*** + $COOH$**	-0.04	1.86	-0.08	-0.02	-0.04	0.00
38	CH_3CCOO*** -> CH_3C* + CO_2* +*	-1.38	0.79	0.11	0.18	0.03	0.09
39	$COOH$** -> CO_2* + H*	-0.35	0.45	0.14	0.04	0.07	0.01
40	$COOH$** -> CO* + OH*	-0.06	0.46	0.00	0.07	0.00	0.05
41	H_2O* + * -> OH* + H*	0.53	0.83	0.08	0.05	0.06	0.04
42	CH_3CH_3 (g) + * -> CH_3CH_3*	0.57	N/A	-0.05	N/A	-0.06	N/A
43	CH_2CH_2 (g) + 2* -> CH_2CH_2**	-0.27	N/A	-0.09	N/A	-0.05	N/A
44	H_2O (g) + * -> H_2O*	0.52	N/A	-0.16	N/A	-0.10	N/A
45	CO_2 (g) + * -> CO_2*	0.54	N/A	-0.09	N/A	-0.07	N/A

`

46	CHCH (g) + 3* -> CHCH***	-1.56	N/A	-0.16	N/A	-0.07	N/A
47	CO (g) + * -> CO*	-0.59	N/A	-0.15	N/A	-0.10	N/A
48	H_2 (g) + 2* -> H* + H*	-0.36	N/A	0.01	N/A	0.00	N/A
49	CH_3CHCHO*** -> CH_3CHCO** + H*	-0.92	0.08	0.04	0.03	0.01	0.01
50	CH_3CHCOH*** -> CH_3CHCO** + H*	-0.26	0.60	0.00	0.00	-0.01	-0.01
51	CH_3CH_2CHO* + 3* -> CH_3CH_2CO*** + H*	-0.87	0.18	0.12	0.09	0.08	0.06
52	CH_3CH_2COH* + 3* -> CH_3CH_2CO*** + H*	-0.25	0.04	0.04	0.02	0.04	0.02
53	CH_3CH_2CHO* + 3* -> CH_3CHCHO*** + H*	-0.24	0.69	0.03	-0.02	0.05	0.02
54	CH_3CHCH_2O*** + * -> CH_3CHCHO*** + H*	-0.67	-0.06	0.01	-0.02	0.01	-0.01
55	$CH_3CHCHOH$** + 2* -> CH_3CHCHO*** + H*	0.15	0.50	0.02	0.02	0.03	0.03
56	CH_3CH_2COH* + 3* -> CH_3CHCOH*** + H*	-0.28	1.07	0.00	-0.15	0.02	-0.08
57	$CH_3CHCHOH$** + 2* -> CH_3CHCOH*** + H*	-0.51	0.45	0.06	0.01	0.05	0.01
58	$CH_3CH_2CH_2O$* + * -> CH_3CH_2CHO* + H*	-0.63	0.02	-0.09	0.00	-0.06	0.00
59	CH_3CH_2CHOH* + * -> CH_3CH_2CHO* + H*	0.14	0.69	-0.07	0.00	-0.04	0.01
60	CH_3CH_2CHOH* + * -> CH_3CH_2COH* + H*	-0.48	0.28	0.01	0.02	0.01	0.02
61	$CH_3CH_2CH_2O$* + 3* -> CH_3CHCH_2O*** + H*	-0.20	0.69	-0.07	-0.12	-0.02	-0.05
62	CH_3CHCH_2OH** + 2*-> CH_3CHCH_2O*** + H*	0.24	0.58	0.08	0.08	0.07	0.06
63	CH_3CH_2CHOH* + 2* -> $CH_3CHCHOH$** + H*	-0.25	0.74	-0.06	-0.09	-0.02	-0.03
64	CH_3CHCH_2OH** + * -> $CH_3CHCHOH$** + H*	-0.58	0.51	0.07	-0.14	0.05	-0.09
65	$CH_3CH_2CH_2OH$* + * -> $CH_3CH_2CH_2O$* + H*	0.35	0.71	0.01	0.02	0.03	0.03
66	$CH_3CH_2CH_2OH$* + * -> CH_3CH_2CHOH* + H*	-0.41	0.46	-0.01	-0.04	0.00	-0.02
67	$CH_3CH_2CH_2OH$* + 2*-> CH_3CHCH_2OH** + H*	-0.09	0.78	-0.14	-0.16	-0.07	-0.08
68	$CH_3CH_2CH_2OH$ (g) + * -> $CH_3CH_2CH_2OH$*	0.66	N/A	-0.14	N/A	-0.12	N/A
69	CH_3CH_2CHO (g) + * -> CH_3CH_2CHO*	0.70	N/A	-0.22	N/A	-0.16	N/A
70	$C_4H_8O_2$ (dioxane) + 2* -> $C_4H_8O_2$**	1.07	N/A	-0.30	N/A	-0.22	N/A

Table 2.2: TOFs (s^{-1}) and surface coverage of the most abundant surface intermediates under vapor phase and liquid water and 1,4-dioanxe conditions on a Pt (111) surface at a propionic acid partial pressure of 1 bar, CO partial pressure of 0.001 bar and a H_2 partial pressure of 0.1 bar with temperatures ranging from 473 K to 523 K.

Phase	Temperature (K)	TOF (s^{-1})	θ_{H*}	θ_{CO*}	θ_{*}	θ_{Pac}
Gas	473	1.79×10^{-6}	0.26	0.32	0.42	0.00
	498	5.92×10^{-6}	0.26	0.27	0.47	0.00
	523	1.80×10^{-5}	0.27	0.22	0.51	0.00
water	473	2.27×10^{-6}	0.04	0.49	0.07	0.40
	498	1.68×10^{-4}	0.07	0.48	0.19	0.26
	523	2.77×10^{-3}	0.09	0.45	0.36	0.09
1, 4-dioxane	473	4.47×10^{-5}	0.11	0.47	0.25	0.16
	498	3.52×10^{-4}	0.14	0.43	0.41	0.02
	523	8.93×10^{-4}	0.16	0.37	0.47	0.00

Table 2.3: Product selectivity under gas and liquid phase conditions at a temperature of 473 K with results from solvation calculations at ±10% of the default COMSO Pt cavity radius being also shown.

	gas	water (default)	water (+10%)	water (-10%)	1, 4-dioxane (default)	1, 4-dioxane (+10%)	1, 4-dioxane (-10%)
S_{DCX}	N/A	N/A	0.01	0.01	N/A	N/A	N/A
S_{DCN}	0.46	0.02	0.01	0.01	0.02	0.02	0.02

`

$S_{propanol}$	0.18	0.74	0.75	0.69	0.71	0.70	0.68
$S_{propanal}$	0.36	0.24	0.23	0.30	0.27	0.28	0.30

Table 2.4: Degrees of rate control for various key steps determined from gas and liquid phase (calculations with ±10% of default COMSO Pt cavity radius are also included) at a temperature of 473 K.

	gas	water (default)	water (+10%)	water (-10%)	1, 4-dioxane (default)	1, 4-dioxane (+10%)	1, 4-dioxane (-10%)
Step 1	0.96	0.96	0.95	0.96	0.96	0.96	0.96
Step 4	N/A	-0.05	-0.10	-0.01	-0.03	-0.03	-0.01
Step 8	N/A	-0.02	-0.04	-0.01	N/A	N/A	N/A
Step 25	N/A	0.06	0.12	0.03	0.02	0.02	0.01

Table 2.5: Degrees of thermodynamic rate control for H*, CO* and CH_3CH_2COOH* from gas and liquid phase (±10% of default COMSO Pt cavity radius are also included) calculations at a temperature of 473 K.

Surface species	gas	water (default)	water (+10%)	water (10%)	1, 4-dioxane (default)	1, 4-dioxane (+10%)	1, 4-dioxane (-10%)
H*	-3.04	0.11	0.09	0.08	-0.63	-0.35	-0.21
CO*	1.84	-3.16	-3.28	-3.34	-2.21	-2.40	-2.61
PAC	0.96	-0.84	-1.02	-0.96	0.18	-0.05	-0.12

Table 2.6: Degrees of selectivity control for various key reaction steps that have impact on DCX path under gas and liquid phase conditions at a temperature of 473 K.

	Step 1	Step 5
Gas	-0.965	-0.002
Water (default)	-0.957	-0.004
Water (+10%)	-0.948	-0.010
Water (-10%)	-0.957	0.002
1,4-dioxane (default)	-0.973	0.013
1,4-dioxane (+10%)	-0.963	-0.002
1,4-dioxane (-10%)	-0.937	-0.001

Table 2.7: Degrees of selectivity control for various key reaction steps that have impact on the DCN path under gas and liquid phase conditions at a temperature of 473 K with N/A denoting values being smaller than 0.01.

	Step 1	Step 4	Step 5	Step 8	Step 51	Step 59	Step 66
Gas	N/A	0.49	N/A	0.01	-0.23	-0.13	-0.18
Water (default)	-0.10	0.46	0.10	0.24	N/A	-0.21	-0.62
Water (+10%)	-0.43	0.21	0.44	0.24	N/A	-0.12	-0.39
Water (-10%)	-0.22	0.20	0.23	0.36	N/A	-0.22	-0.50
1,4-dioxane (default)	-0.02	0.75	0.02	0.09	-0.03	-0.23	-0.67
1,4-dioxane (+10%)	-0.02	0.76	0.02	0.09	-0.02	-0.25	-0.64
1,4-dioxane (-10%)	-0.02	0.66	0.02	0.16	-0.02	-0.27	-0.64

`

Table 2.8: Degrees of selectivity control for various key reaction steps that have impact on the propanol and the propionaldehyde production path under gas and liquid phase conditions at a temperature of 473 K with the values in front of the brackets and the values in the brackets corresponding to the degrees of selectivity control for the propanol and the propionaldehyde production path, respectively.

	Step 4	Step 51	Step 59	Step 66
Gas	-0.41 [-0.41]	-0.23 [0.39]	-0.13 [0.22]	0.79 [-0.18]
Water (default)	-0.01 [-0.01]	N/A [0.01]	-0.24 [0.72]	0.25 [-0.71]
Water (+10%)	N/A [N/A]	N/A [N/A]	-0.22 [0.74]	0.23 [-0.73]
Water (-10%)	N/A [N/A]	N/A [N/A]	-0.30 [0.67]	0.30 [-0.67]
1, 4-dioxane (default)	-0.02 [-0.02]	-0.03 [0.08]	-0.23 [0.62]	0.28 [-0.68]
1, 4-dioxane (+10%)	-0.02 [-0.02]	-0.02 [0.06]	-0.27 [0.63]	0.30 [-0.67]
1, 4-dioxane (-10%)	-0.01 [-0.01]	-0.02 [0.04]	-0.28 [0.64]	0.31 [-0.66]

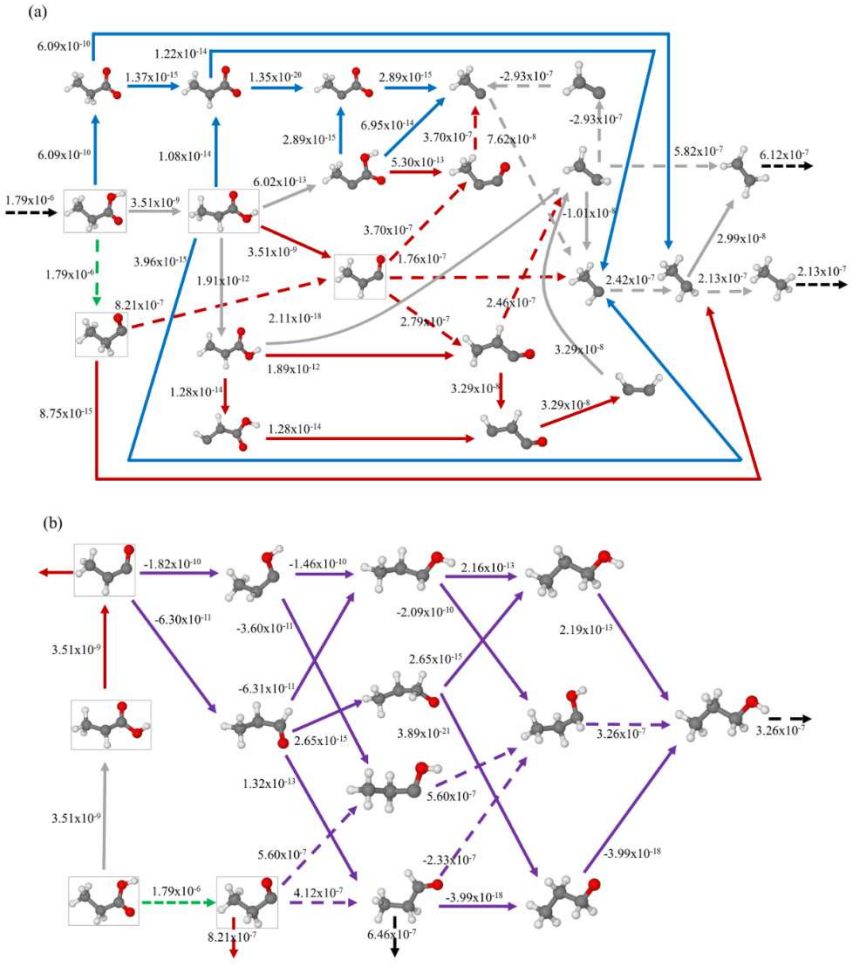

Figure 2.1: TOFs (s^{-1}) of (a) DCX and DCN reaction steps and (b) propanol and propionaldehyde production steps under vapor phase conditions at a temperature of 473 K and a gas partial pressure of propionic acid, CO and hydrogen of 1 bar, 0.001 bar and 0.1 bar, respectively.

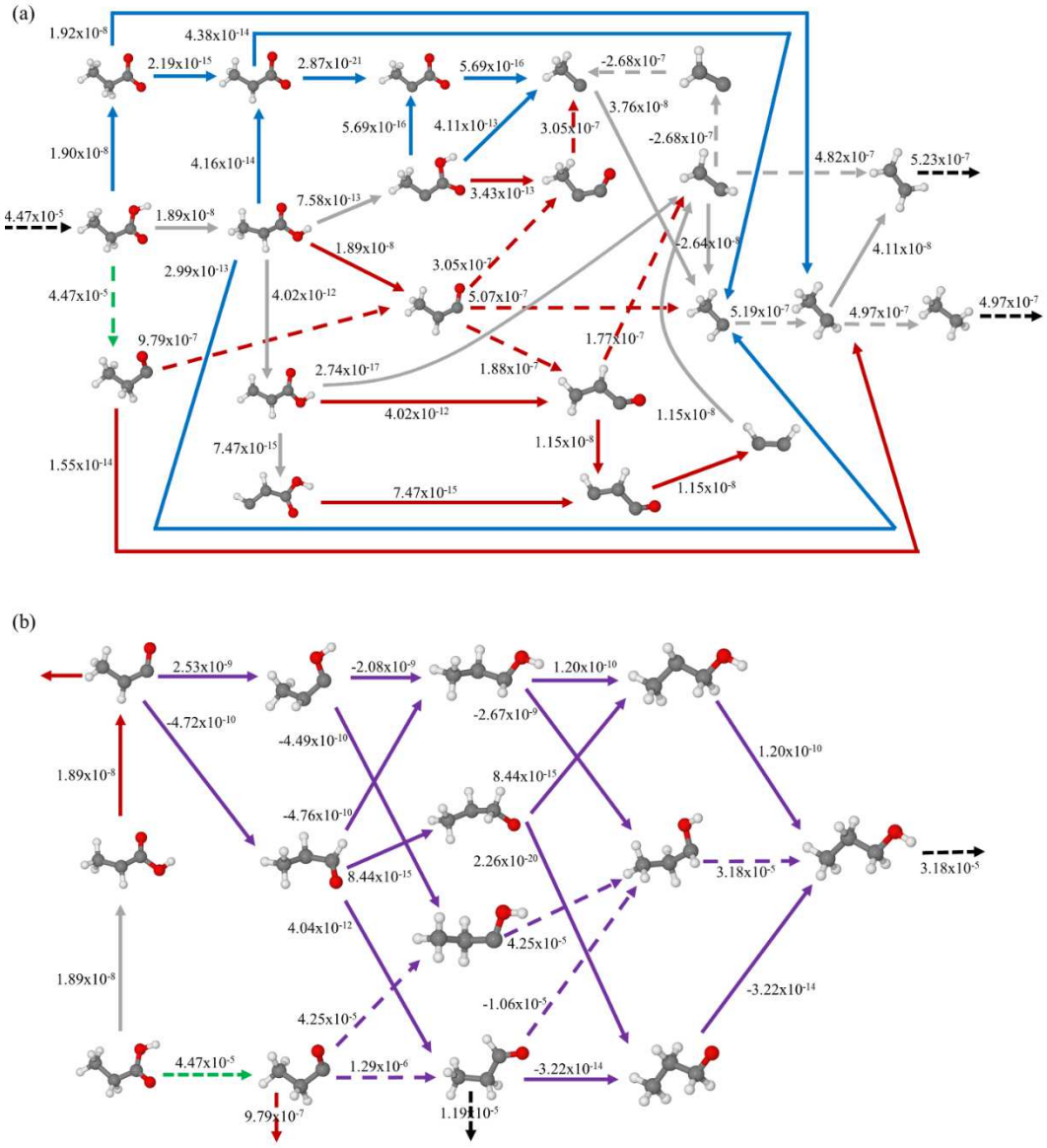

Figure 2.2: TOFs (s^{-1}) of (a) DCX and DCN reaction steps and (b) propanol and propionaldehyde production steps in liquid 1,4-dioxane at a temperature of 473 K and a gas partial pressure of propionic acid, CO and hydrogen of 1 bar, 0.001 bar and 0.1 bar, respectively.

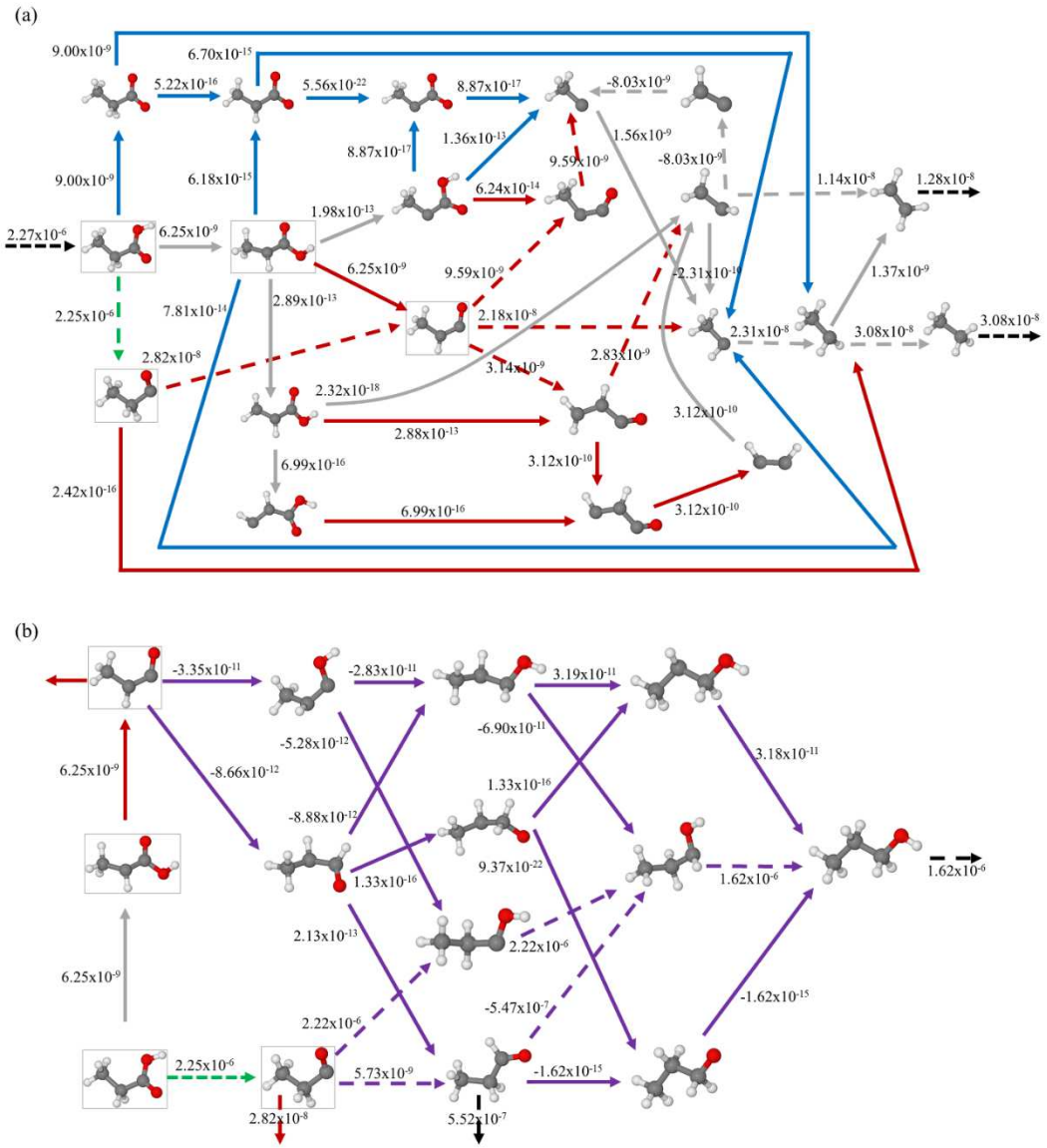

Figure 2.3: TOFs (s^{-1}) of (a) DCX and DCN reaction steps and (b) propanol and propionaldehyde production steps in liquid water at a temperature of 473 K and a gas partial pressure of propionic acid, CO and hydrogen of 1 bar, 0.001 bar and 0.1 bar, respectively.

`

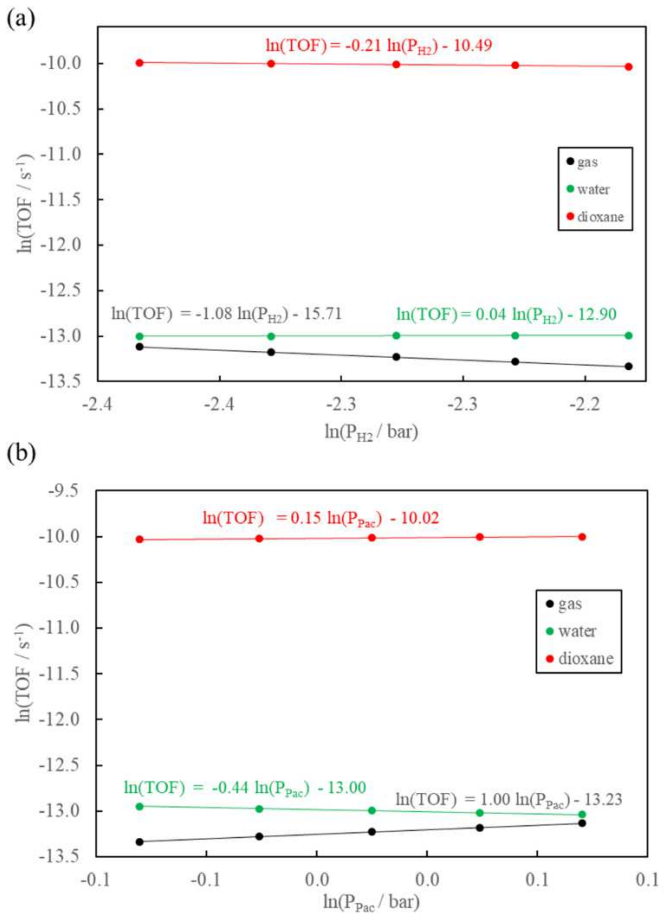

Figure 2.4: Reaction orders of (a) H_2 and (b) propionic acid at a temperature of 473 K and a gas partial pressure of propionic acid, CO and hydrogen of 1 bar, 0.001 bar and 0.1 bar, respectively.

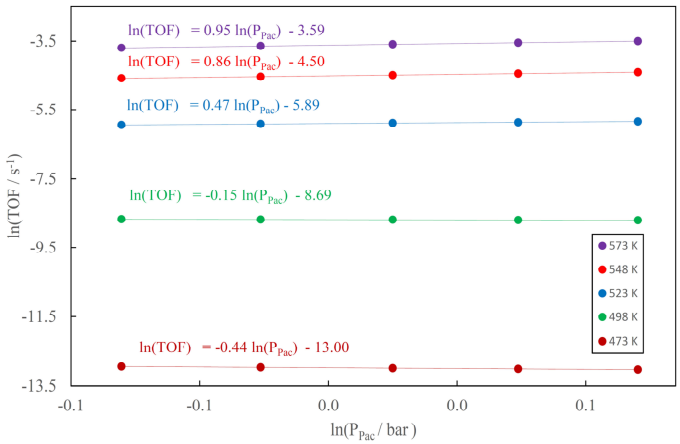

Figure 2.5: Reaction orders of propionic acid at various temperatures in the range of 473-573 K and a gas partial pressure of propionic acid, CO and hydrogen of 1 bar, 0.001 bar and 0.1 bar, respectively.

`

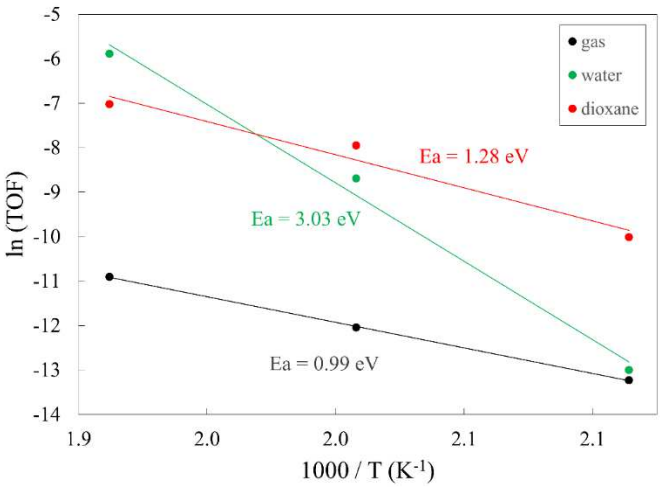

Figure 2.6: Arrhenius plot for the HDO of propionic acid in the temperature range 473−523 K with a propionic acid gas phase partial pressure of 1 bar, a CO gas phase partial pressure of 0.001 bar and a hydrogen partial pressure of 0.1 bar.

2.8 Bibliography

1. J. N. Chheda, G. W. Huber and J. A. Dumesic, *Angew Chem Int Ed Engl*, 2007, **46**, 7164-7183.
2. D. C. Elliott, *Energ Fuel*, 2007, **21**, 1792-1815.
3. G. Knothe, *Fuel Processing Technology*, 2005, **86**, 1059-1070.
4. M. J. Ramos, C. M. Fernandez, A. Casas, L. Rodriguez and A. Perez, *Bioresour Technol*, 2009, **100**, 261-268.
5. G. W. Huber, P. O'Connor and A. Corma, *Applied Catalysis A: General*, 2007, **329**, 120-129.
6. J. Regalbuto, *Computers & Chemical Engineering*, 2010, **34**, 1393-1396.
7. J. Wildschut, F. H. Mahfud, R. H. Venderbosch and H. J. Heeres, *Industrial & Engineering Chemistry Research*, 2009, **48**, 10324-10334.
8. D. Kubička, P. Šimáček and N. Žilková, *Topics in Catalysis*, 2008, **52**, 161-168.
9. J. Lu, S. Behtash and A. Heyden, *The Journal of Physical Chemistry C*, 2012, **116**, 14328-14341.
10. S. Behtash, J. Lu, M. Faheem and A. Heyden, *Green Chem.*, 2014, **16**, 605-616.
11. S. Behtash, J. Lu, C. T. Williams, J. R. Monnier and A. Heyden, *The Journal of Physical Chemistry C*, 2015, **119**, 1928-1942.
12. J. M. Lu, S. Behtash, M. Faheem and A. Heyden, *Journal of Catalysis*, 2013, **305**, 56-66.
13. J. M. Lu, M. Faheem, S. Behtash and A. Heyden, *Journal of Catalysis*, 2015, **324**, 14-24.
14. S. Behtash, J. Lu, O. Mamun, C. T. Williams, J. R. Monnier and A. Heyden, *The Journal of Physical Chemistry C*, 2016, **120**, 2724-2736.
15. Y. Q. Chen, D. J. Miller and J. E. Jackson, *Industrial & Engineering Chemistry Research*, 2007, **46**, 3334-3340.
16. H. Wan, R. V. Chaudhari and B. Subramaniam, *Topics in Catalysis*, 2012, **55**, 129-139.

17. J. Lu, S. Behtash, O. Mamun and A. Heyden, *ACS Catalysis*, 2015, **5**, 2423-2435.
18. M. Faheem, M. Saleheen, J. Lu and A. Heyden, *Catalysis Science & Technology*, 2016, **6**, 8242-8256.
19. W. R. M. A. Vannice, *Journal of Catalysis*, 2000, **192**, 322-334.
20. H. Olcay, L. Xu, Y. Xu and G. W. Huber, *ChemCatChem*, 2010, **2**, 1420-1424.
21. Y. K. Lugo-José, J. R. Monnier and C. T. Williams, *Applied Catalysis A: General*, 2014, **469**, 410-418.
22. S. Behtash, J. Lu, E. Walker, O. Mamun and A. Heyden, *Journal of Catalysis*, 2016, **333**, 171-183.
23. M. Faheem, S. Suthirakun and A. Heyden, *The Journal of Physical Chemistry C*, 2012, **116**, 22458-22462.
24. M. Arend, T. Nonnen, W. F. Hoelderich, J. Fischer and J. Groos, *Applied Catalysis A: General*, 2011, **399**, 198-204.
25. O. Mamun, M. Saleheen, J. Q. Bond and A. Heyden, *Journal of Catalysis*, 2019, **379**, 164-179.
26. G. Kresse and J. Hafner, *Phys Rev B Condens Matter*, 1993, **47**, 558-561.
27. G. Kresse and J. Furthmuller, *Comp Mater Sci*, 1996, **6**, 15-50.
28. G. Kresse and D. Joubert, *Physical Review B*, 1999, **59**, 1758-1775.
29. J. P. Perdew and Y. Wang, *Phys Rev B Condens Matter*, 1992, **45**, 13244-13249.
30. J. P. Perdew and W. Yue, *Phys Rev B Condens Matter*, 1986, **33**, 8800-8802.
31. W. P. Davey, *Physical Review*, 1925, **25**, 753-761.
32. H. J. Monkhorst and J. D. Pack, *Physical Review B*, 1976, **13**, 5188-5192.
33. G. Henkelman, B. P. Uberuaga and H. Jonsson, *Journal of Chemical Physics*, 2000, **113**, 9901-9904.
34. G. Henkelman and H. Jonsson, *Journal of Chemical Physics*, 1999, **111**, 7010-7022.
35. R. A. Olsen, G. J. Kroes, G. Henkelman, A. Arnaldsson and H. Jonsson, *J Chem Phys*, 2004, **121**, 9776-9792.
36. A. Heyden, A. T. Bell and F. J. Keil, *J Chem Phys*, 2005, **123**, 224101.
37. T. S. Tomoshige Nitta, Masayuki Kuro-oka, Takashi Katayama, *JOURNAL OF CHEMICAL ENGINEERING OF JAPAN*, 1984, **17**, 39-45.
38. I. Chorkendorff and J. W. Niemantsverdriet, *Concepts of modern catalysis and kinetics*, Wiley-VCH, Weinheim, 2005.
39. S. C. Ammal and A. Heyden, *ACS Catalysis*, 2019, **9**, 7721-7740.
40. E. A. Walker, D. Mitchell, G. A. Terejanu and A. Heyden, *ACS Catalysis*, 2018, **8**, 3990-3998.
41. J. C. Lee, Y. Xu and G. W. Huber, *Applied Catalysis B-Environmental*, 2013, **140**, 98-107.
42. C. T. Campbell, *ACS Catalysis*, 2017, **7**, 2770-2779.
43. C. T. Campbell, *Journal of Catalysis*, 2001, **204**, 520-524.
44. V. Pallassana and M. Neurock, *Journal of Catalysis*, 2002, **209**, 289-305.

`

CHAPTER 3

INVESTIGATE THE REACTION MECHANISMS OF THE HYDRODEOXYGENATION OF PROPIONIC ACID ON RH (111) SURFACE: A FIRST PRINCIPLES STUDY[2]

[2] W. Yang, R.V. Solomon, O. Mamun, J.Q. Bond and A. Heyden. To be submitted to Journal of Catalysis.

`

3.1 ABSTRACT

Microkinetic models based on first principles calculations have been used to study the vapor and liquid phase hydrodeoxygenation of propionic acid on Rh (1 1 1) surface. Calculations suggest that both decarboxylation and decarbonylation do not occur at an appreciable rate in all reaction environments. Propanol and propionaldehyde are the main products and produced at similar rates in both vapor and liquid phases. While a condensed phase can shift the reaction rate, the dominant pathways and selectivity towards the various products are hardly affected. At 473 K, the propionic acid conversion rate is increased by about 1 time in liquid water relative to the gas phase. In liquid 1,4-dioxane, the conversion rate is slightly increased comparing to the gas phase. With larger Rh cavity radius being used in the liquid phase calculations, the promotion effect of solvent to the rate of the reaction becomes more significant.

KEYWORDS: Propionic acid, Hydrodeoxygenation mechanism, Propanol, Propionaldehyde, Microkinetic modeling, Solvent effect, Lateral interaction

3.2. Introduction

Our industry relies heavily on fossil oil as the primary feedstock to produce transportation fuels, commercial chemicals, electricity and many other residential products. However, we are now not only facing the problems of reserves completion, but also many environmental and climate problems brought by the usage of the fossil fuels, such as the global warming and air pollution. Therefore, finding renewable and 'green' energy resources is gaining increasing attention worldwide. In this concept, biomass is particularly interesting as it is carbon neutral and has much less negative effect on the

`

environment[1-6]. Unfortunately, however, biomass derivatives always suffer from disadvantages such as high viscosity, low energy density, high cloud point temperature and poor oxidative stability due to its high O/C ratio which greatly limits its compatibility to current infrastructure[7-10]. Therefore, there is an urgent need in the deoxygenation of the oxygen-rich biomass derivatives into hydrocarbons with similar properties to conventional petrol-based chemicals and fuels. Vegetable oils, waste fats, algal lipids and many other lipid-rich biomass feedstocks serves as one of the potential class of raw materials to produce biomass-based chemicals and biofuels. During the past decades, many research efforts have been focused on converting these fatty esters and acids into liquid hydrocarbons through hydrodeoxygenation (HDO) process [4, 11, 12]. However, short catalyst lifetime, difficulty in product's separation and many other problems have been reported over the traditional petrol-based catalyst system [4, 11, 13, 14]. As a result, there is an apparent need in the design of new catalyst for the HDO of acids and esters. To rationally design a catalyst for the HDO of organic acids and esters, it is necessary to obtain a comprehensive understanding of the HDO reaction mechanism on the catalyst surface. Key parameters that determine the activity and product selectivity of the catalyst need to be identified which can be used to help the catalyst design.

Recently, we have studied the HDO of propionic acid, our model molecule for organic acid, on various transition metal surfaces based on density functional theory calculations. Two major mechanisms for the HDO of propionic acid, decarbonylation (DCN) and decarboxylation (DCX), have been identified over Pd (111)[15, 16], Pd (211)[17], Ru (0001)[18] surfaces. Through a combination of first-principle calculations and microkinetic modeling, the dominant pathways and rate-controlling steps were identified.

`

According to the results, DCN pathway is always found to prefer over DCX pathway and C-OH bond cleavage is controlling the rate of the HDO process. Our results are in agreement with the experimental results from Murzin *et al* that DCN pathway is favored over DCX pathway in the HDO of long chain fatty acids over Pd/C catalysts[19-22]. Besides, Boda *et al* also reported that DCN pathway is the most dominant path in the HDO of caprylic acid on Pd/C catalyst[23]. However, besides DCN and DCX pathways, alcohols and aldehydes can also be formed in the HDO of acids. For instance, at a temperature of around 400 K and a high H_2 partial pressure (>20 bar), Chen et al[24] found a high selectivity towards propanol production during the HDO of propionic acid on Ru/C catalyst. According to our most recent study, we also found that propanol and propionaldehyde can be produced in the HDO of propionic acid on Pt (111) surface under both vapor and aqueous phases[25]. However, to the best of our knowledge, very few works were reported on the study of the mechanisms of the propanol and propionaldehyde production during the HDO of propionic acid. Therefore, in order to rationally and efficiently design novel catalysts for the HDO of organic acids (such as propionic acid), knowledges on as many reaction pathways of HDO process as possible and reaction mechanisms on various metal surfaces need to be established. Rhodium has long been used in C-H activation[26, 27], hydrogenation reactions[28-30], olefin functionalization[31] and cycloaddition reactions[32]. Interestingly, multiple reaction products have been observed for these Rh catalyzed reactions. For instance, in the study of the aqueous-phase hydrogenation of acetic acid over Rh catalyst, Olcay et al[30] observed both ethanol and alkane production. In contrast, in their recent study of the vapor phase HDO of propionic acid over Rh/SiO_2 catalysts, Lugo-José et al [33] found a 89% selectivity towards DCN and

`

DCX products and 10% selectivity to propane production while no alcohol was observed in the products. Apparently, the reaction conditions and environment appear to contribute to the discrepancy in the product selectivity, and thus Rh catalyst can be an ideal model catalyst system to investigate the activity and selectivity determining steps for the DCN, DCX, alcohol and aldehyde production for the HDO of propionic acid under different reaction conditions.

In this work, therefore, based on microkinetic modelling and first principle calculations, we conducted a comprehensive study of the HDO of propionic acid on Rh (111) surface. Dominant pathways, reaction orders as well as rate-controlling and selectivity-controlling species were identified. Besides, regarding to the solvent effects, several studies have reported a significant effect of a solvent on the reaction mechanisms, activity and product selectivity of HDO reactions[25, 34-37]. For instance, Hoelderich *et al* studied the deoxygenation of oleic acid in water and found a maximum of 20% change in selectivity towards C17 hydrocarbon production[38]. Similarly, Behtash et al [34, 35] found that the rate of DCX was increased in liquid water and becomes competitive to the DCN pathway in the HDO of propionic acid on both Pd (111) and Pd (211) surfaces. Finally, Yang et al studied the HDO of propionic over Pt (111) surface[25], and found that the reaction rate was increased by almost two orders of magnitude in liquid water and dioxane at a temperature of 498 K. Besides, the selectivity towards propanol productions was increased by almost 4 times while that of the DCN pathway was decreased dramatically (became negligible) in both liquid water and dioxane. Therefore, in this work, we also studied the HDO of propionic acid over Rh (111) surface under liquid phase environment. Water and 1,4-dioxane were selected as the solvent since they are

`

usually used in both academic and industrial communities. The solvent effect on the dominant pathways, reaction orders, turnover frequencies (TOF) and apparent activation energies have thus been fully studied.

3.3. Methods

3.3.1. Computational Methods.

All gas phase calculations were performed using Vienna Ab Initio Simulation Package (VASP)[39, 40] based on the density functional theory (DFT) with the projector augmented wave (PAW) method[41]. The electron exchange-correlation effects were described by the generalized gradient approximation (GGA) with the Perdew and Wang functional (PW91)[42, 43]. An energy cutoff of 400 eV was set to the plane wave basis set and the energy convergence criterion was set to 10^{-7} eV. All the structures were optimized with the Hellmann-Feynman force on each atom being smaller than 0.01 eV $Å^{-1}$. The optimized lattice constant of Rh bulk (3.786 Å) is in good agreement with the reported experimental value of 3.804 Å[44]. A $3 \times 2\sqrt{3}$ Rh (111) surface slab with four Rh atom layers has been built to simulate the Rh catalyst surface. The surface slab is separated perpendicularly by a 15 Å vacuum space in order to avoid the interactions between the periodic slabs. For all the surface calculations, the bottom two atom layers were fixed to their bulk positions while the top two layers were fully relaxed in all directions. In the vibrational frequency calculations, all metal atoms were fixed at their optimized positions. It should be noted that frequencies below 100 cm^{-1} were shifted to 100 cm^{-1} in the calculation of vibrational partition function in order to minimize the errors associated with the harmonic approximation for small frequencies[45]. Integration over the Brillouin zone was sampled by a 4×4×1 k-points mesh grid based on the

`

Monkhorst-Pack scheme for the surface calculations[46]. Climbing image nudged elastic band (CI-NEB) method[47] and dimer method[48-50] were employed to locate the transition states of each elementary reaction step.

The implicit solvation model for solid surfaces (iSMS) method developed by our group was used to study the solvent effect on reaction mechanisms[36]. In the model, we defined the free energy function for an absorbed surface intermediate on a periodic metal slab in liquid as $G^{liquid}_{surface+intermediate}$, using a simple subtraction scheme as follows:

$$G^{liquid}_{surface+intermediate} = G^{vacuum}_{surface+intermediate} + (G^{liquid}_{cluster+intermediate} - E^{vacuum}_{cluster+intermediate}) \quad (3.1)$$

where $G^{vacuum}_{surface+intermediate}$ is the DFT calculated free energy of the surface slab model in the absence of a solvent, $G^{liquid}_{cluster+intermediate}$ is the free energy of a metal cluster in the liquid built by removing selected metal atoms from the periodic slab model and removing the periodic boundary conditions, while $E^{vacuum}_{cluster+intermediate}$ is the DFT energy of the same cluster model without the solvent. $G^{liquid}_{cluster+intermediate}$ was calculated via COSMOtherm program using the COSMO-RS implicit solvation model. Thermodynamic properties of the solvents are obtained from the COSMOtherm database at the TZVP level. For all the other structures, COSMO-RS calculations were conducted at the same level of theory. Calculations with a ± 10% of the default COSMO Rh cavity were also performed to investigate the effect of Rh cavity.

`

3.3.2. Microkinetic Modeling

Absorption free energies of all intermediates, G_{ads}, were calculated based on the following equations,

$$G_{ads} = G_{slab+intermediate} - G_{slab} - N_C \times E_C - N_H \times E_H - N_O \times E_O \quad (3.2)$$

$$E_H = 0.5 \times E_{H2} \quad (3.3)$$

$$E_C = E_{CH4} - 2 \times E_{H2} \quad (3.4)$$

$$E_O = E_{H2O} - E_{H2} \quad (3.5)$$

where $G_{slab+intermediate}$ is the free energy of intermediate on the surface slab, G_{slab} is the free energy of the clean surface slab, while E_{CH4}, E_{H2O}, E_{H2} are the total energies of CH_4, H_2O and H_2 molecule, respectively. N_C, N_H and N_O are the number of C, H and O atoms in the adsorbed surface intermediates. The reaction energy and activation energy barrier of various elementary steps were calculated using the following equations,

$$\Delta G_i^{rxn} = \Sigma_j \nu_{ij} \times G_{ads,j}^{i} \quad (3.6)$$

$$\Delta G_i^{\ddagger} = G_{ads,i}^{\ddagger} - \Sigma G_{ads,i}^{R} \quad (3.7)$$

where ΔG_i^{rxn} and $\Delta G_i^{\ddagger}$ are the reaction energy and activation barrier of reaction step i, respectively, and ν_{ij} and $G_{ads,j}^{i}$ are the stoichiometry coefficient and adsorption energy of intermediates j in reaction step i, respectively. Finally, $G_{ads,i}^{\ddagger}$ and $G_{ads,i}^{R}$ are the adsorption energies of transition state and the sum of the adsorption energy of reactant (R) of reaction step i, respectively.

Based on the transition state theory, the forward reaction rate constant (k_{for}) can be calculated as,

`

$$k_{\text{for}} = \frac{k_B T}{h} e^{-\frac{\Delta G‡}{k_B T}} \quad (3.8)$$

where k_B is the Boltzmann constant, h is Planck constant, T is the reaction temperature in K, and $\Delta G‡$ is the zero-point corrected activation barrier for the forward reaction obtained from DFT calculations. For adsorption reaction, the forward reaction rate constant was calculated based on the collision theory with an approximately sticking probability of 1 independent of the solvent,

$$k_{for} = \frac{1}{N_0 \sqrt{2\pi m_A k_B T}} \quad (3.9)$$

where N_0 is the number of sites per surface area (2.08×10^{19} m^{-2}) on the Rh (111) surface and m_A is the molecular weight of adsorbate A. With forward reaction rate constant, the reverse reaction rate constant (k_{rev}) can be determined from the thermodynamic equilibrium constant K,

$$K = \frac{k_{for}}{k_{rev}} \quad (3.10)$$

To include solvent effect in the microkinetic modeling, the reaction energy and activation barrier were recalculated for the liquid phase microkinetic model by the following equations,

$$\Delta G^{‡}_{solvent,i} = G^{‡}_{gas,i} + G_{TS}(\text{solv}) - G_{IS}(\text{solv}) \quad (3.11)$$

$$\Delta G^{rxn}_{solvent,i} = G^{rxn}_{gas,i} + G_{FS}(\text{solv}) - G_{IS}(\text{solv}) \quad (3.12)$$

with G_{IS}(solv), G_{FS}(solv), and G_{TS}(solv) being the solvation free energies of reactants, transition state and products, respectively, that were obtained from the COSMO-RS calculations.

`

3.4. Results and discussion

The detailed reaction network of HDO of propionic acid on Rh (111) surface that consists of DCN, DCX and propanol and propionaldehyde production path is shown in Fig. 3.1. Basically, there are two types of DCN reaction pathways: (1) pathways that start with propionic acid dehydroxylation, $CH_3CH_2COOH^* + 3^* \rightarrow CH_3CH_2CO^{***} + OH^*$ and followed by either direct decarbonylation or one step of dehydrogenation prior to the decarbonylation, and (2) pathways that involve α–carbon dehydrogenation prior to the dehydroxylation step that precedes the decarbonylation. For DCX reaction, there are generally three types of relevant reaction pathways: (1) dehydrogenation of the carboxyl group followed by directly α-carbon dehydrogenation or α-carbon dehydrogenation prior to decarboxylation, (2) one or two α-carbon dehydrogenation steps occur before dehydrogenation of the carboxyl group dehydrogenation and the following decarboxylation, (3) both α- and β-carbon dehydrogenation occur before dehydrogenation of the carboxyl group and the following decarboxylation. While for propanol production, we mainly considered three possible pathways: (1) direct dehydroxylation of the adsorbed $CH_3CH_2COOH^*$, followed by hydrogenation of the carbonyl group of $CH_3CH_2CO^{***}$ to form propanol, which will be referred to as direct-propanol-path, (2) a dehydrogenation step (either α- or β-carbon) taking place prior to dehydroxylation, followed by a couple of hydrogenation steps forming propanol, which will be denoted as the indirect-propanol-path, and (3) hydrogenation of the produced propionaldehyde to propanol. Similarly, we also considered three possible pathways for propionaldehyde production: (1) direct dehydroxylation of the adsorbed propionic acid forming a single hydrogen deficient aldehyde ($CH_3CH_2CO^{***}$), followed by one hydrogenation step to

`

form propionaldehyde on the surface, which will be referred as direct-aldehyde-path, (2) dehydrogenation of one hydrogen deficient propanol to form propionaldehyde, i.e., $CH_3CH_2COOH^*$ −> $CH_3CH_2CO^{***}$ −> $CH_3CH_2COH^*$ −> $CH_3CH_2CHOH^*$ −>$CH_3CH_2CHO^*$, which will be called indirect-aldehyde-path, and (3) dehydrogenation of propionic acid prior to dehydroxylation, followed by hydrogenation to propionaldehyde.

Table 3.1 shows the zero-point energy corrected reaction energies and activation energy barriers of all the reaction steps calculated at a temperature of 473 K. The solvent effects of water and 1,4-dioxane are treated as corrections to the reaction energies and activation energy barriers which are also shown in Table 3.1. In the following sections, we will firstly discuss our lateral interaction model and the results from our microkinetic model (with lateral interaction included) under gas phase including the turnover frequency (TOF), the dominant pathways and selectivity. Then, the solvent effect on both the thermodynamics and kinetics will be discussed systematically. Results from sensitivity analysis, such as degrees of rate control, degrees of thermodynamic rate control and degrees of selectivity control, will also be discussed thereafter. Finally, reaction orders and apparent activation energies under both gas phase and liquid phase will be reported.

3.4.1 Lateral interaction effects

Strong adsorbate-adsorbate attraction, especially the attraction between the most abundant surface adsorbates, can lead to island formation which leads to an overestimation of the rate predicted by the mean-field approximation. Therefore, the mean-field approximation based microkinetic model is typically derived under the

`

assumption of no lateral adsorbate-adsorbate interactions. However, slight adsorbate-adsorbate repulsion can still be accommodated by mean-field models that include the repulsive interaction within the free energy expression[51]. Without any lateral interactions being included, our mean-field microkinetic model results showed that more than 99% of the Rh surface was covered by CO and H, and the fraction of available free sites is exceedingly small. Since both adsorbed CO and H display significant lateral (repulsive) interactions, we should consider these interactions in our microkinetic models. Here, we used a linear lateral interaction model to describe the effects of any high-coverage surface species (CO and H in this work) on the free energy of any surface species in the microkinetic model, while the transition states are assumed to be affected as half the reactant and half the product. The lateral interaction included free energy are calculated based on the following equations:

$$G^i_{ads}(\theta_j) = G^i_{ads}(0) + a_{i,j} * \theta_j \quad (13)$$

$$G^i_{ads}(\theta_1, \dots, \theta_n) = G^i_{ads}(0) + \sum^n_{j \neq i} a_{i,j} * \theta_j \quad (14)$$

$$G^k_a(\theta_1, \dots, \theta_n) = G^k_a(0) + 0.5(G^k_{rxn}(0) - G^k_{rxn}(\theta_1, \dots, \theta_n)) \quad (15)$$

where $G^i_{ads}(0)$ and $G^i_{ads}\ (\theta_j)$ are the adsorption energies of specie i at low surface coverage and high surface coverage (θ_j) of species j (CO or H in this work), respectively. While $a_{i,j}$ is the lateral interaction coefficient of specie j to specie i, and $G^k_a(\theta_1, \dots, \theta_n)$ and $G^k_{rxn}(\theta_1, \dots, \theta_n)$ are the activation barrier and reaction energy of step k with the surface covered by specie i of a coverage θ_i, respectively.

The adsorption energies of all species with 0 and 3 CO and H on the surface (correspond to 0 and 0.25 ML surface coverage, respectively) were used to calculate the

`

lateral interaction coefficient based on the equation 13. All the calculated lateral interaction coefficients are shown in Table B.1 in the appendix B and implemented into the microkinetic model assuming the coefficients being constant at the investigated coverage region in this work. Fig. B.1 in the appendix B shows the coverage dependent adsorption energy of CO on the Rh (111) surface. Two straight linear regions were found for the coverage dependent adsorption energy of CO in the figure demonstrating that a linear model can perfectly describe the coverage dependent adsorption energy at a specific range. Obviously, we can see that the adsorption energy changes much more rapidly in region 2 than that in region 1, which indicating that the lateral interaction coefficient in region 1 is smaller than that of region 2. The corresponding coverage range of CO we used to calculate the lateral interaction coefficient (0.25 ML) lies perfectly in the linear region 1 of Fig. B.1, which make our usage of the lateral interaction coefficient as constant solid. Interestingly, we found that the number of sites of CO occupy via adsorption on the surface have a significant effect on the resulting CO coverage from microkinetic modeling (MKM). When 1 site were assumed for the CO adsorption, the MKM predicted CO surface coverage is larger than 0.60 ML as shown in Table B.2 of the appendix B, and it lies exactly in the linear region 2 of Fig. B.1 in the appendix B. In other words, the usage of lateral interaction coefficient calculated from linear region 1 will underestimate the real values. On the contrary, however, when 3 sites were considered for the CO adsorption, the resulting CO coverage from MKM as shown in Table 3.2 is smaller than 0.30 ML which fits perfectly to linear region 1 of Fig. B.1 in the appendix B. The proposed scheme to calculate the lateral interaction coefficient and the assumption that the lateral interaction coefficient is constant are therefore very solid

`

when 3 sites were considered for CO adsorption. Therefore, unless specified in this work, all the results that will be discussed in the following sections are from microkinetic modeling with CO occupy 3 sites via adsorption on the surface.

3.4.2 Microkinetic modeling results

3.4.2.1 HDO of propionic acid in vapor phase

The microkinetic model was running at a temperature of 473 K and a gas phase partial pressure of Pac, H_2 and CO of 1 bar, 0.1 bar and 0.001 bar, respectively. The TOFs and the surface coverages of the most abundant surface species (MASS) are shown in Table 3.2. Under vapor phase, the rate of the HDO reaction is 3.43×10^{-5} s^{-1} and the surface is mainly covered by CO*** and H* with a surface coverage of 0.48 and 0.50, respectively. As a result, very few free sites (1.5%) are available for reactions to take place on the surface, which explains the low TOF of the reaction in vapor phase. The rates of various elementary surface reactions in the vapor phase are shown in Fig. 3.1, and the dominant pathway of DCX, DCN path and the propanol and propionaldehyde production is shown in dashed arrows. Apparently, the propanol and propionaldehyde production are favored in the HDO of propionic acid under vapor phase and dominantly occur on the surface with a selectivity of 55% and 45%, respectively. While both DCN and DCX are not preferred and the rate of which are negligible comparing to that of propanol and propionaldehyde production (almost 4 orders of magnitude smaller). The dominant pathway of propanol production is the direct-propanol-path, $CH_3CH_2COOH^*$ -> $CH_3CH_2CO^{***}$ -> $CH_3CH_2COH^*$ -> $CH_3CH_2CHOH^*$ -> $CH_3CH_2CH_2OH^*$, and the dominant pathway for propionaldehyde production is the direct-aldehyde-path that follows $CH_3CH_2COOH^*$ -> $CH_3CH_2CO^{***}$ -> $CH_3CH_2CHO^*$. In other words, direct-

`

propanol-path and direct-aldehyde-path are the dominant pathways of the HDO of propionic acid on Rh (111) surface under vapor phase. Interestingly, we didn't find any significant amount of propionaldehyde production from propanol dehydrogenation as we previously found in the HDO of propionic acid on the Pt (111) surface[25]. We also considered the microkinetic model with CO occupy 1 site via adsorption (CO-1-site model) on the surface under the same conditions that were used here. Except a discrepancy in the TOF and the surface coverage of the most abundant surface species as shown Table B.2 in the appendix B, the dominant pathway of the reaction is still the direct-propanol-path and the direct-aldehyde-path. DCN and DCX are also not favored under CO-1-site model, and the rate of which is still negligible as shown in Fig. B.2 in the appendix B.

3.4.2.2 HDO of propionic acid in liquid phase

The effects of solvent water and 1,4-dioxane are shown as corrections to the reaction free energies and activation free energy barriers in Table 3.1. For all the adsorption steps except the adsorption of CO and CO_2, solvent generally has negligible effect, and effect of water are stronger than 1,4-dioxane. As shown in Table 3.1, the adsorption of CO is stabilized by 0.14 eV and 0.09 eV, respectively, in water and 1,4-dioxane. Correspondingly, CO_2 adsorption is stabilized by 0.23 eV and 0.12 eV, respectively, in water and 1,4-dioxane. In addition, adsorption of propionic acid also becomes stronger in the liquid phase than in the gas phase, being stabilized by 0.05 eV and 0.07 eV, respectively in water and 1,4-dioxane. For surface reactions, similarly, the solvents also have negligible effect on most of the reaction steps except for a few steps that are involved in DCX path, which caused an increase of DCX rate and will be

`

discussed further in the following sections. Specifically, the solvents have a large effect on reaction step of 29, 30, 31, 35, 38 and 39, and water still has a stronger effect than 1,4-dioxane. For instance, the reaction energy and activation energy barrier of step 29 ($CH_3CH_2COO^{**}$ -> $CH_3CH_2^*$ + CO_2^*) are decreased by 0.15 eV and 0.11 eV, respectively, in water, while they are decreased by 0.06 eV and 0.02 eV, respectively, in 1,4-dioxane. Step 30 ($CH_3CH_2COO^{**}$ -> CH_3CHCOO^{***} + H^*), which is in competition with step 29 in DCX path, is one other step that is greatly affected by the solvents. The reaction energy and activation barrier of step 30 are decreased by 0.14 eV and 0.12 eV, respectively, in water, while in 1,4-dioxane, they are decreased by 0.03 eV and 0.02 eV, respectively. The stabilization can be understood from the change in exposure of the carboxylate group to the liquid phase during reaction (in the reactant state the carboxylate group points to the surface while in the product state it points at least partially to the liquid phase). In general, water makes DCX reaction steps more exothermic in reaction and easier in overcoming the reaction energy barriers which increase the reaction rate as a result as shown in Table 3.2. While the effects of 1,4-dioxane is usually smaller than 0.1 eV which explain the similar TOF of the reaction in vapor phase and liquid 1,4-dioxane. The energies calculated at ± 10% of the default COSMO Rh cavity are shown in Table B.3 and B.4, respectively, with a similar trend of the solvent effects found in Table 3.1. Interestingly, a larger Rh cavity radius leads to a larger solvent effect for adsorption steps and processes involving a change in exposure of the carboxylate group to the liquid phase. The effects of the solvents on microkinetic modelling kinetic results will be discussed in the following sections.

`

The liquid phase microkinetic model with the solvent effect being included was conducted at the same gas phase partial pressures and temperature as that of the gas phase model. The TOFs and the surface coverages of the most abundant surface species are shown in Table 3.2. Obviously, the TOFs is increased in the liquid phase, and the larger the Rh cavity radius used in the liquid phase calculations, the larger the increase of the TOFs. For instance, in liquid water, the TOF was increased from 3.43×10^{-5} s^{-1} to 8.73×10^{-5} s^{-1} when using the default COSMO Rh cavity, while the TOF was increased to 1.17×10^{-4} s^{-1} if the Rh cavity was increased by 10% in the liquid phase calculations. The same trend was also found in the liquid 1,4-dioxane while the increasement of which to the TOF is smaller than liquid water since the solvent effect of 1,4-dioxane is usually smaller than 0.1 eV as shown in Table 3.1. For instance, when decreasing the Rh cavity by 10% in the liquid phase calculations, the TOF of the reaction is 8.00×10^{-5} s^{-1} in the liquid water, and it is only 3.85×10^{-5} s^{-1} in the liquid 1,4-dioxane with a slightly increase comparing to that in the vapor phase (3.43×10^{-5} s^{-1}). However, with increasing Rh cavity, the promotion effect of 1,4-dioxane to the TOF becomes more significant as shown in Table 3.2. The most abundant surface species (MASS) are still CO*** and H* and occupies most of the surface sites (> 95%). The surface coverage of CO*** is increased in both water and 1,4-dioxane since CO adsorption is greatly stabilized in the liquid phase as discussed in the first part of this section, while the surface coverage of H* was decreased due to a destabilization of the solvent to its adsorption. The coverage of CH_3CH_2COOH* is increased by more than one order of magnitude because of the stabilization of the solvent to the propionic acid adsorption, and the increased coverage of CH_3CH_2COOH* may contribute to the increased TOF of the reaction in the liquid phase.

`

We also observed an increase of the $CH_3CH_2COO^{**}$ coverage which was caused by the stabilization of the solvent to the DCX reactions. However, the coverage of $CH_3CH_2COOH^{*}$ and $CH_3CH_2COO^{**}$ are much smaller than the coverage of CO^{***} and H^{*}.

As shown in Fig. 3.2 and Fig. 3.3, the solvent doesn't change the dominant pathways of the reaction, and the direct-propanol-path and the direct-aldehyde-path are still the dominant pathways of the reaction in both liquid water and 1,4-dioxane. The selectivity toward propanol and propionaldehyde production are around 60% and 40%, respectively, in liquid water, and the corresponding selectivity are around 51% and 49%, respectively, in liquid 1,4-dioxane. The rate of DCN and DCX path are greatly increased in the liquid phase which agrees well with previous studies on the HDO of propionic acid and acetic acid on transition metals surfaces[25, 30, 34, 35]. For instance, comparing to that in the vapor phase, the rate of DCX in liquid water is increased from 7.23×10^{-12} s^{-1} to 1.11×10^{-10} s^{-1}, while the rate of DCN is increased by more than two orders of magnitude (from 2.79×10^{-11} s^{-1} to 5.00×10^{-9} s^{-1}). In liquid 1,4-dioxane, the increasement in the rate of DCN and DCX is much smaller than that in the liquid water, i.e., the DCX rate is only increased by about 1 time comparing to that in the vapor phase. Despite the promotion of the solvent to the DCN and DCX reactions, the rates of which are still much smaller than propanol and propionaldehyde production in both liquid water and 1,4-dioxane (at least 5 orders of magnitude smaller). For the CO-1-site model, as shown in Fig. B.3 and B.4 in the appendix B, the dominant pathways of the reaction are also the direct-propanol-path and the direct-aldehyde-path, and the DCN and DCX are still not favored.

`

In a summary, the dominant pathways of the reaction remain unchanged in in both vapor and liquid phase environments. However, the rate of the reaction is increased in liquid phase and water has a stronger effect that 1,4-dioxane. The rate of DCN and DCX is greatly increased in liquid phase, but it is still much smaller than the propanol and propionaldehyde production rate. In both vapor and liquid phases, the main products, propanol and propionaldehyde, have a similar selectivity, demonstrating that solvent (at least water and 1,4-dioxane) cannot be used to tune the selectivity of the HDO of propionic acid on Rh (111) surface. Finally, DCX and DCN path are not favored in all reaction environments indicating that Rh (111) may not be the active site for DCX and DCN reactions.

3.4.3 Degrees of rate and selectivity control

Campbell's degree of kinetic rate control DRC_i, where i is either one transition state or one surface intermediate, and degree of selectivity control DSC_i were used to determine the rate-controlling and selectivity-controlling species[52-54]. The degree of rate control and selectivity control are calculated based on the following equations,

$$DRC_i = \left(\frac{\partial \ln r}{\partial \frac{-G_i^0}{RT}}\right)_{G_{j\neq i}^0} \tag{16}$$

$$DSC_i = \left(\frac{\partial(\ln rp/rR)}{\partial \frac{-G_i^0}{RT}}\right)_{G_{j\neq i}^0} = \left(\frac{\partial(\ln rp)}{\partial \frac{-G_i^0}{RT}}\right)_{G_{j\neq i}^0} - \left(\frac{\partial(\ln rR)}{\partial \frac{-G_i^0}{RT}}\right)_{G_{j\neq i}^0} = DRC_{i,P} - DRC_{i,R} \tag{17}$$

where the partial derivative is taken holding the free energies of all other species ${G_j}^0$ constant. The value of DRC_i describes the relative increase in net rate due to the

`

(differential) stabilization of the standard-state free energy for species i. $DRC_{i,P}$ and $DRC_{i,R}$ are the degrees of rate control of species i for the rates of yielding product P and consuming reactant R, respectively. The value of DSC_i describes the relative increase in net selectivity to product P from reactant R due to the (differential) stabilization of species i.

The degrees of rate control of the key species are shown in Table 3.3. For the transition states, step1 ($CH_3CH_2COOH^*$ -> $CH_3CH_2CO^{***}$) solely determines the rate of the reaction in both the gas and liquid phases, demonstrating the importance of the dehydroxylation. In other words, stabilizing the transition state of C-OH bond cleavage (step1) will greatly increase the rate of the HDO of propionic acid on Rh (111) surface. The C-OH bond scission has also been identified as the rate controlling step in the HDO of propionic acid over Pd (111) surface[16] and Ru (0001) surface[18], and literature reveals that the HDO of acetic acid also has C-OH bond cleavage as the rate controlling step[30, 55]. From the degrees of thermodynamic rate control which are also shown in Table 3.3, the effect of the adsorption strength of surface intermediates on the reaction rate can be determined. In both gas and liquid phase environments, the two most abundant surface species CO^{***} and H^* have a large negative value of degrees of rate control, demonstrating that stabilize the adsorption CO^{***} and H^* can greatly decrease the rate of the reaction. The strong negative effect can be well understood by their corresponding large surface coverage on the surface since stabilizing their adsorption will make more surface free sites be blocked. As in the in liquid phase, the surface coverage of $CH_3CH_2COOH^*$ and $CH_3CH_2COO^{**}$ was increased to a significantly amount, it is therefore not

`

surprising that their effect on the rate of reaction becomes nonnegligible and stabilizing the adsorption strength will decrease the TOF of the reaction.

The degrees of selectivity control of various key reaction steps for propanol and propionaldehyde production are shown in Table 3.4 and 3.5, and those for the DCN and DCX selectivity are shown in Table B.6 in the appendix B. Results shown in Table 3.4 indicate that the selectivity towards propanol production is mainly determined by step 51 and step 52. Stabilizing reaction step 52 ($CH_3CH_2COH^* + 3^* \rightarrow CH_3CH_2CO^{***} + H^*$) and decelerating the direct propionaldehyde formation step 51 ($CH_3CH_2CHO^* + 3^* \rightarrow CH_3CH_2CO^{***} + H^*$) leads to increased propanol production in all reaction environments. Step 66 ($CH_3CH_2CH_2OH^* + * \rightarrow CH_3CH_2CHOH^* + H^*$) also has significant effect on determining the propanol production, but it is not as important as step 51 and step 52. Generally, CO*** and H* adsorption strength has positive effect on the selectivity of propanol production and stabilizing its adsorption strength can slightly increase the propanol production. For propionaldehyde production, Table 3.5 summarizes the degrees of selectivity control. Again, step 51 and 52 are the key rate controlling steps in all reaction environments determining the relative reaction flux going towards propionaldehyde versus propanol. In contrast to propanol production, however, stabilizing reaction step 52 ($CH_3CH_2COH^* + 3^* \rightarrow CH_3CH_2CO^{***} + H^*$) and decelerating step 51 ($CH_3CH_2CHO^* + 3^* \rightarrow CH_3CH_2CO^{***} + H^*$) leads to decreased propionaldehyde production in all reaction environments. This can be well explained by the fact that step 52 is the key step for propionaldehyde production while step 51 is the key step for propanol production. Similarly, step 66 also plays a significant role in determining the propionaldehyde production and decelerating step 66 (the last step of the

`

dominant propanol formation pathway) favors the propionaldehyde production. For the surface intermediates that have a significant effect on propionaldehyde selectivity, shown in Table 3.5, the stability of adsorbed H* and CO*** are most relevant. Generally, Stabilizing H* and CO*** adsorption decreases the selectivity to propionaldehyde in both the vapor phase and the condensed phase.

3.4.4 Apparent Activation Barrier & Reaction Orders

In order to investigate the temperature dependence of the TOF of the reaction, apparent activation barriers (Ea) have been calculated based on the following equation with a temperature range from 448 K to 573 K in all reaction environments.

$$E_a = k_B T^2 \left(\frac{dln(TOF)}{dT}\right)_{P,T}$$

(18)

To study the pressure dependence of the rate of the reaction, the reaction orders of H_2, CO and propionic acid have also been calculated using,

$$\alpha_i = \left(\frac{dln(TOF)}{dln(P_i)}\right)_{T,P_{j\neq i}}$$

(19)

Fig. 3.4a and 3.4c illustrates the reaction order with respect to H_2 and CO in the vapor phase and liquid phase. In all reaction environments, a negative reaction order was found for both H_2 and CO. H_2 has a reaction order of -1.54, -0.98 and -0.66, respectively, in vapor phase, liquid 1,4-dioxane and liquid water. While a reaction order of -0.23, -0.57 and -0.80 was found for CO in gas phase, liquid 1,4-dioxane and liquid water,

`

respectively. These negative reaction orders correlate (as expected) very well with the corresponding large negative degrees of thermodynamic rate control of H* and CO*** in the different reaction environments as shown in Table 3.3. The reaction orders of propionic acid are all close to 1 under all reaction conditions as shown in Fig. 3.4b, which are 0.97, 0.90 and 0.91, respectively in the vapor phase, liquid 1,4-dioxane and liquid water.

Finally, Fig. 3.4d displays Arrhenius plots for rate of the reaction (consumption of propionic acid) in various reaction environments at a temperature range of 448 K to 573 K. The computed apparent activation barriers are 1.89 eV, 1.89 eV and 1.83 eV in the gas phase, and liquid 1,4-dioxane and water, respectively. The similar activation energies being found in all reaction environments agrees very well with the corresponding observed TOF as shown in Table 3.2. The large apparent activation energy can be explained by the fact the Rh (111) surface favors propanol and propionaldehyde production and the large reaction barriers of step 51 and step 52 (key steps in determining the rate of propanol and propionaldehyde production). As shown in Table B.7 in the appendix B, the reaction barrier of the backward reaction of step 51 and 52, which goes toward propanol and propionaldehyde formation (all the reactions and the corresponding reaction energies in Table B.7 are listed in a dissociation direction), are 0.76 eV and 0.93 eV, respectively. The large apparent activation energy agrees very well with the low TOFs as shown in Table 3.2.

3.5 Conclusions

The HDO of propionic acid over Rh (1 1 1) surface has been systematically studied under both vapor and liquid phase conditions based on the microkinetic modeling

`

and DFT calculations. In all reaction environments, both decarbonylation and decarboxylation are not favored demonstrating that Rh (111) surface may not be the active site for DCN and DCX reaction. Propanol and propionaldehyde production dominantly occur during the HDO of propionic acid on Rh (111) surface, and the dominant pathways for propanol and propionaldehyde production favor a direct formation pathway which starts with direct dehydroxylation and followed by the hydrogenation of the carbonyl group. The dominant pathways of the reaction remain unchanged in the liquid phase while the rate of the reaction was slightly increased by the solvent. Larger Rh cavity radius used in the liquid phase calculations further increase the solvent acceleration on the turnover frequency. Generally, the promotion effect of water is much stronger than 1,4-dioxane on the rate of the reaction. The rate of the reaction is solely controlled by the dehydroxylation of adsorbed propionic acid under both vapor and liquid phase conditions. The selectivity of the main products (propanol and propionaldehyde) is almost the same in all reaction environments. Thus, solvents (at least water and 1,4-dioxane) cannot be designed to manipulate the selectivity of the HDO of organic acids over Rh (111) surface.

3.6 ACKNOWLEDGMENT

We gratefully acknowledge financial support from the U.S. Department of Energy, Office of Basic Energy Science, Catalysis Science program under Award DE-SC0007167 (most of the liquid phase calculations and models and some of the gas phase data) and the National Science Foundation under Grant No. DMREF-1534260 (some of the gas phase data and models). J.Q.B. acknowledges financial support from the National Science Foundation DMREF-1534269. Computational resources have been provided by

`

the National Energy Research Scientific Computing Center (NERSC) which is supported by the Office of Science of the U.S. Department of Energy and in part by XSEDE under grant number TG-CTS090100. Computational resources from CASCADE cluster from Environmental Molecular Sciences Laboratory (EMSL) under Pacific Northwest National Laboratory (PNNL) are also used for the DFT calculations. Finally, computing resources from the USC High Performance Computing Group are gratefully acknowledged. We also gratefully thank the Writing Center of the University of South Carolina for providing suggestions in preparing this paper.

3.7 Tables and figures

Table 3.1: Reaction free energies in eV of various elementary reaction steps in the HDO of Pac on Rh (111) surface at a temperature of 473 K under the vapor phase and liquid phase with water and 1, 4-dioxane as solvent, respectively.

#	Reaction	Gas		Water		1-4-dioxane	
		ΔG_{rxn}	$\Delta G^{‡}$	$\Delta\Delta G_{rxn}$	$\Delta\Delta G^{‡}$	$\Delta\Delta G_{rxn}$	$\Delta\Delta G^{‡}$
0	CH_3CH_2COOH + * -> CH_3CH_2COOH*	0.41	N/A	-0.05	N/A	-0.07	N/A
1	CH_3CH_2COOH* + 3* -> CH_3CH_2CO*** + OH*	0.08	0.65	-0.06	-0.04	0.04	0.02
2	CH_3CH_2COOH* + 2* -> $CH_3CHCOOH$** + H*	0.03	0.63	-0.02	-0.09	0.04	0.01
3	CH_3CH_2CO*** + 2* -> CH_3CH_2** + CO***	-0.51	1.15	-0.06	0.01	-0.05	0.00
4	CH_3CH_2CO*** -> CH_3CHCO** + H*	-0.11	0.82	-0.02	-0.05	-0.01	0.00
5	$CH_3CHCOOH$** + * -> CH_3CHCO** + OH*	-0.06	0.76	-0.05	-0.02	-0.01	-0.01
6	$CH_3CHCOOH$** + 3*->$CH_2CHCOOH$**** + H*	-0.22	0.40	-0.02	-0.03	0.00	-0.01
7	$CH_3CHCOOH$** + 2* -> CH_3CCOOH*** + H*	-0.32	0.26	-0.03	-0.03	-0.03	-0.02
8	CH_3CHCO** + 4* -> CH_3CH*** + CO***	-0.84	0.66	-0.05	0.07	-0.04	0.05
9	CH_3CHCO** + 3* -> CH_3CCO**** + H*	-0.35	0.45	-0.02	-0.02	-0.02	-0.01
10	CH_3CHCO** + 3* -> CH_2CHCO**** + H*	-0.26	0.62	-0.03	-0.02	-0.01	0.03
11	$CH_2CHCOOH$**** + * ->CH_2CHCO**** + OH*	-0.10	0.86	-0.07	-0.01	-0.01	0.02
12	$CH_2CHCOOH$**** + *->$CHCHCOOH$****+ H*	-0.33	0.23	-0.02	-0.01	-0.01	0.01
13	CH_3CCOOH*** + 2* -> CH_3CCO**** + OH*	-0.09	0.86	-0.04	-0.02	0.01	0.02
14	CH_3CCO**** + 2* -> CH_3C*** +CO***'	-1.32	0.22	-0.03	-0.02	-0.03	0.00
15	CH_2CHCO**** + 2* -> CH_2CH*** + CO***	-0.63	0.80	-0.01	0.00	-0.02	0.01
16	CH_2CHCO**** + * -> CHCHCO**** + H*	-0.06	0.43	0.00	-0.01	0.01	0.01
17	CHCHCOOH**** + * -> CHCHCO**** + OH*	0.17	0.92	-0.05	-0.03	0.01	0.00
18	CHCHCO**** + 3* -> CHCH**** + CO***	-1.08	0.54	-0.06	0.04	-0.06	0.00
19	CH_2CH*** + 2* -> CHCH**** + H*	-0.51	0.14	-0.05	-0.05	-0.02	-0.01
20	CH_2CH_2** + 2* -> CH_2CH*** + H*	-0.10	0.42	0.02	-0.01	0.01	0.01
21	CH_2CH*** + * -> CH_2C*** + H*	-0.58	0.04	-0.08	-0.05	-0.05	-0.03
22	CH_3C*** + * -> CH_2C*** + H*	0.20	0.85	-0.07	-0.06	-0.04	-0.03
23	CH_3CH*** + * -> CH_2CH*** + H*	-0.05	0.50	0.01	-0.02	0.00	0.00
24	CH_3CH*** + * -> CH_3C*** + H*	-0.83	0.00	0.00	0.00	-0.01	0.00
25	CH_3CH_2** + 2* -> CH_3CH*** + H*	-0.44	0.71	-0.01	-0.06	0.01	-0.01

`

26	CH_3CH_3* + 2*-> CH_3CH_2** + H*	0.09	0.62	0.01	0.01	0.02	0.02
27	CH_3CH_2** + * -> CH_2CH_2** + H*	-0.39	0.31	-0.02	0.01	0.00	0.03
28	CH_3CH_2COOH* + 2* -> CH_3CH_2COO** + H*	-0.63	0.25	0.01	-0.06	0.02	-0.01
29	CH_3CH_2COO** + * -> CH_3CH_2** + CO_2*	0.76	1.70	-0.15	-0.11	-0.06	-0.02
30	CH_3CH_2COO** + 2* -> CH_3CHCOO*** + H*	0.32	0.93	-0.14	-0.12	-0.03	-0.02
31	$CH_3CHCOOH$** + 2* -> CH_3CHCOO*** + H*	-0.33	0.42	-0.10	-0.08	-0.05	-0.05
32	$CH_3CHCOOH$** + 3* -> CH_3CH*** + COOH**	-0.23	0.93	-0.04	-0.05	-0.01	-0.01
33	CH_3CHCOO*** + * -> CH_3CH*** + CO_2*	0.00	0.95	-0.03	0.02	-0.03	0.02
34	CH_3CHCOO*** + * -> CH_3CCOO*** + H*	0.07	1.02	-0.07	0.02	-0.03	0.01
35	CH_3CCOOH*** + * -> CH_3CCOO*** + H*	0.06	0.83	-0.15	-0.13	-0.04	-0.04
36	CH_3CCOOH*** + 2* -> CH_3C*** + COOH**	-0.74	1.00	-0.01	-0.01	0.01	0.02
37	$CH_2CHCOOH$**** + * ->CH_2CH*** + COOH**	-0.06	1.49	-0.01	-0.01	0.00	0.01
38	CH_3CCOO*** + * -> CH_3C*** + CO_2*	-0.90	0.57	0.05	0.18	-0.01	0.05
39	COOH** -> CO_2* + H*	-0.10	0.71	-0.09	-0.09	-0.06	-0.06
40	COOH** + 2* -> CO*** + OH*	-0.67	0.36	-0.07	0.00	-0.03	0.00
41	H_2O* + * -> OH* + H*	-0.03	0.76	-0.01	-0.05	0.00	-0.02
42	CH_3CH_3 + * -> CH_3CH_3*	0.57	N/A	0.02	N/A	0.00	N/A
43	CH_2CH_2 + 2* -> CH_2CH_2**	-0.10	N/A	-0.01	N/A	0.00	N/A
44	H_2O + * -> H_2O*	0.37	N/A	-0.03	N/A	0.01	N/A
45	CO_2 + * -> CO_2*	0.68	N/A	-0.23	N/A	-0.12	N/A
46	CHCH + 4* -> CHCH****	-1.78	N/A	-0.06	N/A	-0.01	N/A
47	CO + 3* -> CO***	-0.89	N/A	-0.14	N/A	-0.09	N/A
48	H_2 + 2* -> H* + H*	-0.48	N/A	0.02	N/A	0.01	N/A
49	CH_3CHCHO*** -> CH_3CHCO** + H*	-0.41	0.12	-0.01	-0.02	-0.02	-0.02
50	CH_3CHCOH*** -> CH_3CHCO** + H*	-0.49	0.99	-0.04	0.02	-0.02	0.00
51	CH_3CH_2CHO* + 3* -> CH_3CH_2CO*** + H*	-0.75	0.10	-0.04	-0.02	-0.01	-0.03
52	CH_3CH_2COH* + 3* -> CH_3CH_2CO*** + H*	-0.65	0.25	-0.08	-0.07	-0.03	-0.04
53	CH_3CH_2CHO* + 3* -> CH_3CHCHO*** + H*	-0.45	0.21	-0.05	-0.08	0.00	-0.02
54	CH_3CHCH_2O*** + * -> CH_3CHCHO*** + H*	-0.86	0.12	-0.03	-0.04	0.00	-0.01
55	$CH_3CHCHOH$** + 2* -> CH_3CHCHO*** + H*	-0.57	0.34	-0.02	0.01	-0.01	0.00
56	CH_3CH_2COH* + 3* -> CH_3CHCOH*** + H*	-0.27	0.66	-0.06	-0.05	-0.02	-0.01
57	$CH_3CHCHOH$** + 2* -> CH_3CHCOH*** + H*	-0.48	0.29	0.01	0.03	0.00	0.02
58	$CH_3CH_2CH_2O$* + * -> CH_3CH_2CHO* + H*	-0.25	0.47	0.00	-0.04	0.01	0.00
59	CH_3CH_2CHOH* + * -> CH_3CH_2CHO* + H*	-0.37	0.46	0.03	-0.01	0.02	0.00
60	CH_3CH_2CHOH* + * -> CH_3CH_2COH* + H*	-0.47	0.26	0.06	0.03	0.04	0.03
61	$CH_3CH_2CH_2O$* + 3* -> CH_3CHCH_2O*** + H*	0.15	0.83	-0.03	-0.08	0.01	0.00
62	CH_3CHCH_2OH** + 2* -> CH_3CHCH_2O*** + H*	-0.13	0.51	0.05	-0.02	0.02	0.00
63	CH_3CH_2CHOH* + 2* -> $CH_3CHCHOH$** + H*	-0.25	0.44	0.00	0.00	0.03	0.03
64	CH_3CHCH_2OH** + * -> $CH_3CHCHOH$** + H*	-0.42	0.38	0.05	0.01	0.03	0.01
65	$CH_3CH_2CH_2OH$* + * -> $CH_3CH_2CH_2O$* + H*	-0.28	0.63	0.01	-0.05	-0.01	-0.04
66	$CH_3CH_2CH_2OH$* + * -> CH_3CH_2CHOH* + H*	-0.17	0.49	-0.02	0.00	-0.02	0.02
67	$CH_3CH_2CH_2OH$* + 2* -> CH_3CHCH_2OH** + H*	0.00	0.67	-0.07	-0.10	-0.02	-0.04
68	$CH_3CH_2CH_2OH$ + * -> $CH_3CH_2CH_2OH$*	0.59	N/A	0.01	N/A	-0.01	N/A
69	CH_3CH_2CHO + * -> CH_3CH_2CHO*	0.40	N/A	-0.01	N/A	-0.01	N/A
70	$C_4H_8O_2$ (dioxane) + 2* -> $C_4H_8O_2$**	0.99	N/A	-0.13	N/A	-0.10	N/A

Table 3.2: TOFs (s^{-1}) and surface coverage of the most abundant surface intermediates (divided by the corresponding number of sites occupied of the adsorption on the surface) during the HDO of Pac on Rh (111) surface at a temperature of 473 K under both vapor and liquid phases.

species	**gas phase**	**water (-10%)**	**water (d)**	**water (+10%)**	**dioxane (-10%)**	**dioxane (d)**	**dioxane (+10%)**
free site	1.50×10^{-2}	9.57×10^{-3}	5.68×10^{-3}	4.23×10^{-3}	1.36×10^{-2}	8.30×10^{-3}	6.85×10^{-3}
H*	5.00×10^{-1}	3.17×10^{-1}	1.81×10^{-1}	1.56×10^{-1}	4.84×10^{-1}	2.92×10^{-1}	2.48×10^{-1}

`

CO***	1.61×10^{-1}	2.23×10^{-1}	2.68×10^{-1}	2.76×10^{-1}	1.65×10^{-1}	2.30×10^{-1}	2.46×10^{-1}
CH_3CH_2COO**	1.07×10^{-3}	2.21×10^{-3}	2.61×10^{-3}	3.07×10^{-3}	3.27×10^{-3}	2.93×10^{-3}	2.61×10^{-3}
CH_3CH_2COOH*	2.39×10^{-4}	6.62×10^{-3}	2.45×10^{-3}	6.23×10^{-3}	8.20×10^{-4}	2.68×10^{-3}	3.44×10^{-3}
TOF (s^{-1})	3.43×10^{-5}	8.00×10^{-5}	8.73×10^{-5}	1.17×10^{-4}	3.85×10^{-5}	5.91×10^{-5}	8.81×10^{-5}

Table 3.3: Degrees of rate control of key species under gas and liquid phase conditions at a temperature of 473 K and a gas partial pressure of 1 bar, 0.001 bar and 0.1 bar, respectively, for propionic acid, CO and hydrogen.

Surface species	gas	water (default)	water (+10%)	water (-10%)	1, 4-dioxane (default)	1, 4-dioxane (+10%)	1, 4-dioxane (-10%)
H*	-2.97	-1.34	-1.15	-2.14	-1.96	-1.73	-2.82
CO***	-0.22	-0.77	-0.83	-0.50	-0.55	-0.64	-0.25
CH_3CH_2COO**	-0.02	-0.06	-0.07	-0.05	-0.07	-0.06	-0.07
CH_3CH_2COOH*	N/A	-0.03	-0.07	N/A	-0.03	-0.04	N/A
Step 1	0.96	0.96	0.96	0.96	0.96	0.96	0.96

Table 3.4: Degrees of selectivity control for key species that have impact on propanol production path determined from gas and liquid phase calculations (solvation calculations with ±10% of default COSMO Rh cavity are also included) at a temperature of 473 K.

	Step 51	Step 52	Step 59	Step 60	Step 66	CO***	H*
Gas	-0.34	0.35	N/A	0.01	0.09	0.05	0.05
Water (default)	-0.38	0.37	N/A	N/A	0.02	N/A	0.05
Water (+10%)	-0.31	0.31	N/A	N/A	N/A	N/A	0.04
Water (-10%)	-0.32	0.27	-0.01	N/A	0.05	0.03	0.03
1, 4-dioxane (default)	-0.47	0.43	-0.01	N/A	0.05	0.01	0.06
1, 4-dioxane (+10%)	-0.46	0.44	-0.01	N/A	0.03	N/A	0.07
1, 4-dioxane (-10%)	-0.41	0.23	-0.01	0.01	0.18	0.14	-0.03

Table 3.5: Degrees of selectivity control for key species that have impact on propionaldehyde production path determined from gas and liquid phase calculations (solvation calculations with ±10% of default COSMO Rh cavity are also included) at a temperature of 473 K.

	Step 51	Step 52	Step 59	Step 60	Step 66	CO***	H*
Gas	0.52	-0.41	N/A	-0.01	-0.10	-0.06	-0.06
Water (default)	0.56	-0.55	0.01	N/A	-0.03	N/A	-0.07
Water (+10%)	0.63	-0.63	0.01	N/A	-0.02	0.01	-0.08
Water (-10%)	0.62	-0.52	0.02	-0.02	-0.10	-0.06	-0.06
1, 4-dioxane (default)	0.48	-0.43	0.01	N/A	-0.05	-0.01	-0.07
1, 4-dioxane (+10%)	0.49	-0.47	0.01	N/A	-0.03	N/A	-0.08
1, 4-dioxane (-10%)	0.3	-0.30	0.02	-0.02	-0.23	-0.18	0.04

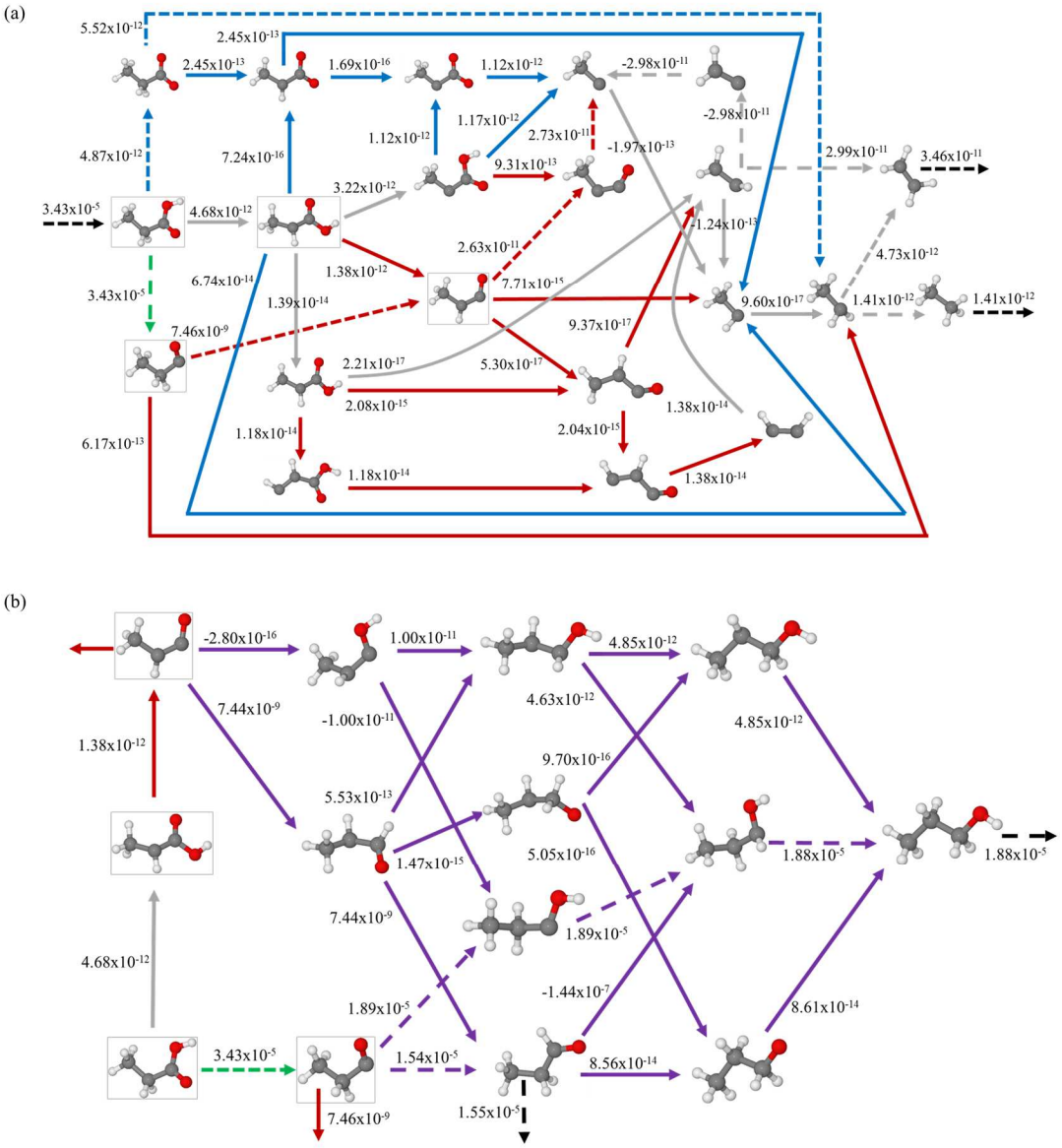

Figure 3.1: TOFs (s^{-1}) of (a) DCX and DCN reaction steps and (b) propanol and propionaldehyde production steps under vapor phase conditions on Rh (111) surface at a temperature of 473 K and a gas partial pressure of propionic acid, CO and hydrogen of 1 bar, 0.001 bar and 0.1 bar, respectively.

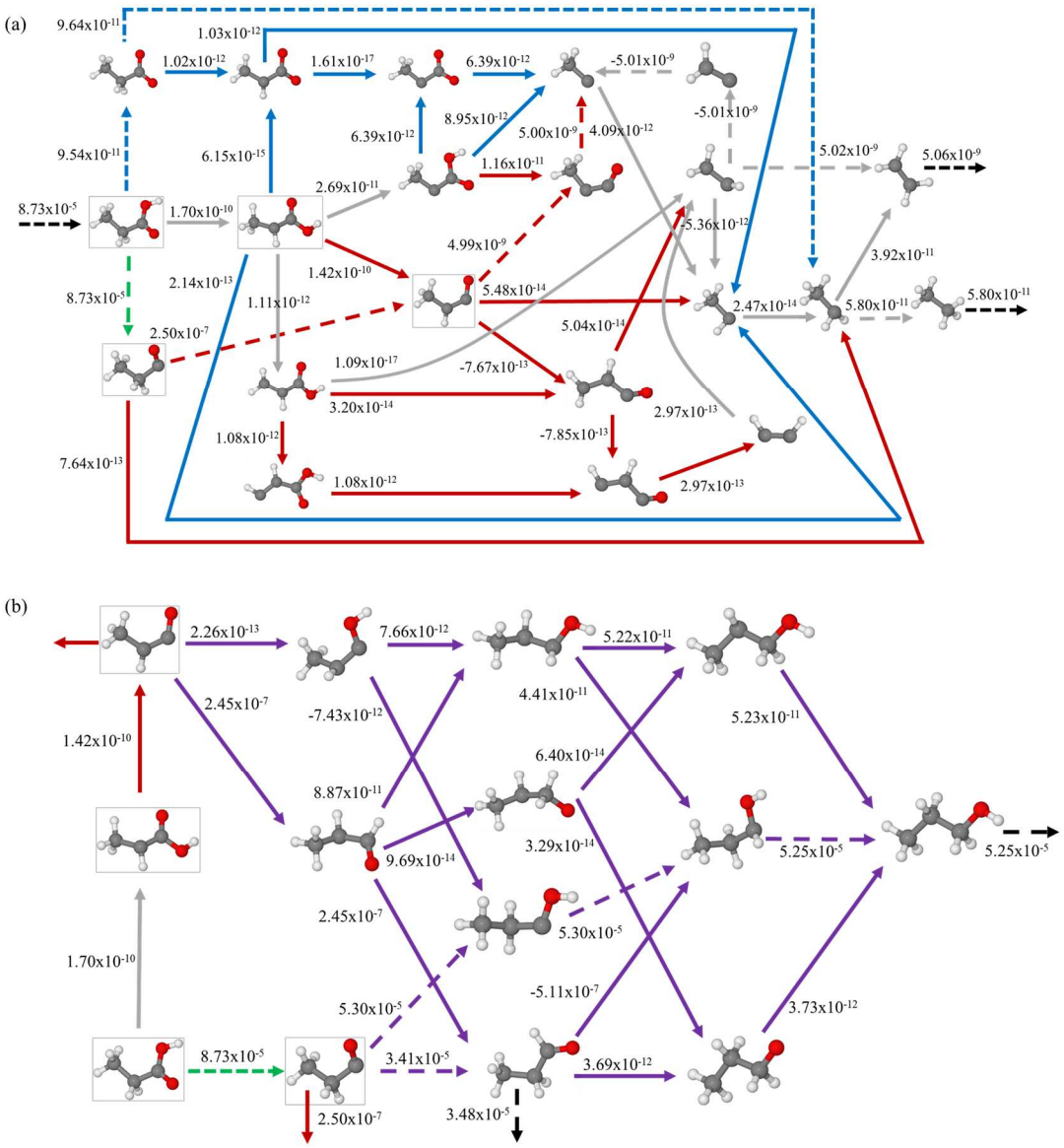

Figure 3.2: TOFs (s^{-1}) of (a) DCX and DCN reaction steps and (b) propanol and propionaldehyde production steps in liquid water on Pt (111) surface at a temperature of 473 K and a gas partial pressure of propionic acid, CO and hydrogen of 1 bar, 0.001 bar and 0.1 bar, respectively.

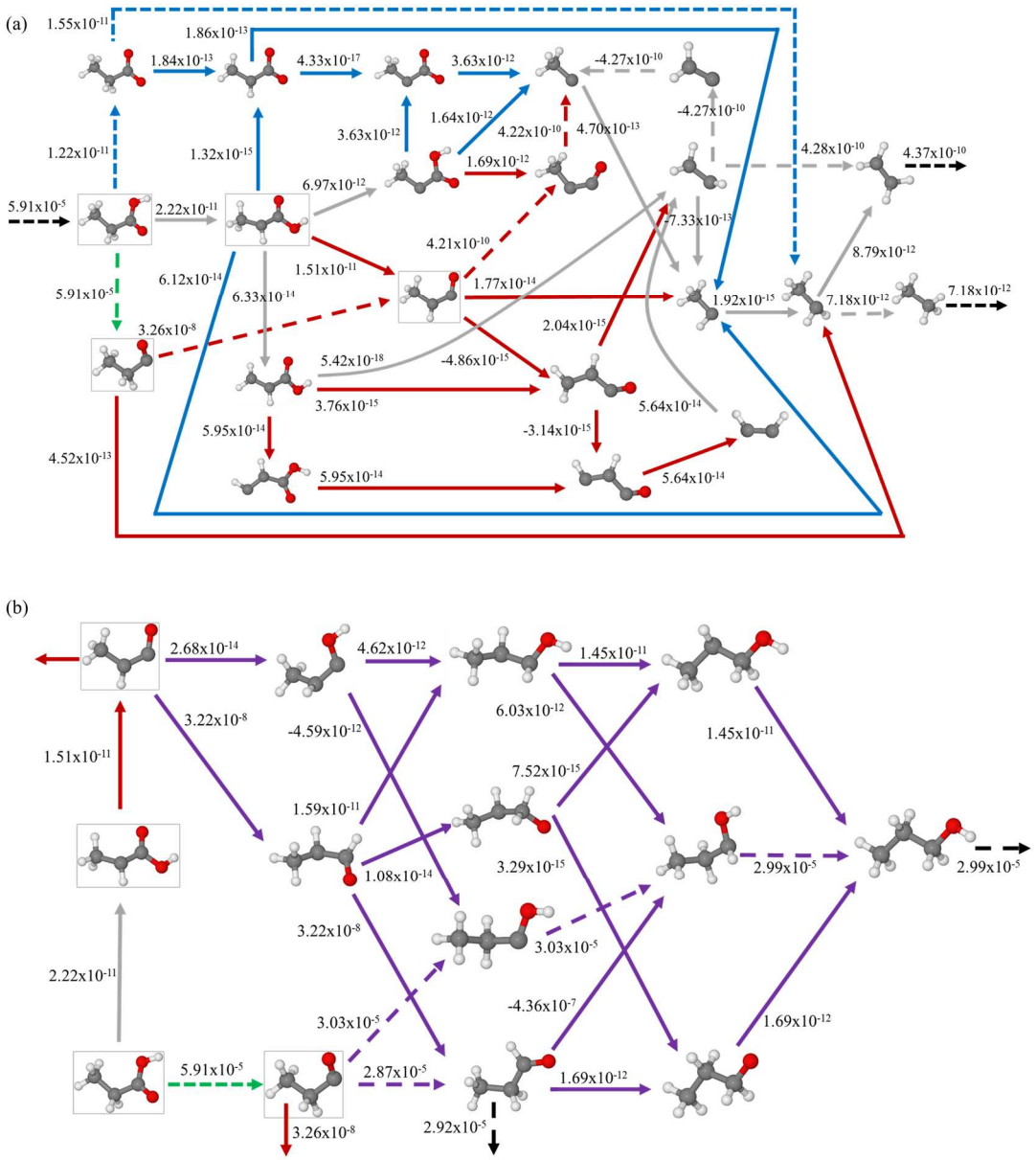

Figure 3.3: TOFs (s^{-1}) of (a) DCX and DCN reaction steps and (b) propanol and propionaldehyde production steps in liquid 1,4-dioxane on Rh (111) surface at a temperature of 473 K and a gas partial pressure of propionic acid, CO and hydrogen of 1 bar, 0.001 bar and 0.1 bar, respectively.

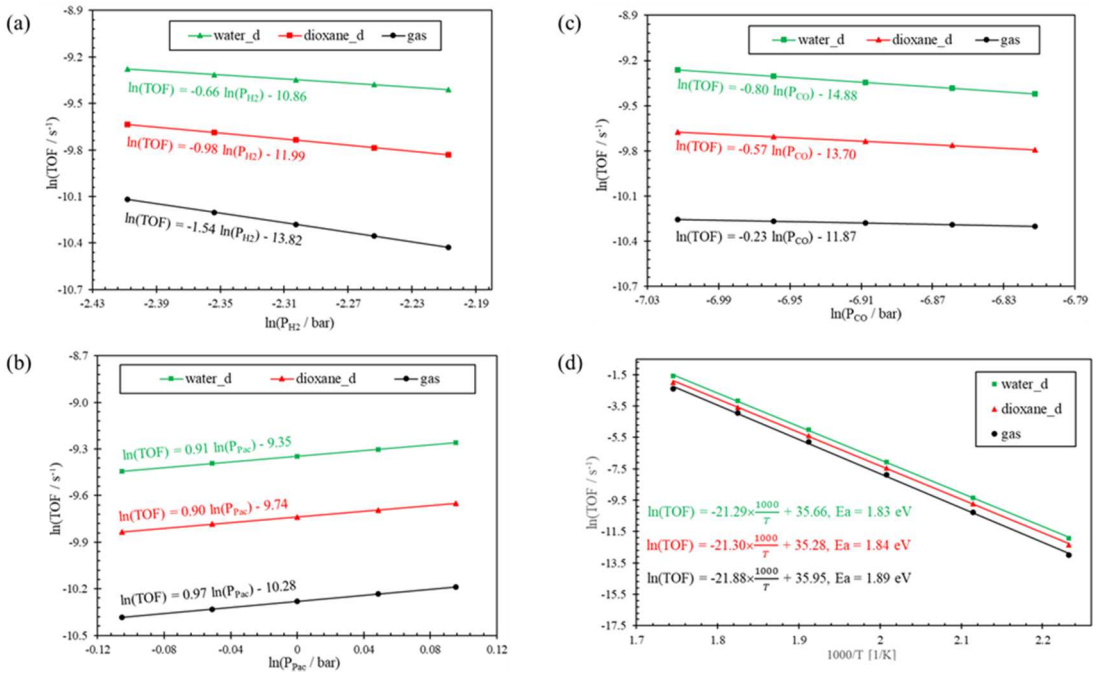

Figure 3.4: Reaction orders of (a) H_2, (b) propionic acid and (c) CO at a temperature of 473 K and (d) Arrhenius plot for the HDO of propionic acid in the temperature range of 448 - 573 K.

3.8 Bibliography

1. P. N. Vennestrom, C. M. Osmundsen, C. H. Christensen and E. Taarning, *Angew Chem Int Ed Engl*, 2011, **50**, 10502-10509.
2. J. R. Regalbuto, *Science*, 2009, **325**, 822-824.
3. M.-A. Perea-Moreno, E. Samerón-Manzano and A.-J. Perea-Moreno, *Sustainability*, 2019, **11**.
4. G. W. Huber, P. O'Connor and A. Corma, *Applied Catalysis A: General*, 2007, **329**, 120-129.
5. P. Gallezot, *Chem Soc Rev*, 2012, **41**, 1538-1558.
6. D. M. Alonso, J. Q. Bond and J. A. Dumesic, *Green Chemistry*, 2010, **12**.
7. G. Knothe, *Fuel Processing Technology*, 2005, **86**, 1059-1070.
8. M. J. Ramos, C. M. Fernandez, A. Casas, L. Rodriguez and A. Perez, *Bioresour Technol*, 2009, **100**, 261-268.
9. J. Monnier, H. Sulimma, A. Dalai and G. Caravaggio, *Applied Catalysis A: General*, 2010, **382**, 176-180.
10. J. C. Serrano-Ruiz and J. A. Dumesic, *Energy Environ. Sci.*, 2011, **4**, 83-99.
11. B. Donnis, R. G. Egeberg, P. Blom and K. G. Knudsen, *Topics in Catalysis*, 2009, **52**, 229-240.
12. D. Kubička, P. Šimáček and N. Žilková, *Topics in Catalysis*, 2008, **52**, 161-168.
13. R. Weingarten, G. A. Tompsett, W. C. Conner and G. W. Huber, *Journal of Catalysis*, 2011, **279**, 174-182.

14. S. G. Wettstein, D. M. Alonso, Y. Chong and J. A. Dumesic, *Energy & Environmental Science*, 2012, **5**.
15. J. Lu, S. Behtash and A. Heyden, *The Journal of Physical Chemistry C*, 2012, **116**, 14328-14341.
16. J. M. Lu, S. Behtash, M. Faheem and A. Heyden, *Journal of Catalysis*, 2013, **305**, 56-66.
17. S. Behtash, J. Lu, C. T. Williams, J. R. Monnier and A. Heyden, *The Journal of Physical Chemistry C*, 2015, **119**, 1928-1942.
18. J. M. Lu, M. Faheem, S. Behtash and A. Heyden, *Journal of Catalysis*, 2015, **324**, 14-24.
19. P. Maki-Arvela, I. Kubickova, M. Snare, K. Eranen and D. Y. Murzin, *Energ Fuel*, 2007, **21**, 30-41.
20. I. Simakova, O. Simakova, P. Mäki-Arvela and D. Y. Murzin, *Catalysis Today*, 2010, **150**, 28-31.
21. I. Simakova, B. Rozmysłowicz, O. Simakova, P. Mäki-Arvela, A. Simakov and D. Y. Murzin, *Topics in Catalysis*, 2011, **54**, 460-466.
22. B. Rozmysłowicz, P. Mäki-Arvela, A. Tokarev, A.-R. Leino, K. Eränen and D. Y. Murzin, *Industrial & Engineering Chemistry Research*, 2012, **51**, 8922-8927.
23. L. Boda, G. Onyestyák, H. Solt, F. Lónyi, J. Valyon and A. Thernesz, *Applied Catalysis A: General*, 2010, **374**, 158-169.
24. Y. Chen, D. J. Miller and J. E. Jackson, *Industrial & Engineering Chemistry Research*, 2007, **46**, 3334-3340.
25. W. Yang, R. V. Solomon, J. Lu, O. Mamun, J. Q. Bond and A. Heyden, *Journal of Catalysis*, 2020, **381**, 547-560.
26. D. A. Colby, R. G. Bergman and J. A. Ellman, *Chem Rev*, 2010, **110**, 624-655.
27. X. Wang, A. Lerchen, T. Gensch, T. Knecht, C. G. Daniliuc and F. Glorius, *Angew Chem Int Ed Engl*, 2017, **56**, 1381-1384.
28. I. D. Gridnev and T. Imamoto, *Acc Chem Res*, 2004, **37**, 633-644.
29. J. C. Lewis, R. G. Bergman and J. A. Ellman, *Acc Chem Res*, 2008, **41**, 1013-1025.
30. H. Olcay, L. Xu, Y. Xu and G. W. Huber, *ChemCatChem*, 2010, **2**, 1420-1424.
31. T. Sperger, I. A. Sanhueza, I. Kalvet and F. Schoenebeck, *Chem Rev*, 2015, **115**, 9532-9586.
32. P. Liu, L. E. Sirois, P. H. Cheong, Z. X. Yu, I. V. Hartung, H. Rieck, P. A. Wender and K. N. Houk, *J Am Chem Soc*, 2010, **132**, 10127-10135.
33. Y. K. Lugo-José, J. R. Monnier and C. T. Williams, *Applied Catalysis A: General*, 2014, **469**, 410-418.
34. S. Behtash, J. Lu, M. Faheem and A. Heyden, *Green Chem.*, 2014, **16**, 605-616.
35. S. Behtash, J. Lu, O. Mamun, C. T. Williams, J. R. Monnier and A. Heyden, *The Journal of Physical Chemistry C*, 2016, **120**, 2724-2736.
36. M. Faheem, S. Suthirakun and A. Heyden, *The Journal of Physical Chemistry C*, 2012, **116**, 22458-22462.
37. O. Mamun, M. Saleheen, J. Q. Bond and A. Heyden, *Journal of Catalysis*, 2019, **379**, 164-179.
38. M. Arend, T. Nonnen, W. F. Hoelderich, J. Fischer and J. Groos, *Applied Catalysis A: General*, 2011, **399**, 198-204.

39. G. Kresse and J. Hafner, *Phys Rev B Condens Matter*, 1993, **47**, 558-561.
40. G. Kresse and J. Furthmuller, *Comp Mater Sci*, 1996, **6**, 15-50.
41. G. Kresse and D. Joubert, *Physical Review B*, 1999, **59**, 1758-1775.
42. J. P. Perdew and Y. Wang, *Phys Rev B Condens Matter*, 1992, **45**, 13244-13249.
43. J. P. Perdew and W. Yue, *Phys Rev B Condens Matter*, 1986, **33**, 8800-8802.
44. J. W. Arblaster, *Platinum Metah Rev.*, 1997, **41**, 184-189.
45. N. L. Haworth, Q. Wang and M. L. Coote, *J Phys Chem A*, 2017, **121**, 5217-5225.
46. H. J. Monkhorst and J. D. Pack, *Physical Review B*, 1976, **13**, 5188-5192.
47. G. Henkelman, B. P. Uberuaga and H. Jonsson, *Journal of Chemical Physics*, 2000, **113**, 9901-9904.
48. R. A. Olsen, G. J. Kroes, G. Henkelman, A. Arnaldsson and H. Jonsson, *J Chem Phys*, 2004, **121**, 9776-9792.
49. A. Heyden, A. T. Bell and F. J. Keil, *J Chem Phys*, 2005, **123**, 224101.
50. G. Henkelman and H. Jonsson, *Journal of Chemical Physics*, 1999, **111**, 7010-7022.
51. I. Chorkendorff and J. W. Niemantsverdriet, *Concepts of modern catalysis and kinetics*, 2017.
52. C. T. Campbell, *ACS Catalysis*, 2017, **7**, 2770-2779.
53. C. T. Campbell, *Journal of Catalysis*, 2001, **204**, 520-524.
54. C. Stegelmann, A. Andreasen and C. T. Campbell, *J Am Chem Soc*, 2009, **131**, 8077-8082.
55. V. Pallassana and M. Neurock, *Journal of Catalysis*, 2002, **209**, 289-305.

`

CHAPTER 4

A COMBINATION OF MACHINE LEARNING METHOD AND FIRST PRINCIPLE CALCULATIONS TO STUDY THE HYDRODEOXYGENATION OF PROPANOIC ACID[3]

[3] Wenqiang Yang, Kareem E. Abdelfatah, Asif J. Chowdhury, Gabriel A. Terejanu, Andreas Heyden. To be submitted to ACS catalysis

`

4.1 Abstract

In a combination of density functional theory calculations and machine learning method, a framework was proposed to identify the rate-controlling species and reaction rate of the hydrodeoxygenation of propionic acid on transition metal surfaces at a DFT level of accuracy with greatly reduced computational cost. A stacked Gaussian process regression model, which use E_{CHCHCO}, E_{OH} and fingerprints as the descriptors for the adsorption energy prediction and E_R_E_{p1}_E_{p2}_FP_R_FP_{P2}_E_{CH3CH} as the descriptors for the transition state energy prediction, can locate exactly the same rate-controlling species and predict the same turnover frequency as that from DFT calculations predictions. Gaussian process model also outperforms the linear ridge regression model that use the same descriptors and the most commonly used transition state scaling model. More importantly, with all surface species adsorption energy being calculated via DFT and the transition state being estimated by linear ridge regression, the predicted rate-controlling species and TOFs agrees well with DFT predictions, demonstrating the importance of the thermodynamics in the kinetic mechanisms.

Keywords: Biomass conversion, Large reaction network, Density functional theory, Machine learning, Gaussian process regression, linear regression, thermodynamics importance

4.2 Introduction

The study of the usage of biomass as an alternative to fossil fuels has greatly increased in popularity due to the environment and climate issues brought by the combustion and conversion of the fossil fuels[1]. However, biomass has its own drawbacks,

`

such as high viscosity, poor oxidation stability, low energy density, and high cloud point temperature due to its high oxygen content, which makes it incompatible to current petrol-based infrastructure and greatly impede its direct commercial applications[2-5]. Deoxygenation therefore becomes very important for the usage of biomass. Currently, the so called hydrodeoxygenation (HDO) process which is conducted in both vapor and liquid phases is widely used for the conversion of biomass to valuable products[6, 7]. However, the conventional heterogeneous catalysts used for the HDO process such as sulfided $NiMo/Al_2O_3$ and $CoMo/Al_2O_3$ have various drawbacks. For instance, short catalyst lifetimes and high sulfur content in the final product have been found[6]. To overcome the limitations of using conventional sulfided catalysts in biomass processing, new catalysts must be developed, which requires a better understanding of the HDO mechanism of biomass. In the meanwhile, however, the reaction network complexity of the biomass conversion which usually involves hundreds of intermediates and thousands of possible reaction steps greatly limits the understanding and modeling of the reaction mechanisms of the biomass conversion both computationally and experimentally. What makes the biomass conversion study in catalysis even more difficult is the fact that the reaction network varies greatly across different catalyst surfaces and active sites, and thus the precise mechanism must be reidentified for every catalyst. Theoretically, microkinetic modeling based on density functional theory (DFT) calculations has been proven to be a very powerful tool in investigating the reaction mechanism in heterogenous catalysis[8, 9], but models proposed mainly considered C_2 molecules or smaller species, and to build a full microkinetic model based on first principle calculations may be possible for biomass conversion but should with a significant amount of computational resource cost.

`

Meanwhile, however, the extreme complexity of reaction networks can be addressed with the concept that most of the reaction steps and intermediates in the network has negligible impact on the final results which can therefore be treated with less accuracy, and the fact that only few key species control the rate of the reaction[8]. Thus, finding a good model for the prediction (estimation) of the properties of the majority of the reaction network and identifying the right species to focus computational and experimental resources on are of paramount importance.

To overcome the computational cost, various semi-empirical methods haven been explored during the past years. One of the most important and also the simplest is the linear scaling relationship, which was firstly proposed by Nørskov, Bligaard and coworkers[10-14]. It relates the adsorption energy of surface intermediate to one or two key descriptors (usually the adsorption energy of small molecules or atomic species such as C, O, OH and CO are used) through a simple linear equation. Besides, the intrinsic properties of the catalyst can also be used as descriptors to predict the adsorption energy of surface intermediates[15-17]. For instance, Reuter and coworkers[15] demonstrated that descriptors being expressed in a nonlinear function of various intrinsic properties of the catalyst, e.g. coordination numbers, d-band moments, and density of states at the Fermi level, are very powerful in predicting the adsorption energy of a wide range of adsorbates over multimetallic transition metal surfaces and facets. However, these methods are usually developed for C_2 molecules or smaller species and each surface intermediates need its own model, which greatly impedes the application of these methods to larger biomass molecules. In order to predict the adsorption energy of large adsorbates, more complicated machine learning models based on group additivity[13, 18-22], 'Coulomb'

`

matrix[23-25], bag-of-bonds[26] and etc. have been proposed recently. However, these methods usually need the adsorption coordinates and adsorbate geometry to achieve a reasonably good prediction accuracy, and currently there is still lack of good models to exactly predict the most stable adsorption configuration of adsorbates on the catalyst surface. To predict the transition state energies, another linear correlation called transition-state scaling relations[27] (TSS) and Brønsted–Evans–Polanyi[28] (BEP) correlations has been used to compute the transition state and activation barriers, respectively, for a family of reactions using the product energy and reaction energy, respectively. Usually, a reaction family is defined based on the bond type that is undergoing breaking (e.g., C-C, C-O, C-H, O-H scission), and correlations are built for each family. This linear relation has been proven to roughly hold true over various of catalyst facets and has been widely used in the computational catalysis community[14, 15, 27-40].

With models being built for the estimation of the properties (adsorption energies of surface intermediates and transition state energies) of the reaction network, to identify the key rate-controlling species and the possible reaction mechanisms without the need to do fully computational calculations of the whole reaction network, descriptor-based, linear-scaling approach has been widely used for computational screening of solid catalysts for reactions that has a small reaction network [38, 41-50]. While for large reaction network, such as biomass conversion reactions, the linear scaling relationship lost its prediction power. Because in order to build the linear scaling relationships that relates all the needed intermediate/transition-state energies to one or two key ‘‘descriptors’’, the energetics of all necessary adsorbed intermediates and transition-states for a set of

`

reference materials need to be computationally calculated by DFT, which requires a huge computational cost for biomass conversions which involves thousands of possible reactions. Additionally, there exists scatter around each of the linear scaling relationships due to real errors in assuming that each energy scales linearly with the descriptor(s), leading to inaccuracies in their energy estimates and thus in the rate predictions. Instead, couple of more complicated machine learning models based on more sophisticated descriptors have been developed recently. For instance, Ulissi and coworkers[49] proposed a framework that is constructed on a Gaussian process based on group additivity fingerprints for the adsorption energies predictions, combined with transition-state scaling relations (TSS) to identify the key species and the most possible reaction mechanisms for the heterogenous catalysis reaction network. The model is interactively used to predict the most important species until all the key species are located and explicitly calculated by DFT. Applying these methods to the reaction of syngas on Rh (111) surface, they identified the most likely reaction mechanism. Similarly, Sutton et al[50] presented a systematic hierarchical multiscale framework based on group additivity and Brønsted–Evans–Polanyi (BEP) relations for parameterization of large microkinetic models. Applying the approach to the moderate size ethanol steam reforming mechanism on Pt, which consist of 67 species and 160 reaction steps, they found that the method delivers first-principles' accuracy at significantly reduced computational cost. Despite the success of these models in determining the reaction mechanism, it still suffers from some intrinsic drawbacks of the models being used to estimate the surface intermediate adsorption energy and transition state energy. Firstly, these methods only work with single metal surface losing the power of screening all possible catalysts. Especially,

`

without the knowledge of the adsorbate geometry on the surface, the group additivity cannot predict the intermediates adsorption energies across catalyst, and there are also no universal rules in categorizing the groups that consist of a molecule. What's more, the usefulness of the widely used simple linear relations (BEP) or TSS on biomass conversion reaction is not clear since biomass usually involves much more complicated chemistry[32, 37, 51]. For instance, Sutton et al.[52] reported that the classic BEP relations is sufficient for C-H but inadequate for O-H and C-OH bond scission for ethanol on Pt (111) and Rh (111) surface, and the similar behavior has also been found by Lee et al. for the C-O scission of methoxy and hydroxyl groups in guaiacol on Pt (111) surface[51]. Alternatively, Wolcott et al[48] recently introduced a degree of rate control approach that focuses instead only on the most relevant energies that most directly control the catalyst's activity. However, they assumed the same rate control species for all the catalysts, which in other words, the predictions from this approach will be much less accurate when the materials are very different.

Previously, we have studied the hydrodeoxygenation (HDO) of the propionic acid on various transition metal (111) surfaces[53]. Using the adsorption energies of CHCHCO and OH as the metal descriptors and fingerprints as the species descriptors, we found that both nonlinear and linear models can give a very good estimation of the adsorption energies of surface intermediates with a MAEs around 0.18 eV, which outperforms the single linear relationship that relates the energies to small species (such as C, O, OH). Similarly, in other work on the prediction of the transition states involved in the HDO of propionic acid[54], we found that with the right combination of the metal descriptors (CHCHCO, OH, CH_3CH), reaction descriptors (reaction energies, reactant energies and

`

product energies) and species descriptors (fingerprints of the reactant and product), both linear and nonlinear models also performs very well in the prediction of transition state energies, and the MAEs of the prediction is much smaller than that of the TSS and BEP relations. We therefore introduced here a framework that based on our previous work to estimate the adsorption energy and transition state energy to explore the reaction mechanism of biomass conversion (HDO of propionic acid was used as the model reaction) with greatly reduced computational cost. We demonstrated the approach on the HDO of the propionic acid on 8 transition metal surfaces, including Pt (111), Pd (111), Ni (111), Cu (111), Rh (111), Ag (111), Re (0001) and Ru (0001). Specifically, we determined the reaction mechanism, rate controlling species and the rate of the reactions. The number of DFT calculations that need to be conducted for key species in order to correctly identify the reaction mechanism are also reported. Finally, we showed the importance of thermodynamics (surface intermediate adsorption energy) in the kinetic analysis.

4.3 Methods

4.3.1 Computational Methods.

All calculations were carried out using the Vienna Ab Initio Simulation Package (VASP)[55, 56] based on density functional theory (DFT) with the projector augmented wave (PAW) method[57]. The generalized gradient approximation (GGA) with the Perdew and Wang 1991 functional (PW91) was used to treat exchange correlation effects[58, 59]. An energy cutoff of 400 eV is used for all DFT calculations and the energy convergence criterion was set to 10^{-7} eV. All structures were relaxed until the Hellmann-Feynman

`

force on each atom were smaller than 0.01 eV $Å^{-1}$. To simulate the surface, a $3 \times 2\sqrt{3}$ (111) surface model was constructed with four metal atom layers separated by a 15 Å vacuum gap. The dipole correction was applied to the direction perpendicular to the surface. For all surface calculations, the bottom two layers were fixed to their bulk positions while the top two layers were fully relaxed in all directions. In the vibrational frequency calculations, however, all metal atoms were fixed at their optimized positions. The Brillouin zone integration was sampled by 4×4×1 k-points for the surface using the Monkhorst-Pack scheme[60]. In order to precisely locate the transition states of the elementary reactions, a combination of the climbing image nudged elastic band (CI-NEB) method and the dimer method was used[61-64]. It should be noted that frequencies below 100 cm^{-1} were shifted to 100 cm^{-1} for the calculation of partition functions in order to minimize the errors associated with the harmonic approximation for small frequencies[65].

4.3.2 Microkinetic Modeling

Adsorption free energies of all intermediates, G_{ads}, have been calculated with a universal reference based on the following equations:

$$G_{ads} = G_{slab+intermediate} - G_{slab} - N_C \times E_C - N_H \times E_H - N_O \times E_O \quad (4.1)$$

$$E_H = 0.5 \times E_{H2} \quad (4.2)$$

$$E_C = E_{CH4} - 2 \times E_{H2} \quad (4.3)$$

$$E_O = E_{H2O} - E_{H2} \quad (4.4)$$

where $G_{slab+intermediate}$ is the free energy of the intermediate on the surface slab, G_{slab} is the free energy of the clean surface slab, and E_{CH4}, E_{H2O}, E_{H2} are the energy of the

`

CH_4, H_2O and H_2 molecules, respectively. N_C, N_H and N_O are the number of C, H and O atoms in the intermediate. Based on the adsorption free energy defined above, the reaction energy and activation energy barrier can be calculated using the following equations:

$$\Delta G_i^{rxn} = \Sigma_j \nu_{ij} \times G^i_{ads,j} \quad (4.5)$$

$$\Delta G_i^{‡} = G^{‡}_{ads,i} - \Sigma\, G^R_{ads,i} \quad (4.6)$$

with ΔG_i^{rxn} and $\Delta G_i^{‡}$ being the reaction free energy and activation free energy of reaction step i, respectively. While ν_{ij} and $G^i_{ads,j}$ are the stoichiometry coefficient and adsorption free energy of intermediates j in reaction step i, respectively. Finally, $G^{‡}_{ads,i}$ and $G^R_{ads,i}$ are the adsorption free energy of the transition state and the sum of the adsorption free energies of the reactant of reaction step i, respectively.

For surface reactions, the forward reaction rate constant (k_{for}) can be calculated according to the transition state theory as,

$$k_{for} = \frac{k_B T}{h} e^{-\frac{\Delta G‡}{k_B T}} \quad (4.7)$$

where k_B is the Boltzmann constant, h is Planck constant, T is the reaction temperature in Kelvin, and $\Delta G‡$ is the zero-point corrected activation barrier for the forward reaction obtained from DFT calculations. For adsorption processes, the reaction rate constant can be approximated through collision theory with a sticking coefficient of 1,

$$k_{for} = \frac{1}{N_0\sqrt{2\pi m_A k_B T}} \quad (4.8)$$

`

where N_0 is the number of sites per surface area (1.454×10^{19} m^{-2}) and m_A denotes the molecular weight of adsorbent A. The reverse reaction rate constant (k_{rev}) is determined from the thermodynamic equilibrium constant K,

$$K = \frac{k_{for}}{k_{rev}} \tag{4.9}$$

With all the forward and reverse reaction rate constants specified, a mean-field microkinetic model was built for the normalized number of surface species i per surface metal atoms[66]. The surface coverage of each species is equal to the number of sites occupied by the species times the normalized number of surface species i per surface metal atoms. Steady state surface coverages and rates are obtained by using the Matlab ODE solver ode15s. No assumptions were made regarding the rate controlling steps in building our models.

4.3.3 Degree of rate control

Campbell's degree of kinetic rate control DRC_i, where i is either one transition state or one surface intermediate, is used to determine the rate-controlling species[67-69]. The degree of rate control is calculated based on the following equations,

$$DRC_i = \left(\frac{\partial \ln r}{\partial \frac{-G_i^0}{RT}} \right)_{G_{j \neq i}^0} \tag{4.16}$$

where the partial derivative is taken holding the free energies of all other species G_j^0 constant. The value of DRC_i describes the relative increase in net rate due to the (differential) stabilization of the standard-state free energy for species i.

`

4.3.4 The iterative algorithm

As shown in Fig. 4.1, algorithm consist of 4 steps in total: (1) predict the surface intermediates adsorption energies with the optimized machine learning model; (2) using the necessary predicted adsorption energies to predict the transition state energies with the optimized models; (3) run the microkinetic model and sensitivity analysis to determine the rate-controlling species, run DFT calculations for these species if they are from model predictions and include these DFT calculated energetics into the microkinetic model, (4) repeat step 1,2 and 3 until all the rate-controlling species are calculated by DFT. The reaction mechanism and the rate of the reaction will then be determined from the last run of the microkinetic model.

4.3.5 The reaction network of the HDO of propionic acid

The detailed reaction network of the HDO of propionic acid consists of decarbonylation (DCN) and decarboxylation (DCX) path is shown in Fig. 4.2. Basically, there are two types of DCN reaction pathways: (1) pathways that start with propionic acid dehydroxylation, $CH_3CH_2COOH^* + {}_3^* \rightarrow CH_3CH_2CO^{***} + OH^*$ and followed by either direct decarbonylation or one step of dehydrogenation prior to the decarbonylation, and (2) pathways that involve α–carbon dehydrogenation prior to the dehydroxylation step that precedes the decarbonylation. For DCX reaction, there are generally three types of relevant reaction pathways: (1) dehydrogenation of the carboxyl group followed by directly α-carbon dehydrogenation or α-carbon dehydrogenation prior to decarboxylation, (2) one or two α-carbon dehydrogenation steps occur before dehydrogenation of the carboxyl group dehydrogenation and the following

`

decarboxylation, (3) both α- and β-carbon dehydrogenation occur before dehydrogenation of the carboxyl group and the following decarboxylation.

4.3.6 Descriptors and models

For surface intermediates adsorption energy prediction, we trained our model with the data of 7 metal surfaces and test on the 8th metal surface. While for the transition state, we trained our model with the data of 5 metal surfaces and test on the 6th metal surfaces since we only have DFT calculated transition states on 6 metal surfaces To compare the nonlinear and linear model, Gaussian process regression and ridge regression model were used since they are among the best model that we have found previously[53, 54]. For the descriptors, a paper-chemistry based fingerprints was used as the species descriptors as shown in Fig. 4.3. In the fingerprints, we first count the total number of different atoms in the molecule, and we also differentiate the atom by the number of unpaired electrons (we assume O and C can have 1 and 3 unpaired electrons at maximum), and lastly we count the number of different bonds in the molecules taking the unpaired electrons of the two atoms forming the bond into consideration (we assume single bond for all the atom-atom connections except for C=O double bond). From principal component analysis (PCA) & varimax rotation, we found that about 98% of the variance of the data can be explained by the adsorption energy of CHCHCO and OH[53]. In a combination with the fingerprints, the MAEs of the predictions for the adsorption energies is 0.127 eV if trained with a Gaussian process model and with the kernel ridge regression, the MAEs is 0.132 eV. Therefore, the adsorption energy of CHCHCO and OH and the fingerprints were used as descriptors for the adsorption energy predictions. For the transition state energy predictions, we found that best descriptors for the linear

`

regression model and the nonlinear regression model are E_R_E_{p1}_E_{p2}_FP_R_FP_{P1}_E_{CH3CH} and E_R_E_{p1}_E_{p2}_FP_R_FP_{P2}_E_{CH3CH}, respectively, where E_R, E_{P1}, E_{P2}, and E_{CH3CH} are the adsorption energy of the reactant of the reaction, the smaller product and the bigger product of the reaction and adsorbed CH_3CH, respectively, while FP_R, FP_{P1} and FP_{P2} are the fingerprints of the reactant, smaller product and bigger product of the reaction, respectively. Therefore, these two descriptors were used for the prediction of the transition state energies in this work.

4.4 Results and Discussion

4.4.1 Energetics predictions

The predictions of the energetics will largely determine the final microkinetic model results, we therefore first report the energetics predictions of different models at the very first cycle. Generally, nonlinear Gaussian process is much better than linear models in predicting the adsorption energies, as show in Fig. 4.4 - 4.9. Except for Cu (111) surface, the predicting MAEs are always smaller than 0.20 eV for the adsorption energy prediction on all the metals surfaces. For linear model, the average MAEs for of the prediction is usually larger than 0.25 eV, and the MAE for the prediction on Cu (111) is extremely large which is larger than 0.35 eV. For the transition state energy prediction, the nonlinear Gaussian process regression outperforms the linear ridge regression model was also found. Specifically, very large prediction errors were found for the transition state scaling (TSS), demonstrating the failure of the linear relation in describing the transition state energy predictions for complicated reactions[32, 37, 51, 52]. The performance

`

of all the models to predict the reaction rate and the ability to identify the rate-controlling species will discussed in more details in the following sections.

4.4.2 Application of the iterative algorithm to the HDO of propionic acid

As shown in Fig. 4.1, we built the microkinetic model with energies from the predictions of the machine learning model, and for each cycle we identify the rate-controlling species (degree of rate control larger than 0.01) and feed the corresponding DFT values back to the models until all the rate-controlling species are calculated by DFT. For the model descriptions, ‘s’ denotes one model was used to predict all the species, ‘r’ means the ridge regression model while ‘g’ denotes Gaussian process regression model. For the descriptors, metal descriptors (CHCHCH plus OH or CHCHCOH) with fingerprints are used as descriptors for the adsorption energy prediction for all the models. For transition state energy predictions, ‘sp’ means the sum of the energy of the product, while ‘all’ is E_R_Ep1_Ep2_F_{PR}_FP_{P2}_E_{CH3CH} as discussed in section 4.3.6, and ‘be’ denotes the descriptor, ER_Ep1_Ep2_FPR_FPP1_ECH3CH. For instance, s_g_s_g_all denotes that a single Gaussian process regression model was used to predict the adsorption energies using metal descriptor (ECHCHCO and EOH) and fingerprints as the input and another single Gaussian process regression model was used to predict the transition state energies using ER_Ep1_Ep2_FPR_FPP2_ECH3CH as the input. Besides, s_g_s_g_all_CH3CH and s_g_s_g_all_CHCHCO are models with descriptors and model type the same as describe before except that E_{CH3CH} and E_{CHCHCO} are used as the metal descriptors, respectively, excluding E_{OH} for the adsorption energy predictions. Generally, for most of the metals, the predicted rate-controlling species converged very fast to the DFT predicted ones by only 2-3 cycles if proper models and

`

descriptors are used. The detailed performance of various models on different metal surfaces will be discussed further in the following sections.

4.4.2.1 Nonlinear model versus linear model

The MAEs of different cycles on the prediction of adsorption energies and transition state energies are shown in Fig. 4.4 – 4.9, respectively for all the six tested metal surfaces. The final predicted rate-controlling species with DFT predicted values and the TOFs from both DFT prediction and machine learning based model predictions are shown in Table 4.1 – 4.6, respectively for the six tested metal surfaces. Generally, the Gaussian process performs extremely well in predicting the rate control species and rate of the reaction for all the tested metals surfaces. Based on the Gaussian process predictions of the adsorption energies and transition state energies, the converged MKM predicts almost the same TOF as the values from DFT predictions, and the most important key species have all been correctly identified with the need of DFT calculations less than 10% of the whole reaction network, demonstrating the great potential of the proposed model to address the large reaction network of the biomass conversions. Interesting, the usage of the best nonlinear model descriptor (s_g_s_g_all in the tables and the figures) and the best linear model descriptors (s_g_s_g_be in the tables and the figures) doesn't have a significant impact on the final converged results if a Gaussian process regression model was used, even though there is a difference in the predicting errors.

We also tested the performance of the linear models that use the same descriptors as that in the Gaussian process regression models. Generally, the linear models can get

`

some good results on some metal surfaces while on some other metals not. For instance, on Ru (0001) and Pd (111) surfaces, linear models using either 'all' or 'be' as descriptors in the transition state energy predictions, the predicted rate of reaction and key species agree very well with DFT predictions. However, for Ru (0001), the reason for the good performance is due to the low prediction errors of the model in predicting both the transition state energies and the adsorption energies, as shown in Fig. 4.7. While for Pd (111), as shown in Table 4.5, a lot of DFT calculations were in need to get a satisfying result. For instance, the total number of transition states and surface species that need to be calculated for the linear model when using 'all' as the descriptor for the transition state (TS) energy prediction are 32 and 21, respectively, and the corresponding numbers for the model using 'be' as the descriptor in TS prediction, are 20 and 11, respectively. Considering that the total transition states and surface species that need to be optimized with DFT calculations for the whole reaction network of the HDO of the propionic acid are 41 and 27, respectively, the linear model doesn't necessary reduce the computational cost greatly in determining the correct key species and may not be a good model for biomass conversion reactions that involves thousands of possible reaction steps and surface species. On Ni (111) and Pt (111) surfaces, linear model can get results close to the DFT predictions, while it is less accurate than the Gaussian process regression models as shown in Table 4.3 and 4.6. Besides, when using TSS for the prediction of the transition state energies, it fails to locate the right key rate-controlling species for all the metals surfaces except that on Pt (111). However, on Pt (111), it needs overall 20 and 13 DFT calculated transition states and surface species, which is much more than that needed by the Gaussian process regression models.

`

In a summary, nonlinear Gaussian process models outperforms the linear ridge regression models and greatly reduced the computational cost in predicting the activity of the transition metal to the hydrodeoxygenation of propionic acid . TSS may not be a very good model in the prediction of the transition states energies in the biomass conversion reactions. In other words, to correctly predict the rate-controlling species and the rate of the reaction with largely reduced computational cost, the right model with the right descriptors must be used.

4.4.2.2 How many descriptors are needed?

For all the models discussed in section 4.3.6, three metal descriptors (catalyst descriptors) are used in the machine learning model. E_{CHCHCO} and E_{OH} are used in the surface intermediates adsorption energy prediction, and E_{CH3CH} is used in the transition state prediction. Therefore, a potential well stablished volcano plot build on this framework that can be used to screen all possible catalyst will have 3 variables in total. From both visualization and the applicability scope, a 4-dimensional volcano plot will be very obscure and useless. Since E_{CH3CH} is the indispensable descriptor in the transition state prediction as we found previously, we tried to reduce the metals descriptors in the adsorption energy predictions. We thus tried to use only E_{CHCHCO} or E_{CH3CH} as the metal descriptors in the adsorption energies prediction while keep the descriptors being used for the TS predictions the same as discussed in section 4.4.2.1, and we used a Gaussian process regression model since it is the best model that we have found as discussed in section 4.4.2.1. We don't consider E_{OH} solely as the metal descriptors in the adsorption energy prediction because neither nonlinear nor linear models can achieve a satisfying

`

estimation of the adsorption energies[53]. So, two models, namely s_g_s_g_all_CHCHCO and s_g_s_g_all_CH_3CH were tested in this work.

The performances of the models using E_{CHCHCO} and E_{CH3CH}, respectively, as the metals descriptors in the adsorption energy predictions, are also shown in Fig. 4.4 - 4.9 and Table 4.1 – 4.6. For all the metals except Cu (111), both the models using E_{CHCHCO} and E_{CH3CH} as metal descriptors predicts the adsorption energies at a similar level of accuracy at convergence, and it also close to the models using both E_{CHCHCO} and E_{OH} as the metals descriptors in the adsorption energy predictions. For Cu (111) surface, the model using E_{CHCHCO} performs much better than the model using E_{CH3CH} as the metal descriptor in prediction the adsorption energies, as shown in Fig. 4.4. However, there is no significant difference in the transition state predictions for these two models since they used the same descriptors in the TS predictions. From Table 4.1, we can find that E_{CHCHCO} model can locate exactly the same rate-controlling species as that found by DFT calculations and predicts a similar TOF, while the E_{CH3CH} model cannot locate both the thermodynamic and kinetic rate-controlling species leading to a very large discrepancy in the predicted TOF. We thus conclude that E_{CHCHCO} is much more important and E_{OH} may not be necessary in the adsorption energy prediction, and what's more a usage of E_{CHCHCO} and E_{CH3CH} may be enough to describe the activity of the activity of transition metals to the HDO of propionic acid.

4.4.2.3 Importance of the thermodynamics

Since both the estimated energetics of the surface intermediates and the transition states were used in the microkinetic model, it is therefore interesting to explore the

`

importance of each of the prediction on the correct determination of the key species and rate of the reactions. Since linear ridge regression model poorly predicts the key species and the rate of the reactions, we thus tried to provide a full DFT calculations of either all the surface intermediates or all the transition states to the linear regression model to study whether its performance could be improved. The used models are s_r_be, s_r_sp and s_r_CHCHCO_OH which corresponds to models using all DFT calculated adsorption energies with 'be' and 'sp' (TSS) as the descriptors for the TS predictions and model using all DFT calculated TS energies with E_{CHCHCO} and E_{OH} as the metal descriptors in predicting the adsorption energies, respectively. As shown in Table 7 -12, with DFT calculated adsorption energies of all the surface intermediates being provide, the linear ridge regression model, which use 'be' as the descriptor in predicting the TS energies, can correctly locate all the rate-controlling species for almost all the metals with few DFT calculated transition states. Even for the TSS relation model, it can achieve a good prediction on the key rate-controlling species and rate of reaction on Ni (111) and Pt (111) surfaces as shown in Table 8 and Table 11, respectively. However, with all the DFT calculated transition states being provided, the linear ridge regression model, which uses E_{CHCHCO} and E_{OH} plus fingerprints as the descriptors in the adsorption energy predictions, generally needs a large fraction of surface intermediates of the whole reaction network being calculated by DFT to obtain a good predictions of the rate-controlling species and the rate of the reactions. Apparently, it is therefore much more important to accurately predict the adsorption energies of the surface intermediates in the kinetic analysis, which agrees very well with previous findings by Sutton et al that thermodynamics is of great importance in kinetic mechanisms indentification[50].

`

4.5 Conclusions

In a combination of density functional theory calculations and machine learning method, a iterative framework was proposed to address the complexity of the reaction network of the biomass conversion. In the iterative cycle, the machine learning model was iteratively used to predict the energetics of surface intermediates and transition states that are to be implemented into a microkinetic model. The microkinetic model was iteratively refined with the DFT calculated key rate-controlling species until all the key species identified were calculated a DFT level of accuracy. For the machine learning model, both nonlinear (Gaussian process) and linear (ridge regression) models were used, and the adsorption energy of CHCHCO, OH and CH_3CH were used as the metals descriptors, a paper chemistry based fingerprints were used as the species descriptors while both the energy of the reactant, product were used as the reaction descriptors. For all the models using E_{CHCHCO} and E_{OH} as the descriptors in the adsorption energy prediction and E_{CH3CH} used in the transition state prediction, the nonlinear Gaussian process regression outperforms the linear ridge regression models in identifying the rate-controlling species and predicting the rate of the reaction. On all the tested 6 metal surfaces, Gaussian process models can predict the rate-controlling species and the TOF of the HDO of propionic acid as that at a DFT level of accuracy with greatly reduced computational cost. However, the widely used TSS cannot correctly locate the key species, and the predicted TOF is in large discrepancy comparing to the DFT predictions. Besides, E_{CHCHCO} was found to be most important metal descriptors in the adsorption energy predictions, and the usage of E_{CHCHCO} and E_{CH3CH} are sufficient to describe the activity of the transition metals to the HDO of propionic acid. Finally, we found that it is

much more important to accurately predict the adsorption energies of the surface intermediates in the kinetic mechanisms, underscoring the importance of the thermodynamics. Overall, in order to correctly identify the key rate-controlling species and predict the rate of the reaction with a high accuracy, the right model and descriptors need to be well stablished, and the framework we proposed could be a good solution to the challenge of the large reaction network of the biomass conversion problems.

4.6 ACKNOWLEDGMENT

We gratefully acknowledge financial support from the U.S. Department of Energy, Office of Basic Energy Science, Catalysis Science program under Award DE-SC0007167 (some of the gas phase data) and the National Science Foundation under Grant No. DMREF-1534260 (some of the gas phase data and models). Computational resources have been provided by the National Energy Research Scientific Computing Center (NERSC) which is supported by the Office of Science of the U.S. Department of Energy and in part by XSEDE under grant number TG-CTS090100. Computational resources from CASCADE cluster from Environmental Molecular Sciences Laboratory (EMSL) under Pacific Northwest National Laboratory (PNNL) are also used for the DFT calculations. Finally, computing resources from the USC High Performance Computing Group are gratefully acknowledged.

`

4.7 Tables and figures

Table 4.1: The predicted rate control species and reaction rate of the HDO of propionic acid on Cu (111) surface from machine learning and DFT calculations with KRC and TRC corresponding to the total number of DFT calculated transition states and surface species used for the machine learning models.

Species	DFT	s_g_s_g all	s_g_s_g be	s_r_s_r all	s_r_s_r be	s_r_s_r sp	s_g_s_g all CHCHCO	s_g_s_g all CH_3CH
CH_3CH_2COO	-0.32	-0.32	-0.32	--	--	--	-0.32	--
H	-2.23	-2.23	-2.23	--	--	--	-2.23	-3.83
TS1	--	--	--	0.96	0.96	0.95	--	0.96
TS5	0.70	0.70	0.70	--	--	--	0.70	--
TS29	0.26	0.26	0.26	--	--	--	0.26	--
KRC	--	10	19	5	4	3	10	7
TRC	--	6	16	1	1	4	6	3
TOF	$4.92x10^{-12}$	$4.92x10^{-12}$	$4.92x10^{-12}$	$9.32x10^{-6}$	$9.33x10^{-6}$	$9.23x10^{-6}$	$4.92x10^{-12}$	$1.69x10^{-14}$

Table 4.2: The predicted rate control species and reaction rate of the HDO of propionic acid on Rh (111) surface from machine learning and DFT calculations with KRC and TRC corresponding to the total number of DFT calculated transition states and surface species used for the machine learning models.

Species	DFT	s_g_s_g all	s_g_s_g be	s_r_s_r all	s_r_s_r be	s_r_s_r sp	s_g_s_g all CHCHCO	s_g_s_g all CH_3CH
$CH_2CHCOOH$	0.05	--	--	--	--	--	--	--
COOH	-0.07	--	--	--	--	--	--	--
CO	-0.98	-0.98	-0.98	--	--	--	-0.98	-0.98
H	-0.87	-0.87	-0.87	-3.70	-3.71	-3.70	-0.87	-0.87
TS1	0.89	0.89	0.89	0.92	0.93	0.96	0.89	0.89
TS5	0.06	0.07	0.07	0.03	0.03	--	0.07	0.07
KRC	--	2	2	3	8	16	2	2
TRC	--	2	2	2	2	8	3	2
TOF	$1.12x10^{-6}$	$1.11x10^{-6}$	$1.11x10^{-6}$	$2.27x10^{-5}$	$2.27x10^{-5}$	$2.15x10^{-5}$	$1.10x10^{-6}$	$1.11x10^{-6}$

`

Table 4.3: The predicted rate control species and reaction rate of the HDO of propionic acid on Ni (111) surface from machine learning and DFT calculations with KRC and TRC corresponding to the total number of DFT calculated transition states and surface species used for the machine learning models.

Species	DFT	s_g_s_g all	s_g_s_g be	s_r_s_r all	s_r_s_r be	s_r_s_r sp	s_g_s_g all CHCHCO	s_g_s_g all CH_3CH
CH_2CH	-0.13	--	--	--	--	--	--	--
CO	-0.57	-0.57	-0.57	N/A	--	--	-0.57	-0.57
H	-2.10	-2.10	-2.10	-3.70	-3.70	-3.70	-2.11	-2.10
TS1	0.93	0.96	0.96	0.96	0.94	0.95	0.96	0.96
TS8	-0.10	--	--	--	--	--	--	--
TS18	-0.06	--	--	--	--	--	--	--
KRC	--	4	3	6	17	9	4	2
TRC	--	3	3	4	7	6	3	2
TOF	$1.18x10^{-8}$	$1.14x10^{-8}$	$1.14x10^{-8}$	$2.92x10^{-8}$	$2.97x10^{-8}$	$2.94x10^{-8}$	$1.16x10^{-8}$	$1.16x10^{-8}$

Table 4.4: The predicted rate control species and reaction rate of the HDO of propionic acid on Ru (0001) surface from machine learning and DFT calculations with KRC and TRC corresponding to the total number of DFT calculated transition states and surface species used for the machine learning models.

Species	DFT	s_g_s_g all	s_g_s_g be	s_r_s_r all	s_r_s_r be	s_r_s_r sp	s_g_s_g all CHCHCO	s_g_s_g all CH_3CH
CH_3CH_2COO	-1.34	-1.33	-1.33	-1.33	-1.33	-1.23	-1.33	-1.33
H	-0.49	-0.48	-0.48	-0.49	-0.49	-0.45	-0.49	-0.49
TS2	0.22	0.23	0.25	0.24	0.24	0.48	0.24	0.23
TS5	0.24	0.25	0.25	0.24	0.24	0.48	0.24	0.24
TS9	0.26	0.24	0.24	0.25	0.25	--	0.25	0.25
TS41	0.24	0.24	0.24	0.23	0.23	--	0.23	0.23
KRC	--	8	13	11	12	17	12	17
TRC	--	5	9	6	6	11	5	9
TOF	$7.67x10^{-6}$	$7.68x10^{-6}$	$7.62x10^{-6}$	$7.50x10^{-6}$	$7.50x10^{-6}$	$1.15x10^{-5}$	$7.48x10^{-6}$	$7.55x10^{-6}$

`

Table 4.5: The predicted rate control species and reaction rate of the HDO of propionic acid on Pd (111) surface from machine learning and DFT calculations with KRC and TRC corresponding to the total number of DFT calculated transition states and surface species used for the machine learning models.

Species	DFT	s_g_s_g all	s_g_s_g be	s_r_s_r all	s_r_s_r be	s_r_s_r sp	s_g_s_g all CHCHCO	s_g_s_g all CH_3CH
CO	-0.61	-0.61	-0.61	-0.61	--	--	-0.61	-0.61
H	-1.12	-1.12	-1.12	-1.12	-2.92	--	-1.12	-1.12
TS1	0.05	0.05	0.05	0.05	0.08	--	0.05	0.05
TS5	0.91	0.91	0.91	0.91	0.88	--	0.90	0.91
TS29	--	--	--	--	--	0.96	--	--
KRC	--	4	4	32	20	1	2	29
TRC	--	2	2	21	11	0	3	18
TOF	$1.14x10^{-11}$	$1.14x10^{-11}$	$1.14x10^{-11}$	$1.14x10^{-11}$	$4.43x10^{-11}$	$3.97x10^{-8}$	$1.14x10^{-11}$	$1.14x10^{-11}$

Table 4.6: The predicted rate control species and reaction rate of the HDO of propionic acid on Pt (111) surface from machine learning and DFT calculations with KRC and TRC corresponding to the total number of DFT calculated transition states and surface species used for the machine learning models.

Species	DFT	s_g_s_g all	s_g_s_g be	s_r_s_r all	s_r_s_r be	s_r_s_r sp	s_g_s_g all CHCHCO	s_g_s_g all CH_3CH
CO	-0.34	-0.34	-0.34	--	--	--	-0.34	-0.34
H	-1.86	-1.86	-1.86	-2.85	-2.86	-2.90	-1.86	-1.87
TS1	0.06	0.05	0.05	0.06	0.08	0.07	0.05	0.05
TS2	0.16	N/A	N/A	--	0.16	0.17	--	--
TS5	0.74	0.90	0.90	0.90	0.73	0.68	0.91	0.89
KRC	--	7	6	7	9	20	6	5
TRC	--	3	2	3	3	13	6	3
TOF	$3.25x10^{-8}$	$3.93x10^{-8}$	$3.90x10^{-8}$	$6.33x10^{-8}$	$5.33x10^{-8}$	$5.59x10^{-8}$	$3.91x10^{-8}$	$3.99x10^{-8}$

Table 4.7 The predicted rate control species and reaction rate based on machine learning predictions on Pt (111) surface with all adsorption energies or transition state energies being calculated by DFT.

Species	DFT	org_ads_pre_ts		pre_ads_org_ts
		s_r_be	s_r_sp	s_r CHCHCO_OH
CO	-0.61	-0.61	-0.60	--
H	-1.12	-1.12	-1.10	-2.93
TS1	0.05	0.05	--	0.08
TS5	0.91	0.91	--	0.88
TS29	--	--	0.96	--
KRC	--	2	1	--
TRC	--	--	--	11
TOF	$1.14x10^{-11}$	$1.13x10^{-11}$	$3.95x10^{-11}$	$4.44x10^{-11}$

`

Table 4.8 The predicted rate control species and reaction rate based on machine learning predictions on Ni (111) surface with all adsorption energies or transition state energies being calculated by DFT.

Species	DFT	org_ads_pre_ts		pre_ads_org_ts
		s_r_be	s_r_sp	s_r CHCHCO_OH
CH_2CH	-0.13	--	--	--
CO	-0.57	-0.57	-0.57	-0.56
H	-2.10	-2.10	-2.10	-2.13
TS1	0.93	0.96	0.96	0.90
TS8	-0.10	--	--	-0.03
TS18	-0.06	--	--	-0.02
KRC	--	3	1	--
TRC	--	--	--	25
TOF	$1.18x10^{-8}$	$1.14x10^{-8}$	$1.14x10^{-8}$	$1.20x10^{-8}$

Table 4.9 The predicted rate control species and reaction rate based on machine learning predictions on Cu (111) surface with all adsorption energies or transition state energies being calculated by DFT.

Species	DFT	org_ads_pre_ts		pre_ads_org_ts
		s_r_be	s_r_sp	s_r CHCHCO_OH
CH_3CH_2COO	-0.32	-0.32	-0.32	--
H	-2.23	-2.23	-2.22	-2.88
TS1	--	--	--	--
TS5	0.70	0.70	0.71	0.70
TS29	0.26	0.26	0.26	0.26
KRC	--	5	33	--
TRC	--	--	--	12
TOF	$4.92x10^{-12}$	$4.92x10^{-12}$	$4.93x10^{-12}$	$7.27x10^{-12}$

Table 4.10 The predicted rate control species and reaction rate based on machine learning predictions on Rh (111) surface with all adsorption energies or transition state energies being calculated by DFT.

Species	DFT	org_ads_pre_ts		pre_ads_org_ts
		s_r_be	s_r_sp	s_r CHCHCO_OH
$CH_2CHCOOH$	0.05	--	--	--
COOH	-0.07	--	--	0.01
CO	-0.98	-0.97	-0.75	-0.98
H	-0.87	-0.87	-0.67	-0.87
TS1	0.89	0.89		0.90
TS5	0.06	0.07	0.96	0.07
KRC	--	4	9	--
TRC	--	--	--	18
TOF	$1.12x10^{-6}$	$1.10x10^{-6}$	$7.73x10^{-8}$	$1.12x10^{-6}$

`

Table 4.11 The predicted rate control species and reaction rate based on machine learning predictions on Pt (111) surface with all adsorption energies or transition state energies being calculated by DFT.

Species	DFT	org_ads_pre_ts		pre_ads_org_ts
		s_r_be	s_r_sp	s_r CHCHCO_OH
CO	-0.34	-0.34	-0.44	--
H	-1.86	-1.86	-2.40	-2.86
TS1	0.06	0.06	--	0.08
TS2	0.16	0.16	0.05	0.16
TS5	0.74	0.74	--	0.73
TS7	--	--	0.91	--
TS6	--	--	--	-0.39
TS8	--	--	--	-0.35
KRC	--	6	5	--
TRC	--	--	--	5
TOF	3.25×10^{-8}	3.25×10^{-8}	9.47×10^{-9}	5.33×10^{-8}

Table 4.12 The predicted rate control species and reaction rate based on machine learning predictions on Ru (0001) surface with all adsorption energies or transition state energies being calculated by DFT.

Species	DFT	org_ads_pre_ts		pre_ads_org_ts
		s_r_be	s_r_sp	s_r CHCHCO_OH
CH_3CH_2COO	-1.34	-1.24	-1.24	-1.34
H	-0.49	-0.45	-045	-0.49
TS2	0.22	0.45	0.45	0.22
TS5	0.24	0.48	0.48	0.24
TS9	0.26	--	--	0.26
TS41	0.24	--	--	0.24
TS31	--	0.02	0.02	--
TS32	--	0.08	--	--
KRC	--	5	7	--
TRC	--	--	--	5
TOF	7.67×10^{-6}	1.16×10^{-5}	1.18×10^{-5}	7.67×10^{-6}

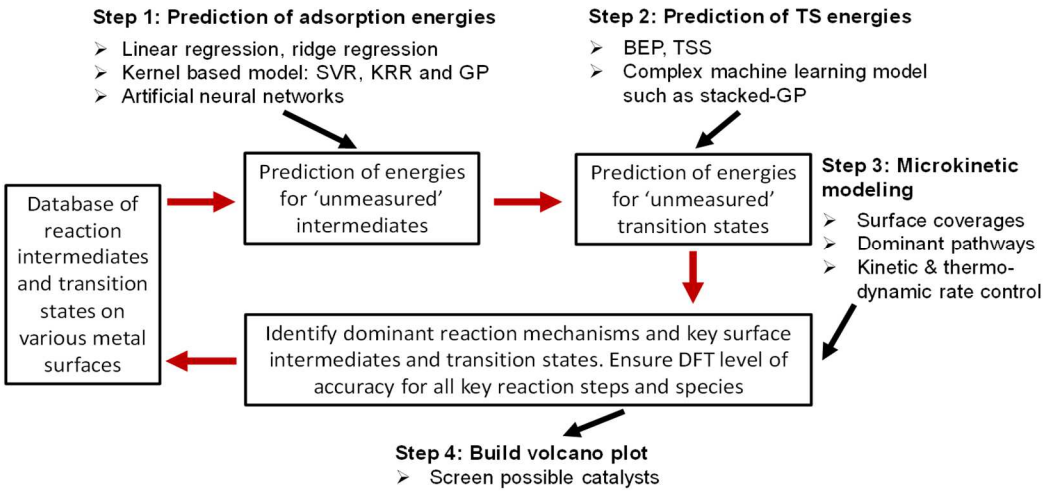

Figure 4.1: A schematic representation of the machine learning based iteratively looping cycle that used to identify the reaction mechanisms and turnover frequency of the reactions.

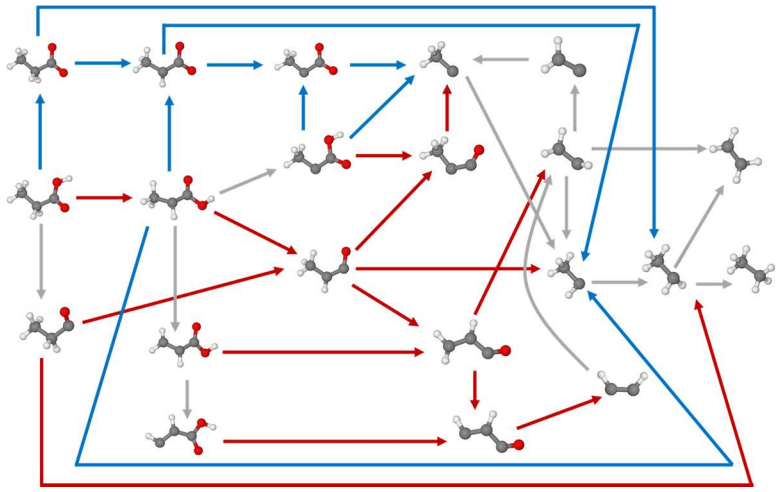

Figure 4.2: The reaction network of the HDO of propionic acid with reactions involved in DCN path being shown in red arrows and that for the DCX path being shown in blue arrows while gray arrows show the reactions involved in both the DCX and DCN path.

`

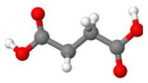

Chemical formula: $COOHCH_2CH_2COOH$

SMILES: OC(=O)[C-1]CC(=O)O

H	C	O	O^0	O^1	C^0	C^1	C^2	C^3	C-H	$C-O^0$	$C-O^1$	C=O	O-H
5	4	4	4	0	3	1	0	0	3	2	0	2	2

C^0-C^0	C^0-C^1	C^0-C^2	C^0-C^3	C^1-C^1	C^1-C^2	C^1-C^3	C^2-C^2	C^2-C^3	C^3-C^3
1	2	0	0	0	0	0	0	0	0

Figure 4.3: A list of fingerprints that is used to represent $COOHCHCH_2COOH$ molecules.

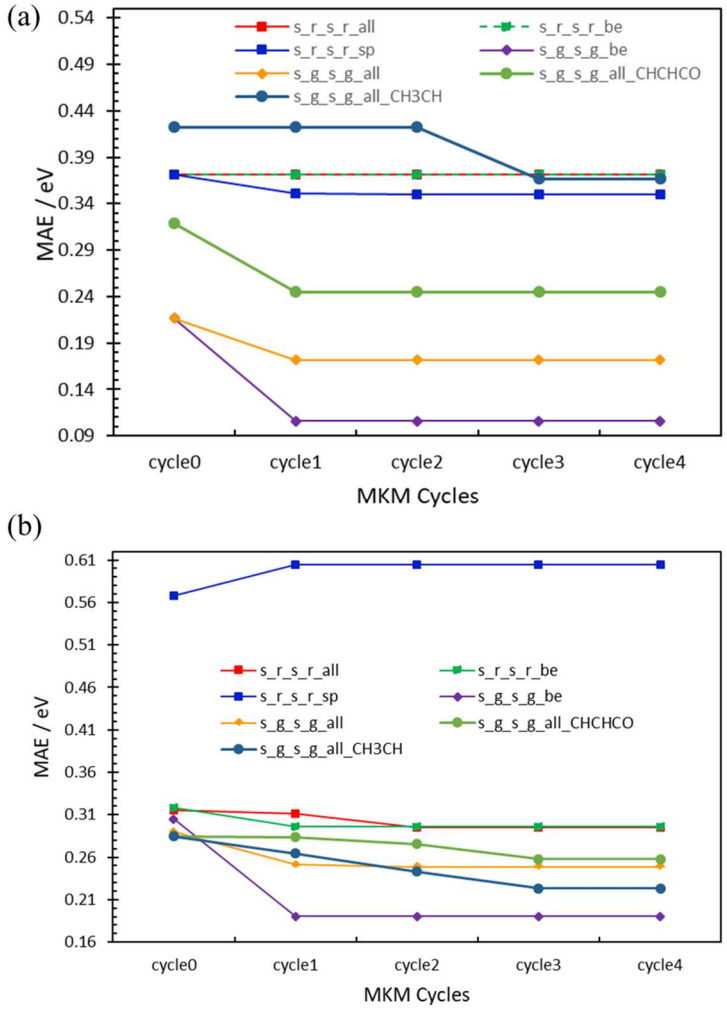

Figure 4.4: The MAEs for the prediction of (a) the adsorption energy of surface species and (b) the transition state energy that involved in the hydrodeoxygenation of the propionic acid on Cu (111) surface at each microkinetic model cycle.

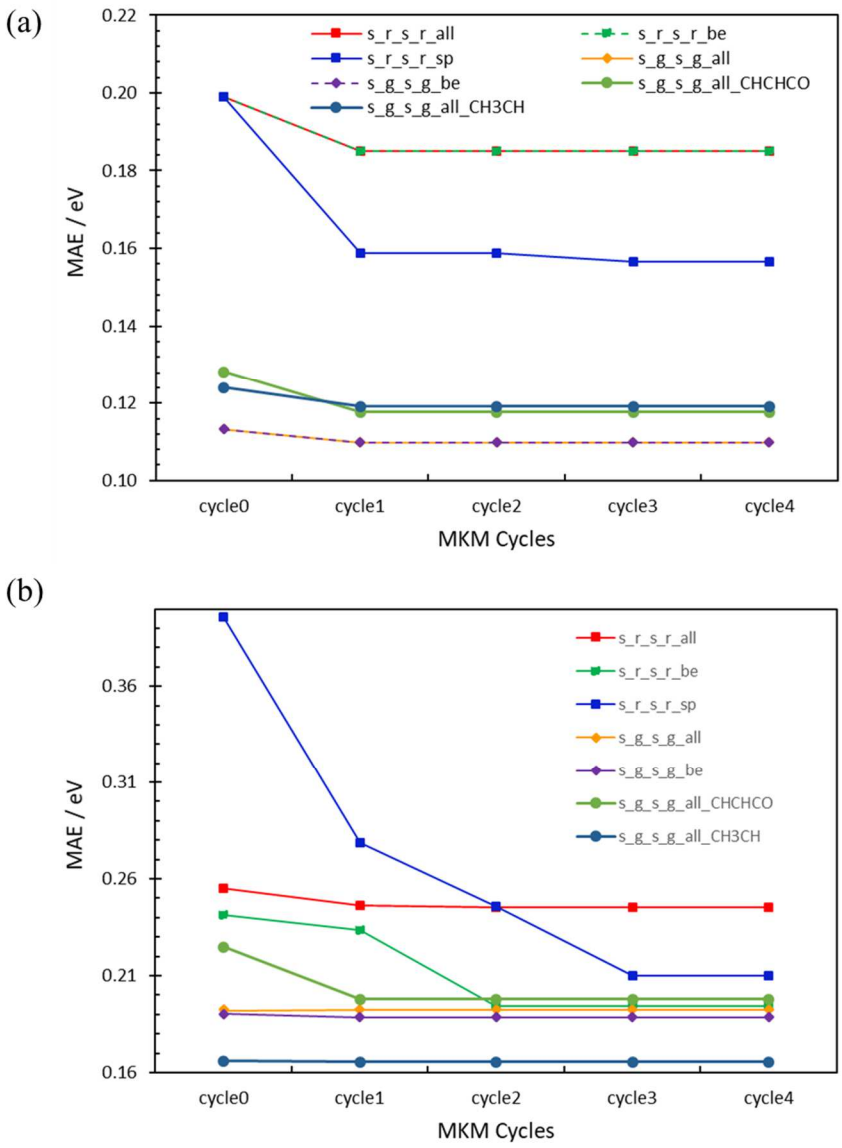

Figure 4.5: The MAEs for the prediction of (a) the adsorption energy of surface species and (b) the transition state energy that involved in the hydrodeoxygenation of the propionic acid on Rh (111) surface at each microkinetic model cycle.

(a)

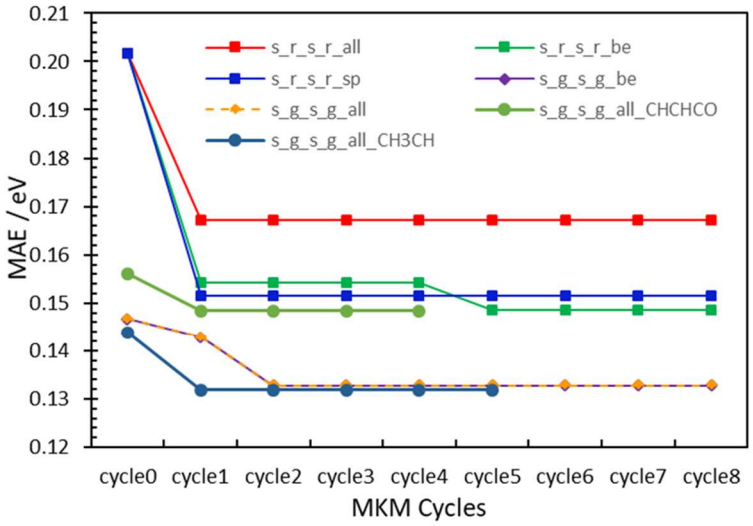

(b)

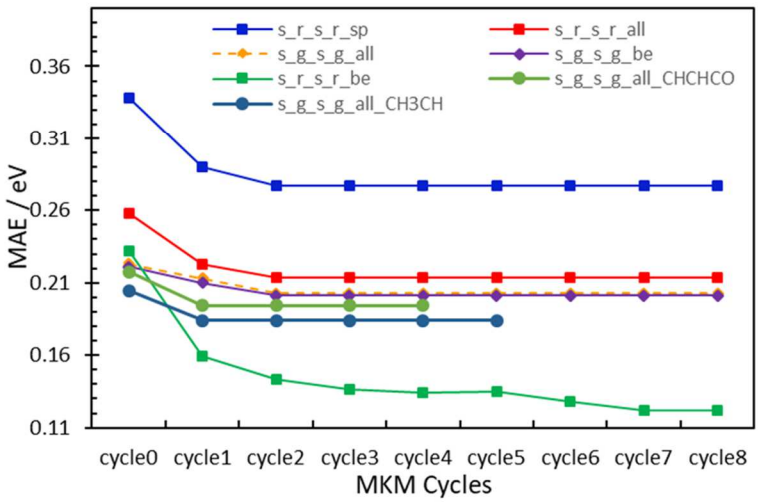

Figure 4.6: The MAEs for the prediction of (a) the adsorption energy of surface species and (b) the transition state energy that involved in the hydrodeoxygenation of the propionic acid on Ni (111) surface at each microkinetic model cycle.

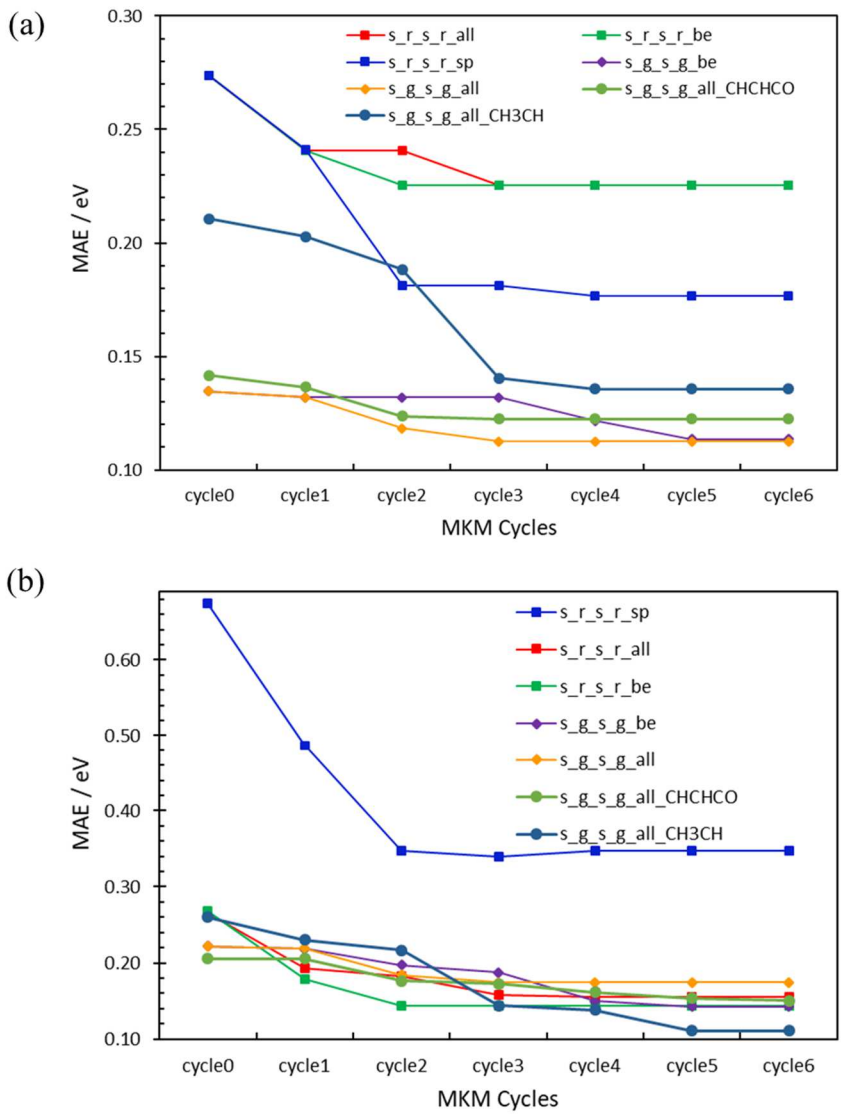

Figure 4.7: The MAEs for the prediction of (a) the adsorption energy of surface species and (b) the transition state energy that involved in the hydrodeoxygenation of the propionic acid on Ru (0001) surface at each microkinetic model cycle.

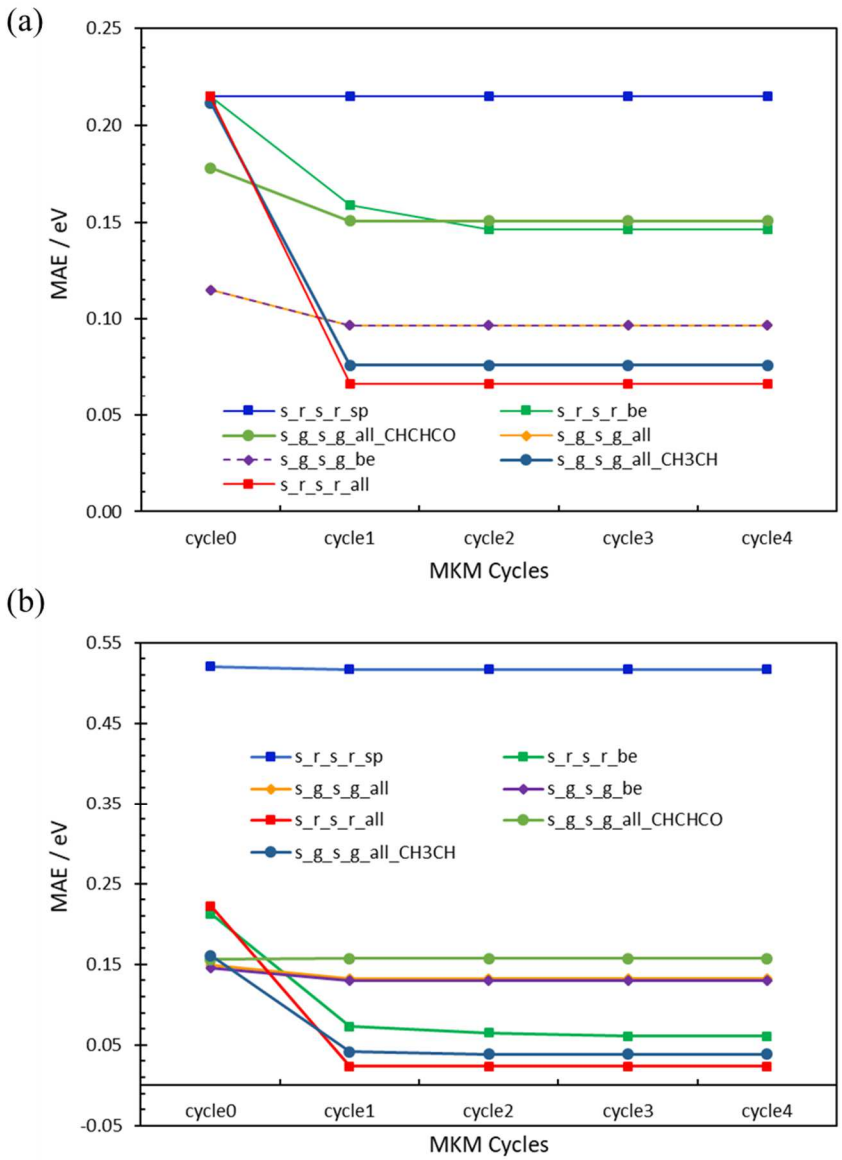

Figure 4.8: The MAEs for the prediction of (a) the adsorption energy of surface species and (b) the transition state energy that involved in the hydrodeoxygenation of the propionic acid on Pd (111) surface at each microkinetic model cycle.

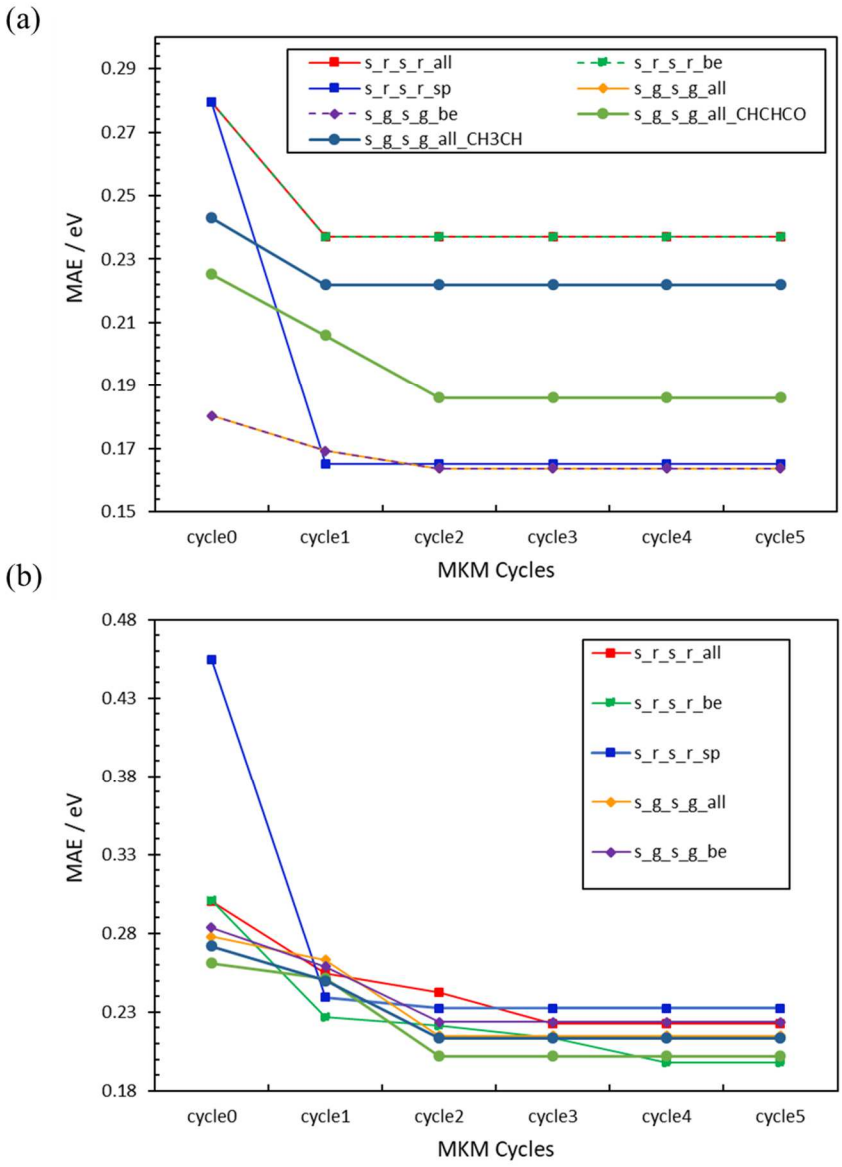

Figure 4.9: The MAEs for the prediction of (a) the adsorption energy of surface species and (b) the transition state energy that involved in the hydrodeoxygenation of the propionic acid on Pt (111) surface at each microkinetic model cycle.

4.8 Bibliography

1. D. M. Alonso, J. Q. Bond and J. A. Dumesic, *Green Chemistry*, 2010, **12**, 1493.
2. J. J. Bozell and G. R. Petersen, *Green Chemistry*, 2010, **12**, 539.
3. D. J. Braden, C. A. Henao, J. Heltzel, C. C. Maravelias and J. A. Dumesic, *Green Chemistry*, 2011, **13**, 1755.
4. J. N. Chheda, G. W. Huber and J. A. Dumesic, *Angew Chem Int Ed Engl*, 2007, **46**, 7164-7183.
5. P. Gallezot, *Chem Soc Rev*, 2012, **41**, 1538-1558.

`

6. P. Gallezot, *ChemSusChem*, 2008, **1**, 734-737.
7. H. Wang, J. Male and Y. Wang, *ACS Catalysis*, 2013, **3**, 1047-1070.
8. I. Chorkendorff and J. W. Niemantsverdriet, *Concepts of modern catalysis and kinetics*, 2017.
9. H. Olcay, L. Xu, Y. Xu and G. W. Huber, *ChemCatChem*, 2010, **2**, 1420-1424.
10. F. Abild-Pedersen, J. Greeley, F. Studt, J. Rossmeisl, T. R. Munter, P. G. Moses, E. Skulason, T. Bligaard and J. K. Norskov, *Phys Rev Lett*, 2007, **99**, 016105.
11. E. M. Fernandez, P. G. Moses, A. Toftelund, H. A. Hansen, J. I. Martinez, F. Abild-Pedersen, J. Kleis, B. Hinnemann, J. Rossmeisl, T. Bligaard and J. K. Norskov, *Angew Chem Int Ed Engl*, 2008, **47**, 4683-4686.
12. G. Jones, F. Studt, F. Abild-Pedersen, J. K. Nørskov and T. Bligaard, *Chemical Engineering Science*, 2011, **66**, 6318-6323.
13. V. Vorotnikov and D. G. Vlachos, *The Journal of Physical Chemistry C*, 2015, **119**, 10417-10426.
14. J. Greeley, *Annu Rev Chem Biomol Eng*, 2016, **7**, 605-635.
15. M. Andersen, S. V. Levchenko, M. Scheffler and K. Reuter, *ACS Catalysis*, 2019, **9**, 2752-2759.
16. F. Calle-Vallejo, D. Loffreda, M. T. Koper and P. Sautet, *Nat Chem*, 2015, **7**, 403-410.
17. Z. Li, X. Ma and H. Xin, *Catalysis Today*, 2017, **280**, 232-238.
18. S. W. Benson and J. H. Buss, *The Journal of Chemical Physics*, 1958, **29**, 546-572.
19. H. K. Eigenmann, D. M. Golden and S. W. Benson, *The Journal of Physical Chemistry*, 1973, **77**, 1687-1691.
20. G. H. Gu and D. G. Vlachos, *The Journal of Physical Chemistry C*, 2016, **120**, 19234-19241.
21. N. Guo, S. Caratzoulas, D. J. Doren, S. I. Sandler and D. G. Vlachos, *Energy & Environmental Science*, 2012, **5**, 6703.
22. M. Salciccioli, Y. Chen and D. G. Vlachos, *The Journal of Physical Chemistry C*, 2010, **114**, 20155-20166.
23. M. Rupp, A. Tkatchenko, K. R. Muller and O. A. von Lilienfeld, *Phys Rev Lett*, 2012, **108**, 058301.
24. M. Rupp, R. Ramakrishnan and O. A. von Lilienfeld, *The Journal of Physical Chemistry Letters*, 2015, **6**, 3309-3313.
25. B. Huang and O. A. von Lilienfeld, *J Chem Phys*, 2016, **145**, 161102.
26. K. Hansen, F. Biegler, R. Ramakrishnan, W. Pronobis, O. A. von Lilienfeld, K. R. Muller and A. Tkatchenko, *J Phys Chem Lett*, 2015, **6**, 2326-2331.
27. S. Wang, V. Petzold, V. Tripkovic, J. Kleis, J. G. Howalt, E. Skulason, E. M. Fernandez, B. Hvolbaek, G. Jones, A. Toftelund, H. Falsig, M. Bjorketun, F. Studt, F. Abild-Pedersen, J. Rossmeisl, J. K. Norskov and T. Bligaard, *Phys Chem Chem Phys*, 2011, **13**, 20760-20765.
28. R. A. van Santen, M. Neurock and S. G. Shetty, *Chem Rev*, 2010, **110**, 2005-2048.
29. T. Bligaard, J. K. Nørskov, S. Dahl, J. Matthiesen, C. H. Christensen and J. Sehested, *Journal of Catalysis*, 2004, **224**, 206-217.

30. J. Cheng, P. Hu, P. Ellis, S. French, G. Kelly and C. M. Lok, *The Journal of Physical Chemistry C*, 2008, **112**, 1308-1311.
31. S. Wang, B. Temel, J. Shen, G. Jones, L. C. Grabow, F. Studt, T. Bligaard, F. Abild-Pedersen, C. H. Christensen and J. K. Nørskov, *Catalysis Letters*, 2010, **141**, 370-373.
32. S. Wang, V. Vorotnikov, J. E. Sutton and D. G. Vlachos, *ACS Catalysis*, 2014, **4**, 604-612.
33. A. J. Medford, A. Vojvodic, J. S. Hummelshøj, J. Voss, F. Abild-Pedersen, F. Studt, T. Bligaard, A. Nilsson and J. K. Nørskov, *Journal of Catalysis*, 2015, **328**, 36-42.
34. J. Zaffran, C. Michel, F. Delbecq and P. Sautet, *Catalysis Science & Technology*, 2016, **6**, 6615-6624.
35. P. N. Plessow and F. Abild-Pedersen, *The Journal of Physical Chemistry C*, 2015, **119**, 10448-10453.
36. A. Michaelides, Z. P. Liu, C. J. Zhang, A. Alavi, D. A. King and P. Hu, *J Am Chem Soc*, 2003, **125**, 3704-3705.
37. J. Zaffran, C. Michel, F. Auneau, F. Delbecq and P. Sautet, *ACS Catalysis*, 2014, **4**, 464-468.
38. A. H. Motagamwala, M. R. Ball and J. A. Dumesic, *Annu Rev Chem Biomol Eng*, 2018, **9**, 413-450.
39. R. B. Sandberg, M. H. Hansen, J. K. Nørskov, F. Abild-Pedersen and M. Bajdich, *ACS Catalysis*, 2018, **8**, 10555-10563.
40. J. K. Nørskov, T. Bligaard, A. Logadottir, S. Bahn, L. B. Hansen, M. Bollinger, H. Bengaard, B. Hammer, Z. Sljivancanin, M. Mavrikakis, Y. Xu, S. Dahl and C. J. H. Jacobsen, *Journal of Catalysis*, 2002, **209**, 275-278.
41. D. Loffreda, F. Delbecq, F. Vigne and P. Sautet, *Angew Chem Int Ed Engl*, 2009, **48**, 8978-8980.
42. L. C. Grabow, F. Studt, F. Abild-Pedersen, V. Petzold, J. Kleis, T. Bligaard and J. K. Norskov, *Angew Chem Int Ed Engl*, 2011, **50**, 4601-4605.
43. A. Nandy, J. Zhu, J. P. Janet, C. Duan, R. B. Getman and H. J. Kulik, *ACS Catalysis*, 2019, **9**, 8243-8255.
44. Y. Wang, L. Xiao, Y. Qi, M. Mahmoodinia, X. Feng, J. Yang, Y. A. Zhu and Chen, *Phys Chem Chem Phys*, 2019, **21**, 19269-19280.
45. W. Guo, M. Stamatakis and D. G. Vlachos, *ACS Catalysis*, 2013, **3**, 2248-2255.
46. P. Deshlahra and E. Iglesia, *The Journal of Physical Chemistry C*, 2016, **120**, 16741-16760.
47. M. Jaraíz, J. E. Rubio, L. Enríquez, R. Pinacho, J. L. López-Pérez and A. Lesarri, *ACS Catalysis*, 2019, **9**, 4804-4809.
48. C. A. Wolcott, A. J. Medford, F. Studt and C. T. Campbell, *Journal of Catalysis*, 2015, **330**, 197-207.
49. Z. W. Ulissi, A. J. Medford, T. Bligaard and J. K. Norskov, *Nat Commun*, 2017, **8**, 14621.
50. J. E. Sutton and D. G. Vlachos, *Chemical Engineering Science*, 2015, **121**, 190-199.
51. K. Lee, G. H. Gu, C. A. Mullen, A. A. Boateng and D. G. Vlachos, *ChemSusChem*, 2015, **8**, 315-322.

52. J. E. Sutton and D. G. Vlachos, *ACS Catalysis*, 2012, **2**, 1624-1634.
53. A. J. Chowdhury, W. Yang, E. Walker, O. Mamun, A. Heyden and G. A. Terejanu, *The Journal of Physical Chemistry C*, 2018, **122**, 28142-28150.
54. K. Abdelfatah, W. Yang, R. Vijay Solomon, B. Rajbanshi, A. Chowdhury, M. Zare, S. K. Kundu, A. Yonge, A. Heyden and G. Terejanu, *The Journal of Physical Chemistry C*, 2019, **123**, 29804-29810.
55. G. Kresse and J. Hafner, *Phys Rev B Condens Matter*, 1993, **47**, 558-561.
56. G. Kresse and J. Furthmuller, *Comp Mater Sci*, 1996, **6**, 15-50.
57. G. Kresse and D. Joubert, *Physical Review B*, 1999, **59**, 1758-1775.
58. J. P. Perdew and Y. Wang, *Phys Rev B Condens Matter*, 1992, **45**, 13244-13249.
59. J. P. Perdew and W. Yue, *Phys Rev B Condens Matter*, 1986, **33**, 8800-8802.
60. H. J. Monkhorst and J. D. Pack, *Physical Review B*, 1976, **13**, 5188-5192.
61. G. Henkelman, B. P. Uberuaga and H. Jonsson, *Journal of Chemical Physics*, 2000, **113**, 9901-9904.
62. G. Henkelman and H. Jonsson, *Journal of Chemical Physics*, 1999, **111**, 7010-7022.
63. R. A. Olsen, G. J. Kroes, G. Henkelman, A. Arnaldsson and H. Jonsson, *J Chem Phys*, 2004, **121**, 9776-9792.
64. A. Heyden, A. T. Bell and F. J. Keil, *J Chem Phys*, 2005, **123**, 224101.
65. N. L. Haworth, Q. Wang and M. L. Coote, *J Phys Chem A*, 2017, **121**, 5217-5225.
66. T. S. Tomoshige Nitta, Masayuki Kuro-oka, Takashi Katayama, *JOURNAL OF CHEMICAL ENGINEERING OF JAPAN*, 1984, **17**, 39-45.
67. C. T. Campbell, *ACS Catalysis*, 2017, **7**, 2770-2779.
68. C. T. Campbell, *Journal of Catalysis*, 2001, **204**, 520-524.
69. C. Stegelmann, A. Andreasen and C. T. Campbell, *J Am Chem Soc*, 2009, **131**, 8077-8082.

`

CHAPTER 5

CONCLUSIONS

The overall objective of this thesis is to theoretically investivgate the reaction mechanims of the hydrodeoxygenaton of propioinc acid on the transition metal surfaces, including the dominant pathways, rate control species, reaction orders and the apparent activation energy. A density functional theory (DFT) based calculations were conducted on the Pt (111) and Rh (111) surface to study the hydrodeoxygenation of the propionic acid. While, a combination of machine learning method and DFT calculations was used to study the reactions on 6 transition metals surfaces at a greatly reduced computational resources cost since a full DFT calculations for large reaction network that usually involved in biomass conversion is not realistic.

Firstly, microkinetic models based on transition state theory and DFT have been developed for the investigation of the HDO of propionic acid over Pt (111) surface under both vapor and liquid phase conditions. In all reaction environments, decarboxylation is not favored. In the gas phase, both decarbonylation products and propanol and propionaldehyde can be produced. However, propanol and propionaldehyde production is favored over decarbonylation products in liquid phase. Under both vapor and liquid phase conditions, the dominant pathway for decarbonylation is the direct path which starts with dehydroxylation of adsorbed propionic acid, followed by α-carbon dehydrogenation and then either direct decarbonylation or further dehydrogenation prior to decarbonylation.

`

Propanol and propionaldehyde production also favor a direct formation pathway which starts with direct dehydroxylation and hydrogenation of the carbonyl group. Only the propionaldehyde production mechanism changes in liquid phase. Here, the propanol production is significantly favored such that propionaldehyde is primarily produced from dehydrogenated surface alcohol species. In liquid 1,4-dioxane and at 473 K, the conversion rate of propionic acid is predicted to increase by one order of magnitude. Higher temperatures further increase the solvent acceleration on the turnover frequency. In liquid water and at 473 K, the propionic acid consumption rate is not significantly increased, primarily because of strong adsorption of propionic acid which leads to the surface being partially blocked by propionic acid. With increasing temperature, however, the TOF is dramatically increased in liquid water and becomes even larger than that in liquid 1,4-dioxane as the surface is much less covered by propionic acid at these temperatures. The rate of the reaction is solely controlled by the dehydroxylation of adsorbed propionic acid under both vapor and liquid phase conditions. The rate of the decarbonylation mechanism is barely affected by the solvents and the increase in propionic acid conversion due to the presence of a solvent primarily originates from an increase in the rate of propanol and propionaldehyde production. Thus, solvents can be designed to manipulate the selectivity of the HDO of organic acids.

In the second part of this work, based on the similar method as that on Pt (111) surface, the HDO of propionic acid over a Rh (111) surface has been systematically studied under both vapor and liquid phase conditions. In all reaction environments, both decarbonylation and decarboxylation are not favored demonstrating that Rh (111) surface may not be the active site for DCN and DCX reaction. Propanol and propionaldehyde

`

production dominantly occur during the HDO of propionic acid on Rh (111) surface, and the dominant pathways for propanol and propionaldehyde production favor a direct formation pathway which starts with direct dehydroxylation and followed by the hydrogenation of the carbonyl group. The dominant pathways of the reaction remain unchanged in the liquid phase while the rate of the reaction was slightly increased by the solvent. Larger Rh cavity radius used in the liquid phase calculations further increase the solvent acceleration on the turnover frequency. Generally, the promotion effect of water is much stronger than 1,4-dioxane on the rate of the reaction. The rate of the reaction is solely controlled by the dehydroxylation of adsorbed propionic acid under both vapor and liquid phase conditions. The selectivity of the main products (propanol and propionaldehyde) is almost the same in all reaction environments. Thus, solvents (at least water and 1,4-dioxane) cannot be designed to manipulate the selectivity of the HDO of organic acids over Rh (111) surface.

Finally, in a combination of density functional theory calculations and machine learning method, a iterative framework was proposed to address the complexity of the reaction network of the biomass conversion. In the iterative cycle, the machine learning model was iteratively used to predict the energetics of surface intermediates and transition states that are to be implemented into a microkinetic model. The microkinetic model was iteratively refined with the DFT calculated key rate-controlling species until all the key species identified were calculated a DFT level of accuracy. For the machine learning model, both nonlinear (Gaussian process) and linear (ridge regression) models were used, and the adsorption energy of CHCHCO, OH and CH_3CH were used as the metals descriptors, a paper chemistry based fingerprints were used as the species

`

descriptors while both the energy of the reactant, product were used as the reaction descriptors. For all the models using E_{CHCHCO} and E_{OH} as the descriptors in the adsorption energy prediction and E_{CH3CH} used in the transition state prediction, the nonlinear Gaussian process regression outperforms the linear ridge regression models in identifying the rate-controlling species and predicting the rate of the reaction. On all the tested 6 metal surfaces, Gaussian process models can predict the rate-controlling species and the TOF of the HDO of propionic acid as that at a DFT level of accuracy with greatly reduced computational cost. However, the widely used TSS cannot correctly locate the key species, and the predicted TOF is in large discrepancy comparing to the DFT predictions. Besides, E_{CHCHCO} was found to be most important metal descriptors in the adsorption energy predictions, and the usage of E_{CHCHCO} and E_{CH3CH} are sufficient to describe the activity of the transition metals to the HDO of propionic acid. Finally, we found that it is much more important to accurately predict the adsorption energies of the surface intermediates in the kinetic mechanisms, underscoring the importance of the thermodynamics. Overall, in order to correctly identify the key rate-controlling species and predict the rate of the reaction with a high accuracy, the right model and descriptors need to be well stablished, and the framework we proposed could be a good solution to the challenge of the large reaction network of the biomass conversion problems.

`

APPENDIX A

SUPPORTING INFORMATION FOR UNRAVELING THE MECHANISM OF THE HYDRODEOXYGENATION OF PROPIONIC ACID OVER A PT (111) SURFACE IN VAPOR AND LIQUID PHASES[4]

[4] W. Yang, R.V. Solomon, J. Lu, O. Mamun, J.Q. Bond and A. Heyden. Journal of Catalysis, 2020, 381, 547-560.

Reprinted here with permission of publisher.

`

Table A.1: Reaction free energies in eV of all elementary reaction steps in the HDO of PAc on a Pt (111) surface at a temperature of 473 K in the vapor phase and in the presence of liquid water and 1,4-dioxane with 10% increase of the default COSMO Pt cavity radius in the solvation calculations, and The number of * signifies the number of adsorption sites.

#	Reaction	Gas		Water		1-4-dioxane	
		ΔG_{rxn}	$\Delta G^{‡}$	$\Delta\Delta G_{rxn}$	$\Delta\Delta G^{‡}$	$\Delta\Delta G_{rxn}$	$\Delta\Delta G^{‡}$
0	CH_3CH_2COOH (g) + * -> CH_3CH_2COOH*	0.79	N/A	-0.30	N/A	-0.22	N/A
1	CH_3CH_2COOH* + 3* -> CH_3CH_2CO*** + OH*	0.52	0.70	0.08	0.06	0.08	0.05
2	CH_3CH_2COOH* + 2* -> $CH_3CHCOOH$** + H*	-0.21	0.72	-0.03	-0.08	0.01	-0.03
3	CH_3CH_2CO*** -> CH_3CH_2* + CO* + *	-0.74	1.47	-0.13	-0.07	-0.07	-0.07
4	CH_3CH_2CO*** -> CH_3CHCO** + H*	-0.29	0.71	-0.06	-0.09	-0.02	-0.04
5	$CH_3CHCOOH$** + * -> CH_3CHCO** + OH*	0.44	0.78	0.05	0.09	0.05	0.08
6	$CH_3CHCOOH$** + 2*-> $CH_2CHCOOH$*** + H*	-0.29	0.67	0.00	-0.04	0.01	0.01
7	$CH_3CHCOOH$** + 2* -> CH_3CCOOH*** + H*	-0.10	0.74	-0.02	0.00	-0.02	-0.02
8	CH_3CHCO** + * -> CH_3CH** + CO*	-0.54	0.84	-0.10	-0.01	-0.06	-0.01
9	CH_3CHCO** + 2* -> CH_3CCO*** + H*	-0.31	0.65	-0.01	-0.03	0.01	0.00
10	CH_3CHCO** + 2* -> CH_2CHCO*** + H*	0.06	0.87	-0.03	-0.12	0.00	-0.06
11	$CH_2CHCOOH$*** + * -> CH_2CHCO*** + OH*	0.78	1.47	0.02	0.08	0.03	0.07
12	$CH_2CHCOOH$*** + * -> $CHCHCOOH$*** + H*	-0.07	0.77	-0.04	-0.09	-0.03	-0.05
13	CH_3CCOOH*** + * -> CH_3CCO*** + OH*	0.23	0.77	0.06	0.09	0.08	0.09
14	CH_3CCO*** -> CH_3C* +CO* + *	-1.18	0.75	-0.10	0.03	-0.06	0.02
15	CH_2CHCO*** + * -> CH_2CH*** + CO*	-0.89	0.69	-0.10	0.00	-0.06	-0.01
16	CH_2CHCO*** + 2* -> $CHCHCO$**** + H*	-0.20	0.61	-0.01	-0.06	0.00	-0.02
17	$CHCHCOOH$*** + 2* -> $CHCHCO$**** + OH*	0.65	1.09	0.05	0.08	0.07	0.08
18	$CHCHCO$**** -> $CHCH$*** + CO*	-0.82	0.51	-0.11	0.03	-0.08	0.02
19	CH_2CH*** + * -> $CHCH$*** + H*	-0.13	0.69	-0.03	-0.08	-0.01	-0.05
20	CH_2CH_2** + 2* -> CH_2CH*** + H*	-0.05	0.69	-0.04	-0.10	-0.02	-0.05
21	CH_2CH*** -> CH_2C** + H*	-0.38	0.38	0.00	-0.02	0.01	-0.01
22	CH_3C* + 2* -> CH_2C** + H*	0.27	1.06	-0.02	-0.11	0.00	-0.07
23	CH_3CH** + 2* -> CH_2CH*** + H*	-0.29	0.51	-0.03	-0.12	-0.01	-0.07
24	CH_3CH** -> CH_3C* + H*	-0.94	0.25	-0.01	-0.04	0.01	-0.02
25	CH_3CH_2* + 2* -> CH_3CH** + H*	-0.10	0.66	-0.03	-0.08	-0.01	-0.05
26	CH_3CH_3* + *-> CH_3CH_2* + H*	-0.11	0.64	-0.03	-0.08	0.00	-0.03
27	CH_3CH_2* + 2* -> CH_2CH_2** + H*	-0.34	0.57	-0.02	-0.10	0.00	-0.06
28	CH_3CH_2COOH* + 2* -> CH_3CH_2COO** + H*	-0.41	0.31	0.12	0.10	0.10	0.06
29	CH_3CH_2COO** -> CH_3CH_2* + CO_2*	-0.09	1.49	-0.04	0.00	-0.02	0.01
30	CH_3CH_2COO** + 2* -> CH_3CHCOO*** + H*	0.47	1.24	-0.10	-0.17	-0.03	-0.08
31	$CH_3CHCOOH$** + 2* -> CH_3CHCOO*** + H*	0.27	0.75	0.05	0.03	0.06	0.04
32	$CH_3CHCOOH$** + 2* -> CH_3CH** + COOH**	-0.04	1.42	-0.08	-0.05	-0.03	-0.03
33	CH_3CHCOO*** -> CH_3CH** + CO_2*	-0.66	0.95	0.03	0.08	0.00	0.03
34	CH_3CHCOO*** + * -> CH_3CCOO*** + H*	-0.22	1.04	-0.07	-0.03	-0.04	-0.01
35	CH_3CCOOH*** + * -> CH_3CCOO*** + H*	0.15	0.90	0.00	0.09	0.04	0.09
36	CH_3CCOOH*** + * -> CH_3C* + COOH**	-0.89	1.06	-0.06	0.03	0.00	0.05
37	$CH_2CHCOOH$*** + 2*->CH_2CH*** +COOH**	-0.04	1.86	-0.10	-0.01	-0.05	0.01
38	CH_3CCOO*** -> CH_3C* + CO_2* +*	-1.38	0.79	0.09	0.18	0.05	0.10
39	COOH** -> CO_2* + H*	-0.35	0.45	0.16	0.06	0.09	0.03
40	COOH** -> CO* + OH*	-0.06	0.46	0.02	0.08	0.02	0.06
41	H_2O* + * -> OH* + H*	0.53	0.83	0.11	0.08	0.08	0.06
42	CH_3CH_3 (g) + * -> CH_3CH_3*	0.57	N/A	-0.08	N/A	-0.06	N/A
43	CH_2CH_2 (g) + 2* -> CH_2CH_2**	-0.27	N/A	-0.12	N/A	-0.07	N/A
44	H_2O (g) + * -> H_2O*	0.52	N/A	-0.20	N/A	-0.13	N/A
45	CO_2 (g) + * -> CO_2*	0.54	N/A	-0.11	N/A	-0.08	N/A
46	CHCH (g) + 3* -> CHCH***	-1.56	N/A	-0.19	N/A	-0.10	N/A

`

47	CO (g) + * -> CO*	-0.59	N/A	-0.16	N/A	-0.10	N/A
48	H_2 (g) + 2* -> H* + H*	-0.36	N/A	0.00	N/A	0.00	N/A
49	CH_3CHCHO*** -> CH_3CHCO** + H*	-0.92	0.08	0.03	0.01	0.01	0.00
50	CH_3CHCOH*** -> CH_3CHCO** + H*	-0.26	0.60	0.00	0.01	0.00	0.00
51	CH_3CH_2CHO* + 3* -> CH_3CH_2CO*** + H*	-0.87	0.18	0.14	0.09	0.09	0.07
52	CH_3CH_2COH* + 3* -> CH_3CH_2CO*** + H*	-0.25	0.04	0.05	0.03	0.04	0.03
53	CH_3CH_2CHO* + 3* -> CH_3CHCHO*** + H*	-0.24	0.69	0.05	0.00	0.06	0.03
54	CH_3CHCH_2O*** + * ->CH_3CHCHO*** + H*	-0.67	-0.06	0.00	-0.03	0.01	-0.02
55	$CH_3CHCHOH$** + 2* -> CH_3CHCHO*** + H*	0.15	0.50	0.04	0.04	0.04	0.04
56	CH_3CH_2COH* + 3* -> CH_3CHCOH*** + H*	-0.28	1.07	-0.01	-0.17	0.01	-0.11
57	$CH_3CHCHOH$** + 2* -> CH_3CHCOH*** + H*	-0.51	0.45	0.07	0.03	0.05	0.01
58	$CH_3CH_2CH_2O$* + * -> CH_3CH_2CHO* + H*	-0.63	0.02	-0.12	-0.03	-0.08	-0.01
59	CH_3CH_2CHOH* + * -> CH_3CH_2CHO* + H*	0.14	0.69	-0.10	-0.01	-0.06	-0.01
60	CH_3CH_2CHOH* + * -> CH_3CH_2COH* + H*	-0.48	0.28	-0.01	0.01	0.00	0.02
61	$CH_3CH_2CH_2O$* + 3* -> CH_3CHCH_2O*** + H*	-0.20	0.69	-0.08	-0.13	-0.03	-0.07
62	CH_3CHCH_2OH** + 2* ->CH_3CHCH_2O*** + H*	0.24	0.58	0.11	0.12	0.10	0.10
63	CH_3CH_2CHOH* + 2* -> $CH_3CHCHOH$** + H*	-0.25	0.74	-0.09	-0.11	-0.04	-0.06
64	CH_3CHCH_2OH** + * -> $CH_3CHCHOH$** + H*	-0.58	0.51	0.07	-0.15	0.06	-0.11
65	$CH_3CH_2CH_2OH$* + * -> $CH_3CH_2CH_2O$* + H*	0.35	0.71	0.03	0.05	0.05	0.05
66	$CH_3CH_2CH_2OH$* + * -> CH_3CH_2CHOH* + H*	-0.41	0.46	0.01	-0.04	0.02	-0.02
67	$CH_3CH_2CH_2OH$* + 2* ->CH_3CHCH_2OH** + H*	-0.09	0.78	-0.15	-0.17	-0.08	-0.10
68	$CH_3CH_2CH_2OH$ (g) + * -> $CH_3CH_2CH_2OH$*	0.66	N/A	-0.19	N/A	-0.15	N/A
69	CH_3CH_2CHO (g) + * -> CH_3CH_2CHO*	0.70	N/A	-0.28	N/A	-0.19	N/A
70	$C_4H_8O_2$ (dioxane) + 2* -> $C_4H_8O_2$**	1.07	N/A	-0.35	N/A	-0.25	N/A

Table A.2: Reaction free energies in eV of all the elementary reaction steps in the HDO of PAc on a Pt (111) surface at a temperature of 473 K in the vapor phase and in the presence of liquid water and 1,4-dioxane with 10% decrease of the default COSMO Pt cavity radius in the solvation calculations, and the number of * signifies the number of adsorption sites.

#	Reaction	Gas		Water		1-4-dioxane	
		ΔG_{rxn}	$\Delta G^{\ddagger}$	$\Delta\Delta G_{rxn}$	$\Delta\Delta G^{\ddagger}$	$\Delta\Delta G_{rxn}$	$\Delta\Delta G^{\ddagger}$
0	CH_3CH_2COOH (g) + * -> CH_3CH_2COOH*	0.79	N/A	-0.24	N/A	-0.19	N/A
1	CH_3CH_2COOH* + 3* -> CH_3CH_2CO*** + OH*	0.52	0.70	0.03	0.02	0.07	0.02
2	CH_3CH_2COOH* + 2* -> $CH_3CHCOOH$** + H*	-0.21	0.72	-0.04	-0.08	0.03	-0.02
3	CH_3CH_2CO*** -> CH_3CH_2* + CO* + *	-0.74	1.47	-0.13	-0.02	-0.10	-0.03
4	CH_3CH_2CO*** -> CH_3CHCO** + H*	-0.29	0.71	-0.04	-0.08	-0.02	-0.04
5	$CH_3CHCOOH$** + * -> CH_3CHCO** + OH*	0.44	0.78	0.03	0.08	0.01	0.03
6	$CH_3CHCOOH$** + 2* ->$CH_2CHCOOH$*** + H*	-0.29	0.67	0.03	-0.04	0.01	-0.01
7	$CH_3CHCOOH$** + 2* -> CH_3CCOOH*** + H*	-0.10	0.74	0.00	0.02	-0.03	-0.03
8	CH_3CHCO** + * -> CH_3CH** + CO*	-0.54	0.84	-0.13	0.03	-0.07	0.02
9	CH_3CHCO** + 2* -> CH_3CCO*** + H*	-0.31	0.65	-0.04	-0.03	-0.01	-0.01
10	CH_3CHCO** + 2* -> CH_2CHCO*** + H*	0.06	0.87	-0.04	-0.09	0.00	-0.04
11	$CH_2CHCOOH$*** + * -> CH_2CHCO*** + OH*	0.78	1.47	-0.04	0.04	0.00	0.04
12	$CH_2CHCOOH$*** + * -> $CHCHCOOH$*** + H*	-0.07	0.77	-0.08	-0.09	-0.06	-0.05
13	CH_3CCOOH*** + * -> CH_3CCO*** + OH*	0.23	0.77	-0.01	0.04	0.03	0.05
14	CH_3CCO*** -> CH_3C* +CO* + *	-1.18	0.75	-0.10	0.08	-0.05	0.05
15	CH_2CHCO*** + * -> CH_2CH*** + CO*	-0.89	0.69	-0.12	0.03	-0.07	0.01
16	CH_2CHCO*** + 2* -> $CHCHCO$**** + H*	-0.20	0.61	-0.01	-0.05	-0.01	-0.02
17	$CHCHCOOH$*** + 2* -> $CHCHCO$**** + OH*	0.65	1.09	0.02	0.04	0.05	0.06
18	$CHCHCO$**** -> $CHCH$*** + CO*	-0.82	0.51	-0.14	0.03	-0.08	0.01
19	CH_2CH*** + * -> $CHCH$*** + H*	-0.13	0.69	-0.03	-0.06	-0.02	-0.04
20	CH_2CH_2** + 2* -> CH_2CH*** + H*	-0.05	0.69	-0.05	-0.06	-0.02	-0.03

`

21	CH_2CH^{***} -> CH_2C^{**} + H*	-0.38	0.38	-0.01	-0.02	-0.01	-0.01
22	CH_3C^* + 2* -> CH_2C^{**} + H*	0.27	1.06	-0.02	-0.08	-0.02	-0.05
23	CH_3CH^{**} + 2* -> CH_2CH^{***} + H*	-0.29	0.51	-0.02	-0.11	0.00	-0.07
24	CH_3CH^{**} -> CH_3C^* + H*	-0.94	0.25	-0.01	-0.02	0.01	-0.02
25	$CH_3CH_2^*$ + 2* -> CH_3CH^{**} + H*	-0.10	0.66	-0.04	-0.06	0.01	-0.02
26	$CH_3CH_3^*$ + *-> $CH_3CH_2^*$ + H*	-0.11	0.64	-0.02	-0.06	0.00	0.00
27	$CH_3CH_2^*$ + 2* -> $CH_2CH_2^{**}$ + H*	-0.34	0.57	-0.02	-0.08	0.02	-0.03
28	$CH_3CH_2COOH^*$ + 2* -> $CH_3CH_2COO^{**}$ + H*	-0.41	0.31	0.08	-0.01	0.05	-0.02
29	$CH_3CH_2COO^{**}$ -> $CH_3CH_2^*$ + CO_2*	-0.09	1.49	0.02	0.01	0.02	0.03
30	$CH_3CH_2COO^{**}$ + 2* -> CH_3CHCOO^{***} + H*	0.47	1.24	-0.16	-0.23	-0.04	-0.08
31	$CH_3CHCOOH^{**}$ + 2* -> CH_3CHCOO^{***} + H*	0.27	0.75	-0.04	-0.08	-0.03	-0.06
32	$CH_3CHCOOH^{**}$ + 2* -> CH_3CH^{**} + $COOH^{**}$	-0.04	1.42	-0.08	-0.04	-0.05	-0.04
33	CH_3CHCOO^{***} -> CH_3CH^{**} + CO_2*	-0.66	0.95	0.13	0.17	0.07	0.09
34	CH_3CHCOO^{***} + * -> CH_3CCOO^{***} + H*	-0.22	1.04	-0.08	-0.02	-0.04	-0.02
35	CH_3CCOOH^{***} + * -> CH_3CCOO^{***} + H*	0.15	0.90	-0.12	-0.02	-0.04	0.02
36	CH_3CCOOH^{***} + * -> CH_3C^* + $COOH^{**}$	-0.89	1.06	-0.09	0.02	-0.01	0.04
37	$CH_2CHCOOH^{***}$ + 2*->CH_2CH^{***} + $COOH^{**}$	-0.04	1.86	-0.14	-0.05	-0.06	-0.02
38	CH_3CCOO^{***} -> CH_3C^* + CO_2* +*	-1.38	0.79	0.20	0.27	0.12	0.16
39	$COOH^{**}$ -> CO_2* + H*	-0.35	0.45	0.17	0.00	0.09	-0.01
40	$COOH^{**}$ -> CO* + OH*	-0.06	0.46	-0.02	0.07	-0.01	0.05
41	H_2O* + * -> OH* + H*	0.53	0.83	0.05	-0.01	0.04	0.00
42	CH_3CH_3 (g) + * -> CH_3CH_3*	0.57	N/A	-0.04	N/A	-0.05	N/A
43	CH_2CH_2 (g) + 2* -> CH_2CH_2**	-0.27	N/A	-0.07	N/A	-0.02	N/A
44	H_2O (g) + * -> H_2O*	0.52	N/A	-0.16	N/A	-0.08	N/A
45	CO_2 (g) + * -> CO_2*	0.54	N/A	-0.09	N/A	-0.08	N/A
46	CHCH (g) + 3* -> $CHCH^{***}$	-1.56	N/A	-0.14	N/A	-0.06	N/A
47	CO (g) + * -> CO*	-0.59	N/A	-0.19	N/A	-0.13	N/A
48	H_2 (g) + 2* -> H* + H*	-0.36	N/A	-0.01	N/A	0.00	N/A
49	CH_3CHCHO^{***} -> CH_3CHCO^{**} + H*	-0.92	0.08	0.04	0.05	0.01	0.02
50	CH_3CHCOH^{***} -> CH_3CHCO^{**} + H*	-0.26	0.60	-0.01	0.00	-0.02	-0.02
51	$CH_3CH_2CHO^*$ + 3* -> $CH_3CH_2CO^{***}$ + H*	-0.87	0.18	0.05	0.05	0.06	0.05
52	$CH_3CH_2COH^*$ + 3* -> $CH_3CH_2CO^{***}$ + H*	-0.25	0.04	0.00	0.02	0.02	0.01
53	$CH_3CH_2CHO^*$ + 3* -> CH_3CHCHO^{***} + H*	-0.24	0.69	-0.03	-0.07	0.03	0.00
54	$CH_3CHCH_2O^{***}$ + * -> CH_3CHCHO^{***} + H*	-0.67	-0.06	0.00	0.00	0.01	-0.01
55	$CH_3CHCHOH^{**}$ + 2* -> CH_3CHCHO^{***} + H*	0.15	0.50	-0.01	0.02	0.01	0.02
56	$CH_3CH_2COH^*$ + 3* -> CH_3CHCOH^{***} + H*	-0.28	1.07	-0.02	-0.15	0.01	-0.09
57	$CH_3CHCHOH^{**}$ + 2* -> CH_3CHCOH^{***} + H*	-0.51	0.45	0.05	0.03	0.03	0.01
58	$CH_3CH_2CH_2O^*$ + * -> $CH_3CH_2CHO^*$ + H*	-0.63	0.02	-0.04	0.04	-0.03	0.03
59	$CH_3CH_2CHOH^*$ + * -> $CH_3CH_2CHO^*$ + H*	0.14	0.69	-0.07	-0.03	-0.04	-0.01
60	$CH_3CH_2CHOH^*$ + * -> $CH_3CH_2COH^*$ + H*	-0.48	0.28	-0.03	0.00	0.00	0.01
61	$CH_3CH_2CH_2O^*$ + 3* -> $CH_3CHCH_2O^{***}$ + H*	-0.20	0.69	-0.07	-0.12	-0.02	-0.05
62	$CH_3CHCH_2OH^{**}$ + 2* ->$CH_3CHCH_2O^{***}$ + H*	0.24	0.58	0.03	0.03	0.04	0.03
63	$CH_3CH_2CHOH^*$ + 2* -> $CH_3CHCHOH^{**}$ + H*	-0.25	0.74	-0.09	-0.08	-0.02	-0.03
64	$CH_3CHCH_2OH^{**}$ + * -> $CH_3CHCHOH^{**}$ + H*	-0.58	0.51	0.04	-0.16	0.05	-0.10
65	$CH_3CH_2CH_2OH^*$ + * -> $CH_3CH_2CH_2O^*$ + H*	0.35	0.71	-0.07	-0.03	-0.02	-0.01
66	$CH_3CH_2CH_2OH^*$ + * -> $CH_3CH_2CHOH^*$ + H*	-0.41	0.46	-0.04	-0.08	-0.01	-0.04
67	$CH_3CH_2CH_2OH^*$ + 2* ->$CH_3CHCH_2OH^{**}$ + H*	-0.09	0.78	-0.17	-0.20	-0.08	-0.10
68	$CH_3CH_2CH_2OH$ (g) + * -> $CH_3CH_2CH_2OH$*	0.66	N/A	-0.07	N/A	-0.07	N/A
69	CH_3CH_2CHO (g) + * -> CH_3CH_2CHO*	0.70	N/A	-0.18	N/A	-0.13	N/A
70	$C_4H_8O_2$ (dioxane) + 2* -> $C_4H_8O_2$**	1.07	N/A	-0.08	N/A	-0.13	N/A

`

Table A.3: Surface coverages of various surface intermediates under both vapor phase and liquid phase conditions on a Pt (111) surface at a propionic acid partial pressure of 1 bar, CO partial pressure of 0.001 bar and a H_2 partial pressure of 0.1 bar, and at a temperature of 473 K, and the number of * signifies the number of adsorption sites.

species	gas	water (default)	water (+10%)	water (-10%)	dioxane (default)	dioxane (+10%)	dioxane (-10%)
CH_2C**	$7.57x10^{-12}$	$1.12x10^{-12}$	$4.17x10^{-13}$	$1.32x10^{-13}$	$4.62x10^{-12}$	$3.48x10^{-12}$	$2.85x10^{-12}$
CH_2CH***	$1.67x10^{-13}$	$4.50x10^{-15}$	$1.01x10^{-15}$	$3.96x10^{-16}$	$8.16x10^{-14}$	$6.10x10^{-14}$	$3.44x10^{-14}$
CH_2CH_2**	$1.95x10^{-13}$	$1.44x10^{-13}$	$5.82x10^{-14}$	$3.92x10^{-15}$	$1.26x10^{-12}$	$1.58x10^{-12}$	$2.14x10^{-13}$
CH_2CHCO***	$1.27x10^{-8}$	$5.67x10^{-10}$	$7.22x10^{-11}$	$1.13x10^{-10}$	$2.03x10^{-8}$	$1.23x10^{-8}$	$1.14x10^{-8}$
$CH_2CHCOOH$***	$4.51x10^{-9}$	$2.39x10^{-7}$	$2.12x10^{-7}$	$3.00x10^{-8}$	$3.60x10^{-7}$	$6.10x10^{-7}$	$1.36x10^{-7}$
CH_3C*	$2.74x10^{-5}$	$4.00x10^{-5}$	$2.63x10^{-5}$	$1.04x10^{-5}$	$7.17x10^{-5}$	$5.64x10^{-5}$	$4.37x10^{-5}$
CH_3CCO***	$9.48x10^{-12}$	$3.69x10^{-13}$	$3.50x10^{-14}$	$6.17x10^{-14}$	$7.34x10^{-12}$	$5.61x10^{-12}$	$7.02x10^{-12}$
CH_3CCOO***	$6.10x10^{-23}$	$4.68x10^{-24}$	$1.66x10^{-24}$	$3.33x10^{-24}$	$4.57x10^{-24}$	$7.21x10^{-24}$	$4.87x10^{-24}$
CH_3CCOOH***	$3.02x10^{-16}$	$2.49x10^{-15}$	$3.65x10^{-15}$	$2.10x10^{-16}$	$3.87x10^{-15}$	$9.46x10^{-15}$	$1.16x10^{-15}$
CH_3CH**	$6.35x10^{-13}$	$1.93x10^{-13}$	$5.45x10^{-14}$	$3.65x10^{-14}$	$1.40x10^{-12}$	$1.14x10^{-12}$	$1.03x10^{-12}$
CH_3CH_2*	$2.29x10^{-13}$	$6.35x10^{-14}$	$4.13x10^{-14}$	$2.37x10^{-14}$	$5.01x10^{-13}$	$4.51x10^{-13}$	$6.66x10^{-13}$
$CH_3CH_2CH_2O$*	$2.86x10^{-30}$	$2.41x10^{-28}$	$1.39x10^{-28}$	$7.81x10^{-29}$	$1.20x10^{-27}$	$1.48x10^{-27}$	$1.00x10^{-27}$
$CH_3CH_2CH_2OH$*	$6.11x10^{-19}$	$3.97x10^{-15}$	$3.27x10^{-15}$	$3.78x10^{-16}$	$3.18x10^{-14}$	$4.87x10^{-14}$	$1.24x10^{-14}$
CH_3CH_2CHO*	$1.32x10^{-20}$	$1.36x10^{-16}$	$1.20x10^{-16}$	$2.26x10^{-17}$	$3.15x10^{-16}$	$5.44x10^{-16}$	$2.02x10^{-16}$
CH_3CH_2CHOH*	$2.46x10^{-13}$	$1.82x10^{-12}$	$6.38x10^{-13}$	$3.35x10^{-13}$	$1.17x10^{-11}$	$9.36x10^{-12}$	$7.09x10^{-12}$
CH_3CH_2CO***	$4.61x10^{-12}$	$2.75x10^{-14}$	$3.39x10^{-15}$	$3.55x10^{-15}$	$2.68x10^{-12}$	$1.97x10^{-12}$	$1.13x10^{-12}$
CH_3CH_2COH*	$6.80x10^{-9}$	$1.69x10^{-8}$	$7.88x10^{-9}$	$5.46x10^{-9}$	$1.48x10^{-7}$	$1.44x10^{-7}$	$9.80x10^{-8}$
CH_3CH_2COO**	$9.88x10^{-7}$	$1.39x10^{-5}$	$8.10x10^{-6}$	$8.07x10^{-6}$	$5.15x10^{-5}$	$3.63x10^{-5}$	$5.84x10^{-5}$
CH_3CH_2COOH*	$2.72x10^{-5}$	$4.01x10^{-1}$	$4.53x10^{-1}$	$4.09x10^{-1}$	$1.64x10^{-1}$	$2.18x10^{-1}$	$2.24x10^{-1}$
CH_3CH_3*	$4.83x10^{-21}$	$9.35x10^{-21}$	$5.58x10^{-21}$	$1.37x10^{-21}$	$1.40x10^{-19}$	$1.34x10^{-19}$	$6.90x10^{-20}$
CH_3CHCH_2O***	$1.56x10^{-25}$	$2.77x10^{-26}$	$4.32x10^{-27}$	$4.36x10^{-27}$	$3.86x10^{-25}$	$2.51x10^{-25}$	$2.22x10^{-25}$
CH_3CHCH_2OH**	$3.08x10^{-20}$	$5.06x10^{-18}$	$3.24x10^{-18}$	$5.40x10^{-19}$	$7.05x10^{-18}$	$1.29x10^{-17}$	$3.50x10^{-18}$
CH_3CHCHO***	$1.11x10^{-19}$	$5.80x10^{-20}$	$8.63x10^{-21}$	$9.83x10^{-21}$	$5.27x10^{-19}$	$3.79x10^{-19}$	$3.45x10^{-19}$
$CH_3CHCHOH$**	$8.00x10^{-15}$	$4.92x10^{-14}$	$2.33x10^{-14}$	$1.03x10^{-14}$	$2.35x10^{-13}$	$2.64x10^{-13}$	$1.24x10^{-13}$
CH_3CHCO**	$7.29x10^{-10}$	$6.44x10^{-10}$	$1.92x10^{-10}$	$1.58x10^{-10}$	$4.49x10^{-9}$	$3.53x10^{-9}$	$3.82x10^{-9}$
CH_3CHCOH***	$4.96x10^{-13}$	$8.79x10^{-14}$	$1.89x10^{-14}$	$1.11x10^{-14}$	$1.50x10^{-12}$	$1.43x10^{-12}$	$8.38x10^{-13}$
CH_3CHCOO***	$5.76x10^{-20}$	$6.07x10^{-20}$	$3.26x10^{-20}$	$2.63x10^{-20}$	$1.05x10^{-19}$	$1.01x10^{-19}$	$7.35x10^{-20}$
$CH_3CHCOOH$**	$2.93x10^{-12}$	$2.20x10^{-09}$	$2.26x10^{-09}$	$5.66x10^{-10}$	$5.16x10^{-10}$	$9.89x10^{-10}$	$2.28x10^{-10}$
CHCH***	$6.89x10^{-13}$	$1.38x10^{-14}$	$1.84x10^{-15}$	$1.04x10^{-15}$	$1.95x10^{-13}$	$1.18x10^{-13}$	$1.18x10^{-13}$
CHCHCO****	$7.20x10^{-15}$	$1.30x10^{-16}$	$1.42x10^{-17}$	$7.17x10^{-18}$	$3.84x10^{-15}$	$2.77x10^{-15}$	$1.80x10^{-15}$
CHCHCOOH***	$1.64x10^{-13}$	$4.71x10^{-12}$	$5.17x10^{-12}$	$6.10x10^{-13}$	$4.80x10^{-12}$	$9.23x10^{-12}$	$2.09x10^{-12}$
CO*	$3.21x10^{-1}$	$4.93x10^{-1}$	$4.83x10^{-1}$	$5.27x10^{-1}$	$4.72x10^{-1}$	$4.65x10^{-1}$	$5.01x10^{-1}$
CO_2*	$9.84x10^{-23}$	$1.04x10^{-20}$	$9.63x10^{-21}$	$3.45x10^{-21}$	$2.62x10^{-20}$	$2.90x10^{-20}$	$1.98x10^{-20}$
COOH**	$9.28x10^{-18}$	$2.52x10^{-17}$	$2.55x10^{-17}$	$1.04x10^{-18}$	$1.96x10^{-16}$	$3.89x10^{-16}$	$5.91x10^{-17}$
H*	$2.55x10^{-1}$	$3.71x10^{-2}$	$2.61x10^{-2}$	$2.34x10^{-2}$	$1.10x10^{-1}$	$1.04x10^{-1}$	$8.21x10^{-2}$
H_2O*	$3.21x10^{-18}$	$1.67x10^{-15}$	$1.05x10^{-15}$	$5.24x10^{-16}$	$5.97x10^{-15}$	$9.33x10^{-15}$	$3.49x10^{-15}$
$C_4H_8O_2$**	$1.71x10^{-9}$	$5.55x10^{-6}$	$5.36x10^{-6}$	$1.98x10^{-8}$	$5.50x10^{-6}$	$7.33x10^{-6}$	$6.61x10^{-7}$
OH*	$6.49x10^{-19}$	$7.04x10^{-19}$	$4.04x10^{-19}$	$8.18x10^{-20}$	$6.04x10^{-18}$	$7.12x10^{-18}$	$2.59x10^{-18}$
*	$4.24x10^{-1}$	$6.85x10^{-2}$	$3.75x10^{-2}$	$4.13x10^{-2}$	$2.54x10^{-1}$	$2.13x10^{-1}$	$1.92x10^{-1}$

`

Table A.4: CO and H lateral interaction coefficients, α_{CO} and α_H, of various species on Pt (111) calculated at a temperature of 473 K.

Species	α_{CO}	α_H
CH_2C**	0.873	0.749
CH_2CH***	0.614	0.574
CH_2CH_2**	0.101	0.327
CH_2CHCO***	0.010	-0.348
$CH_2CHCOOH$***	-0.022	0.498
CH_3C*	0.453	0.603
CH_3CCO***	1.155	0.674
CH_3CCOO***	2.022	0.703
CH_3CCOOH***	1.107	0.969
CH_3CH**	0.185	0.447
CH_3CH_2*	0.024	0.278
$CH_3CH_2CH_2O$*	0.356	0.521
$CH_3CH_2CH_2OH$*	-0.938	-0.031
CH_3CH_2CHO*	-0.682	0.208
CH_3CH_2CHOH*	-0.015	0.471
CH_3CH_2CO***	0.736	0.591
CH_3CH_2COH*	-0.058	0.250
CH_3CH_2COO**	-0.263	0.255
CH_3CH_2COOH*	-1.207	-0.027
CH_3CH_3*	-0.222	0.059
CH_3CHCH_2O***	0.795	0.481
CH_3CHCH_2OH**	0.312	0.529
CH_3CHCHO***	0.653	0.590
$CH_3CHCHOH$**	0.366	0.422
CH_3CHCO**	0.495	0.398
CH_3CHCOH***	0.715	0.642
CH_3CHCOO***	1.190	0.794
$CH_3CHCOOH$**	0.295	0.803
CHCH***	0.736	0.576
CHCHCO****	1.124	0.661
CHCHCOOH***	0.802	0.827
CO*	0.734	0.328
CO_2*	-0.164	0.035
COOH**	0.143	0.279
H*	0.300	0.234
H_2O*	-0.553	-0.048
OH*	0.539	0.389
$C_4H_8O_2$**(dioxane)	-0.832	0.168

`

Table A.5: Degrees of selectivity control for various key species that have impact on the DCX mechanism under gas and liquid phase conditions at a temperature of 473 K, a propionic acid partial pressure of 1 bar, a CO partial pressure of 0.001 bar and a hydrogen partial pressure of 0.1 bar, and the tesults from solvation calculations with ±10% of the default COMSO Pt cavity radius are also shown for water and 1,4-dioxane, and N/A denotes that the value is smaller than 0.01.

species	Gas	Water (default)	Water (+10%)	Water (-10%)	Dioxane (default)	Dioxane (+10%)	Dioxane (-10%)
H*	1.57	-0.15	-0.11	-0.09	0.16	N/A	-0.07
CH_3CH_2COO**	0.97	0.96	0.96	0.96	0.98	0.96	0.96
CH_3CH_2COOH*	-0.96	0.07	0.21	0.16	-0.61	-0.49	-0.44
CO*	-1.22	2.18	2.25	2.31	1.84	1.88	2.02

Table A.6: Degrees of selectivity control for various key species that have impact on the DCN mechanism under gas and liquid phase conditions at a temperature of 473 K, a propionic acid partial pressure of 1 bar, a CO partial pressure of 0.001 bar and a hydrogen partial pressure of 0.1 bar. Results from solvation calculations with ±10% of default COMSO Pt cavity radius are also shown for water and 1,4-dioxane, and N/A denotes that the value is smaller than 0.01.

species	Gas	Water (default)	Water (+10%)	Water (-10%)	Dioxane (default)	Dioxane (+10%)	Dioxane (-10%)
H*	1.30	0.09	-0.05	0.03	0.55	0.44	0.35
CH_3CH_2CO***	0.49	0.45	0.21	0.20	0.75	0.76	0.66
CH_3CHCO**	0.02	0.32	0.29	0.46	0.11	0.11	0.19
CH_3CH_2COOH*	N/A	0.40	0.43	0.45	-0.04	0.01	0.05
$CH_3CHCOOH$**	N/A	0.10	0.44	0.23	0.02	0.02	0.02
CH_3CH_2CHOH*	-0.13	-0.22	-0.13	-0.23	-0.24	-0.26	-0.28
$CH_3CH_2CH_2OH$*	-0.18	-0.62	-0.39	-0.50	-0.66	-0.64	-0.64
CH_3CH_2CHO*	-0.22	N/A	N/A	N/A	-0.03	-0.02	-0.02
CO*	-2.02	-0.20	0.46	0.14	-0.42	-0.50	-0.42

Table A.7: Degrees of selectivity control for various key species that have impact on the propanol production path under gas and liquid phase conditions at a temperature of 473 K, a propionic acid partial pressure of 1 bar, a CO partial pressure of 0.001 bar and a hydrogen partial pressure of 0.1 bar and the results from solvation calculations with ±10% of default COMSO Pt cavity radius are also shown for water and 1,4-dioxane, and N/A denotes that the value is smaller than 0.01 with the values in front of the brackets and the values in the brackets corresponding to the degrees of selectivity control for the propanol and the propionaldehyde production path, respectively.

species	Gas	Water (default)	Water (+10%)	Water (-10%)	Dioxane (default)	Dioxane (+10%)	Dioxane (-10%)
H*	0.81	N/A	N/A	0.01	0.22	0.14	0.09
CO*	-0.61	0.88	0.93	0.99	0.95	0.81	0.90
CH_3CH_2CO***	-0.41	-0.01	N/A	N/A	-0.02	-0.02	-0.01
CH_3CH_2CHO*	-0.23	N/A	N/A	N/A	-0.03	-0.02	-0.02

`

CH_3CH_2COOH*	N/A	0.39	0.51	0.48	-0.05	N/A	0.02
CH_3CH_2CHOH*	-0.13	-0.24	-0.22	-0.29	-0.23	-0.25	-0.28
$CH_3CH_2CH_2OH$*	0.79	0.25	0.23	0.30	0.28	0.30	0.31

Table A.8: Degrees of selectivity control for various key species that have impact on the propionaldehyde production path under gas and liquid phase conditions at a temperature of 473 K, a propionic acid partial pressure of 1 bar, a CO partial pressure of 0.001 bar and a hydrogen partial pressure of 0.1 bar, and the results from solvation calculations with ±10% of default COMSO Pt cavity radius are also shown for water and 1,4-dioxane, and N/A denotes that the value is smaller than 0.01 while the values in front of the brackets and the values in the brackets corresponding to the degrees of selectivity control for the propanol and the propionaldehyde production path, respectively.

species	Gas	Water (default)	Water (+10%)	Water (-10%)	Dioxane (default)	Dioxane (+10%)	Dioxane (-10%)
H*	0.62	-0.08	-0.05	-0.04	0.1	0.01	-0.04
CO*	-1.02	0.86	0.91	0.97	0.82	0.73	0.84
CH_3CH_2CO***	-0.41	-0.01	N/A	N/A	-0.02	-0.02	-0.01
CH_3CH_2CHO*	0.39	0.01	N/A	N/A	0.08	0.06	0.04
CH_3CH_2COOH*	N/A	0.46	0.58	0.54	-0.03	0.04	0.07
CH_3CH_2CHOH*	0.22	0.72	0.74	0.67	0.62	0.63	0.63
$CH_3CH_2CH_2OH$*	-0.18	-0.71	-0.73	-0.67	-0.68	-0.67	-0.66

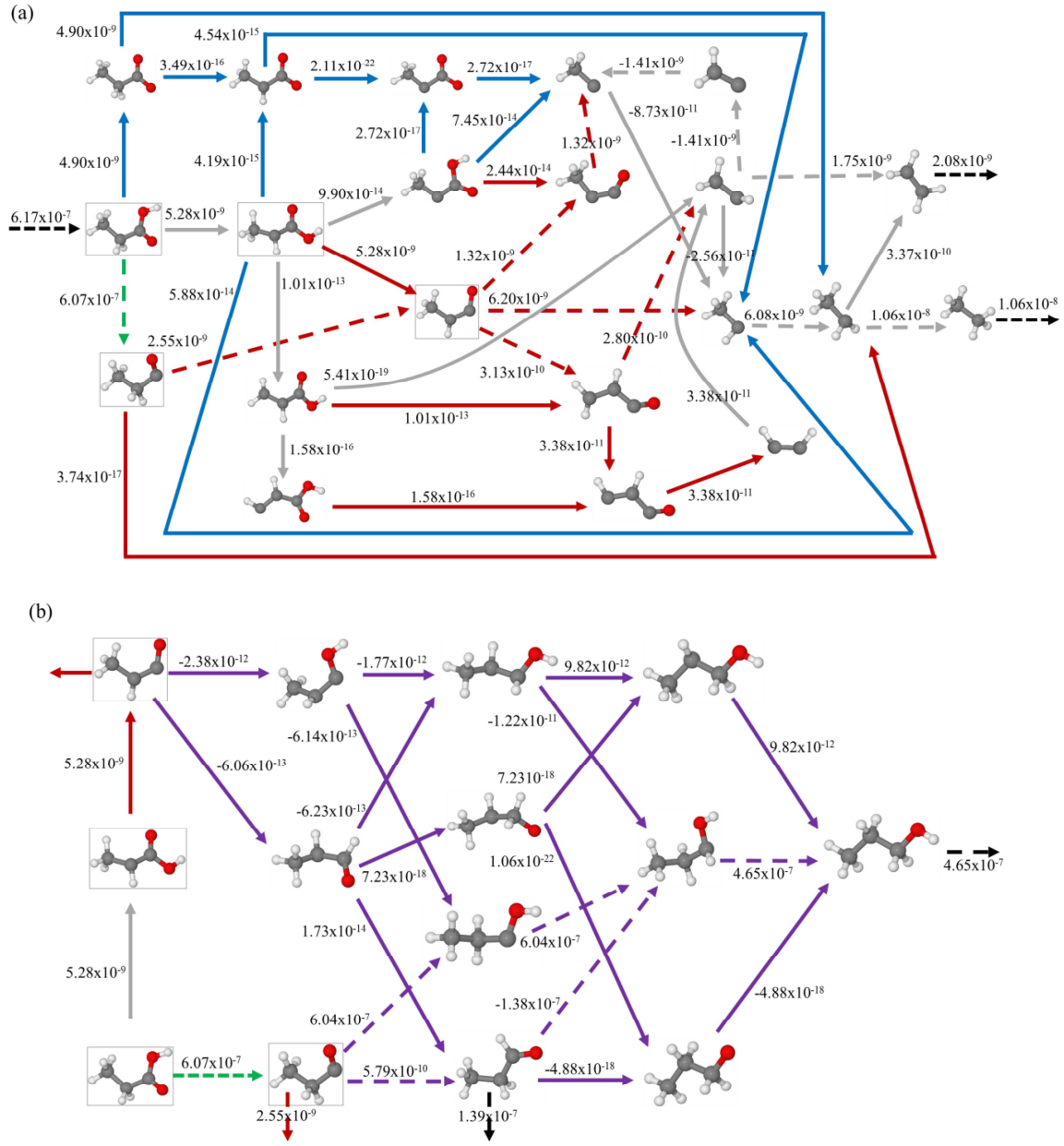

Figure A.1: TOFs (s^{-1}) of various elementary steps in the presence of liquid water (with 10% increase in the default COSMO Pt cavity radius in the solvation calculations) at a temperature of 473 K, a propionic acid gas phase partial pressure of 1 bar, a CO gas phase partial pressure of 0.001 bar and a hydrogen partial pressure of 0.1 bar. For convenience, black arrows are the adsorption/desorption steps, blue arrows are DCX steps, red arrows are DCN steps, purple steps are steps involved in propanol and propionaldehyde productions, while gray arrows are the steps involved in both DCN and DCX steps and green arrows are steps involved in DCN and propanol and propionaldehyde productions. Dominant pathways are shown in dashed arrows. TOFs (s^{-1}) of reaction steps involved in DCX and DCN are shown in (a) while the TOFs (s^{-1}) for propanol and propionaldehyde production steps are shown in (b).

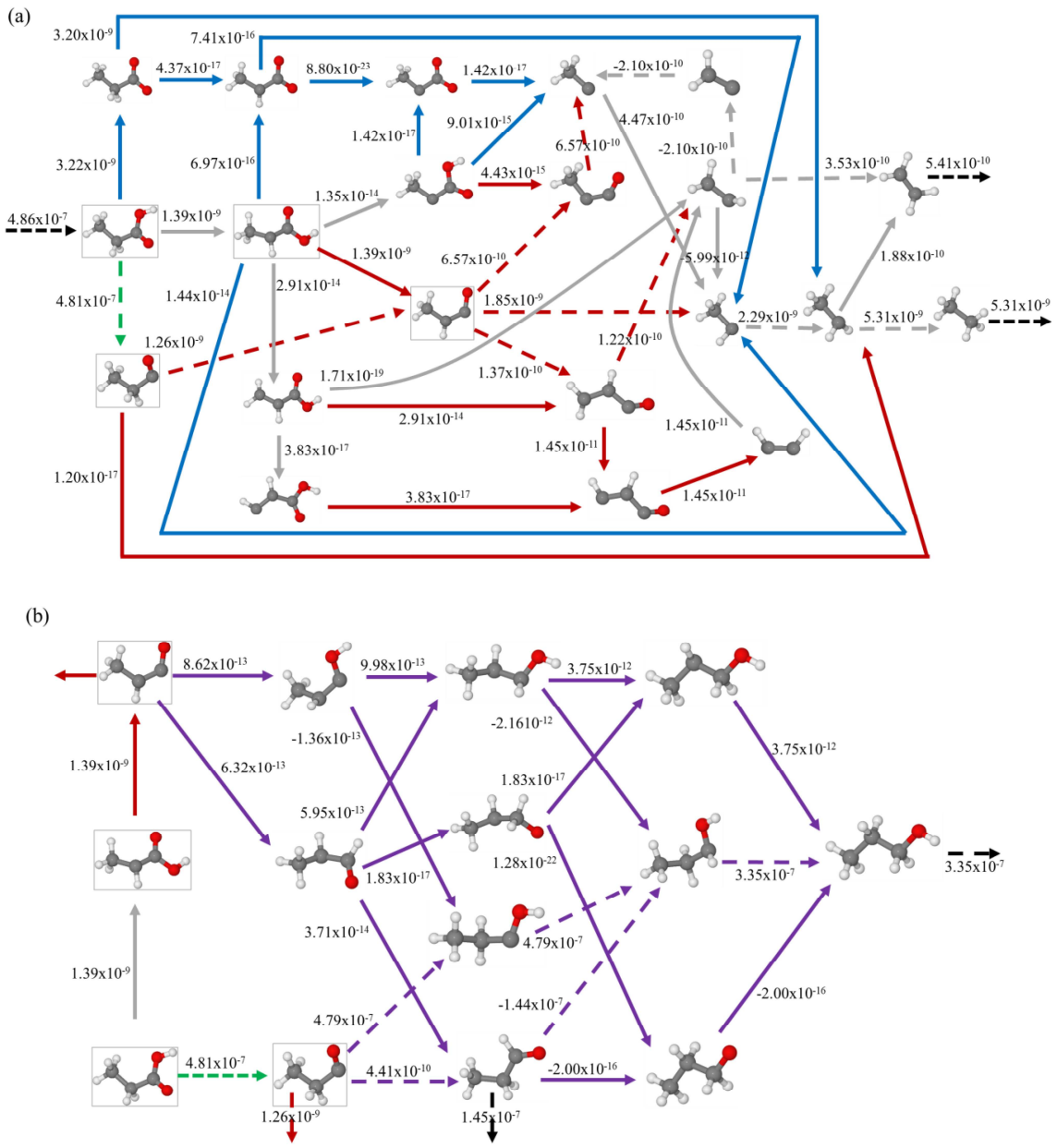

Figure A.2: TOFs (s^{-1}) of various elementary steps in the presence of liquid water (with 10% decrease in the default COSMO Pt cavity radius in the solvation calculations) at a temperature of 473 K, a propionic acid gas phase partial pressure of 1 bar, a CO gas phase partial pressure of 0.001 bar and a hydrogen partial pressure of 0.1 bar. For convenience, black arrows are the adsorption/desorption steps, blue arrows are DCX steps, red arrows are DCN steps, purple steps are steps involved in propanol and propionaldehyde productions, while gray arrows are the steps involved in both DN and DCX steps and green arrows are steps involved in DCN and propanol and propionaldehyde productions. Dominant pathways are shown in dashed arrows. TOFs (s^{-1}) of reaction steps involved in DCX and DCN are shown in (a) while the TOFs (s^{-1}) for propanol and propionaldehyde production steps are shown in (b).

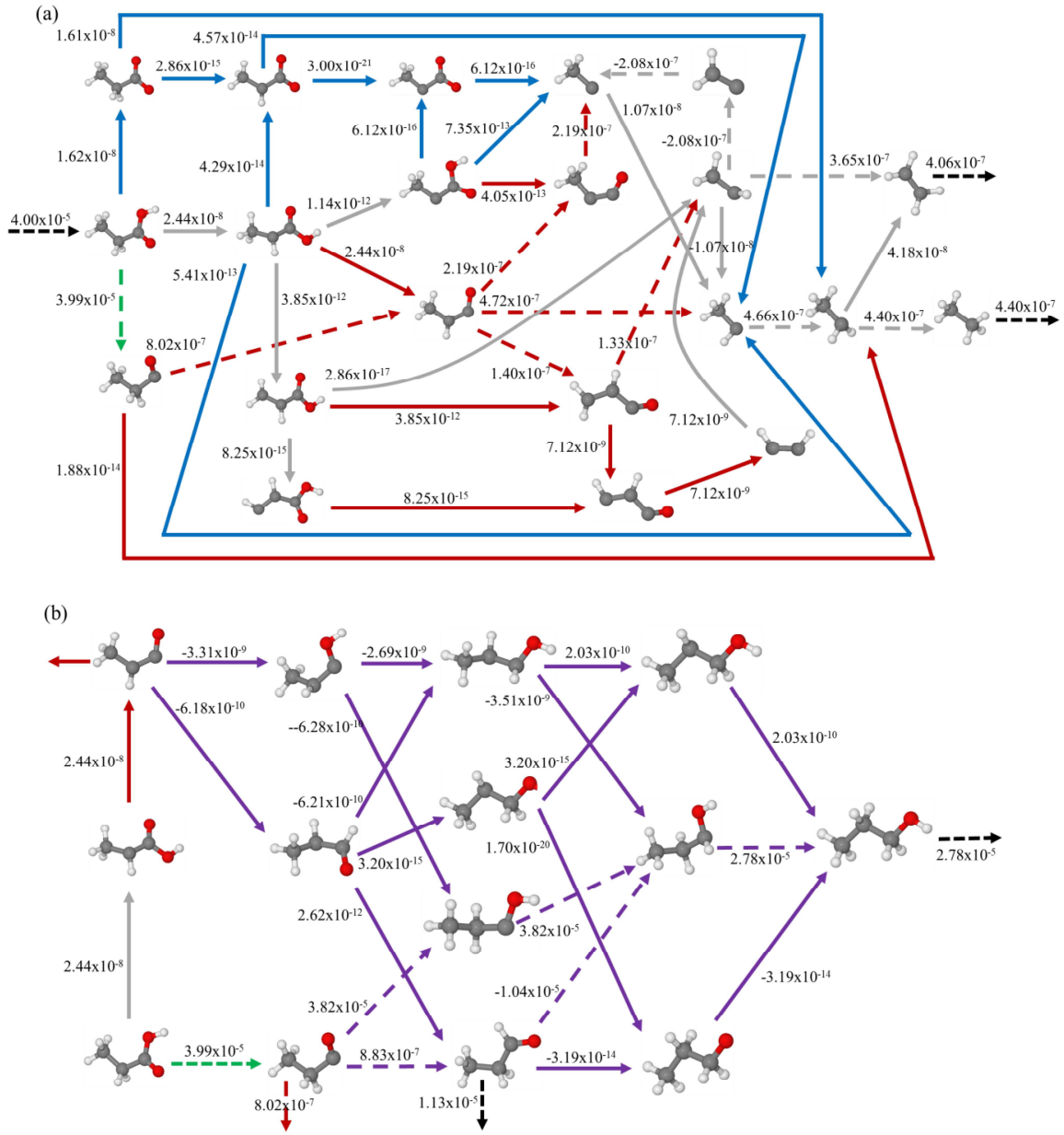

Figure A.3: TOFs (s^{-1}) of various elementary steps in the presence of liquid 1,4-dioxane (with 10% increase of the default COSMO Pt cavity radius in the solvation calculations) at a temperature of 473 K, a propionic acid gas phase partial pressure of 1 bar, a CO gas phase partial pressure of 0.001 bar and a hydrogen partial pressure of 0.1 bar. For convenience, black arrows are the adsorption/desorption steps, blue arrows are DCX steps, red arrows are DCN steps, purple steps are steps involved in propanol and propionaldehyde productions, while gray arrows are the steps involved in both DCN and DCX steps and green arrows are steps involved in DCN and propanol and propionaldehyde productions. Dominant pathways are shown in dashed arrows. TOFs (s^{-1}) of reaction steps involved in DCX and DCN are shown in (a) while the TOFs (s^{-1}) for propanol and propionaldehyde production steps are shown in (b).

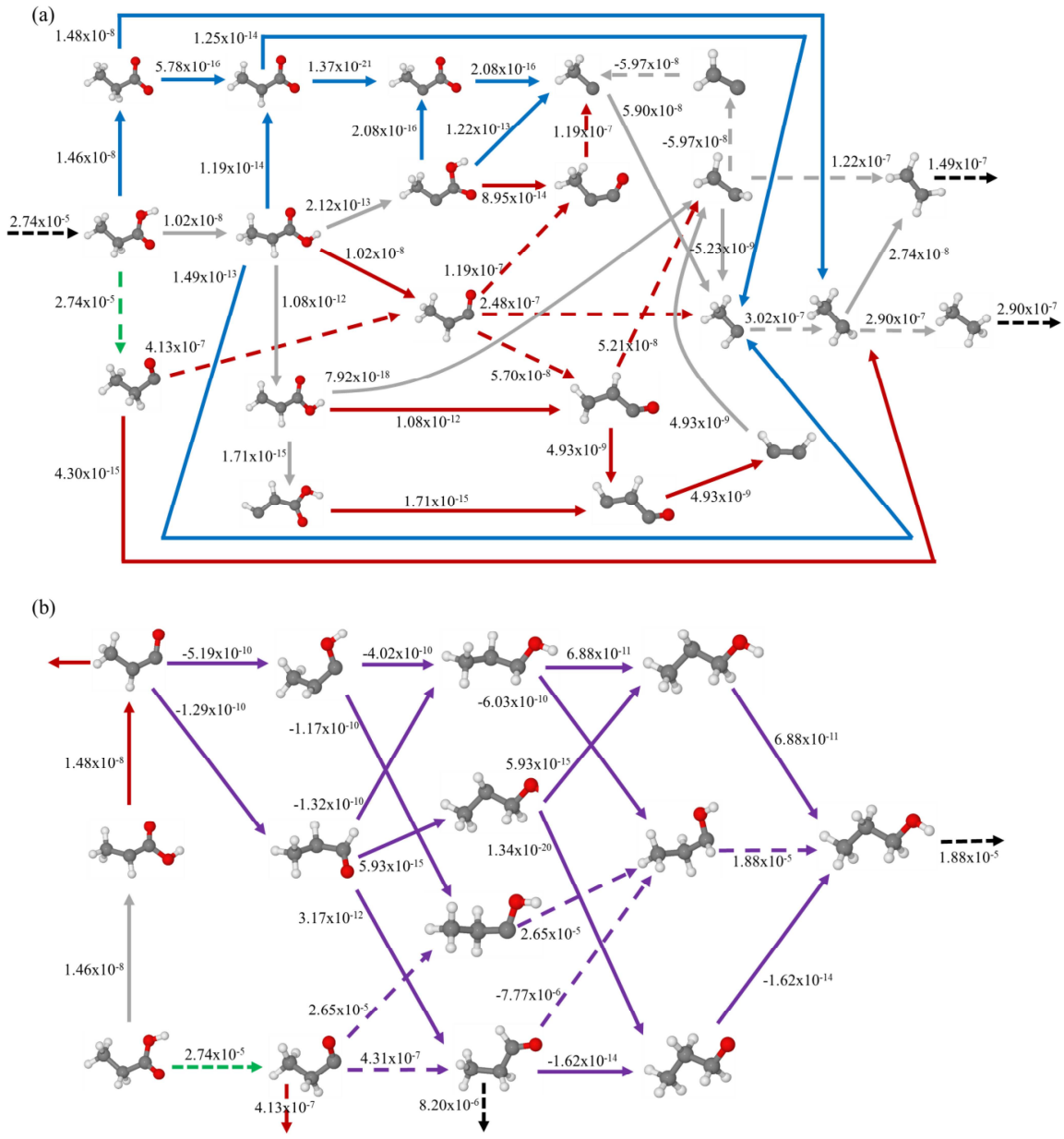

Figure A.4: TOFs (s^{-1}) of various elementary steps in the presence of liquid 1,4-dioxane (with 10% decrease in the default COSMO Pt cavity radius in the solvation calculations) at a temperature of 473 K, a propionic acid gas phase partial pressure of 1 bar, a CO gas phase partial pressure of 0.001 bar and a hydrogen partial pressure of 0.1 bar. For convenience, black arrows are the adsorption/desorption steps, blue arrows are DCX steps, red arrows are DCN steps, purple steps are steps involved in propanol and propionaldehyde productions, while gray arrows are the steps involved in both DCN and DCX steps and green arrows are steps involved in DCN and propanol and propionaldehyde productions. Dominant pathways are shown in dashed arrows. TOFs (s^{-1}) of reaction steps involved in DCX and DCN are shown in (a) while the TOFs (s^{-1}) for propanol and propionaldehyde production steps are shown in (b).

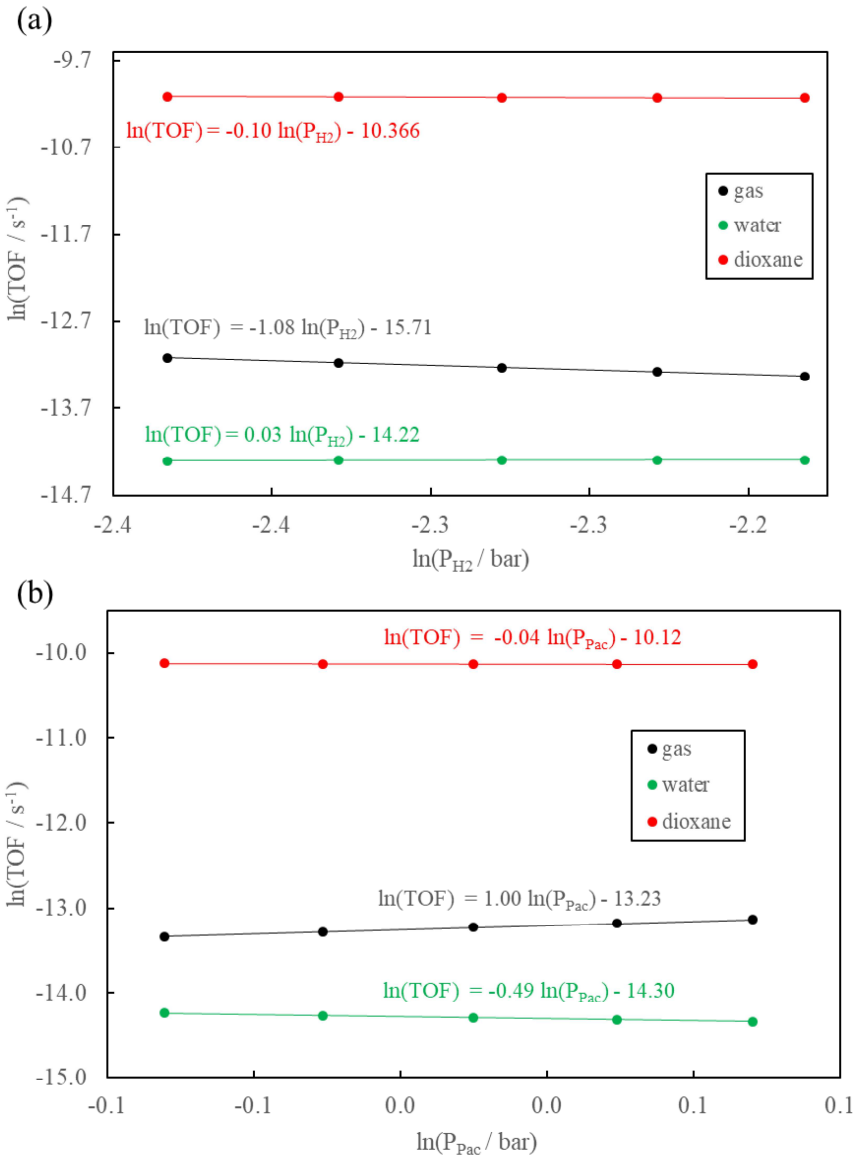

Figure A.5: Reaction orders of (a) H_2 and (b) propionic acid at a temperature of 473 K, a propionic acid gas phase partial pressure of 1 bar, a CO gas phase partial pressure of 0.001 bar and a hydrogen partial pressure of 0.1 bar with a 10% increase in the default COMSO Pt cavity radius in the solvation calculations.

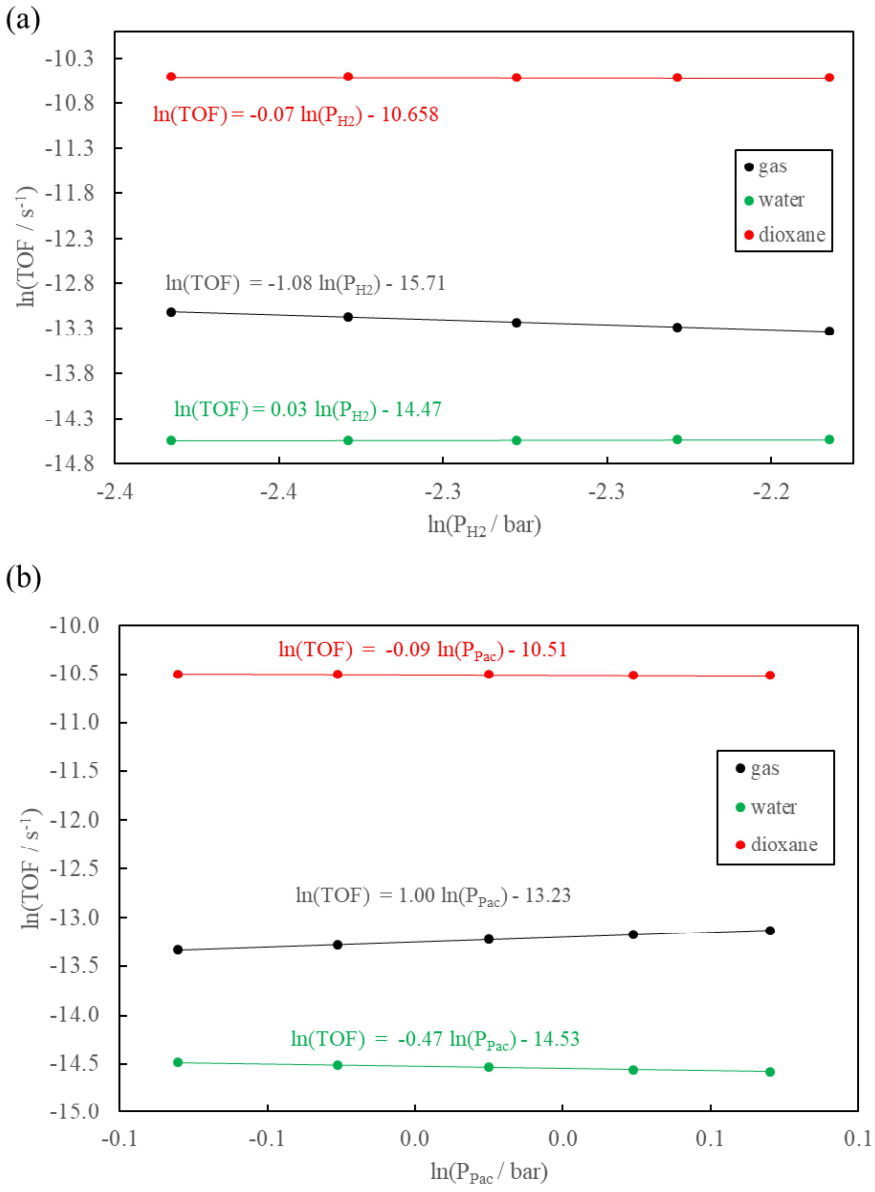

Figure A.6: Reaction orders of (a) H_2 and (b) propionic acid at a temperature of 473 K, a propionic acid gas phase partial pressure of 1 bar, a CO gas phase partial pressure of 0.001 bar and a hydrogen partial pressure of 0.1 bar with 10% decrease in the default COMSO Pt cavity radius in the solvation calculations.

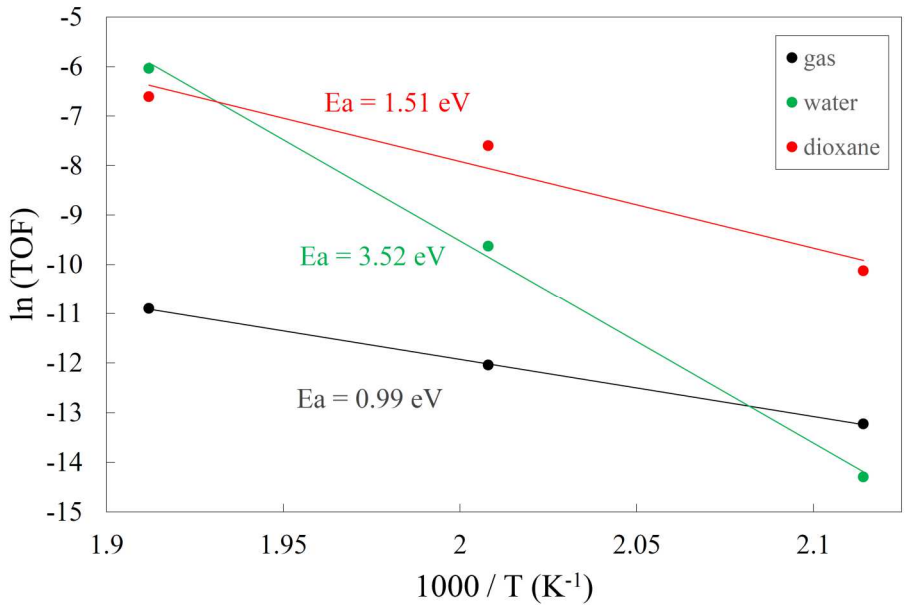

Figure A.7: Arrhenius plot for the HDO of propionic acid in the temperature range 473−523 K with a propionic acid gas phase partial pressure of 1 bar, a CO gas phase partial pressure of 0.001 bar and a hydrogen partial pressure of 0.1 bar, with 10% increase in the default COMSO Pt cavity radius in the solvation calculations.

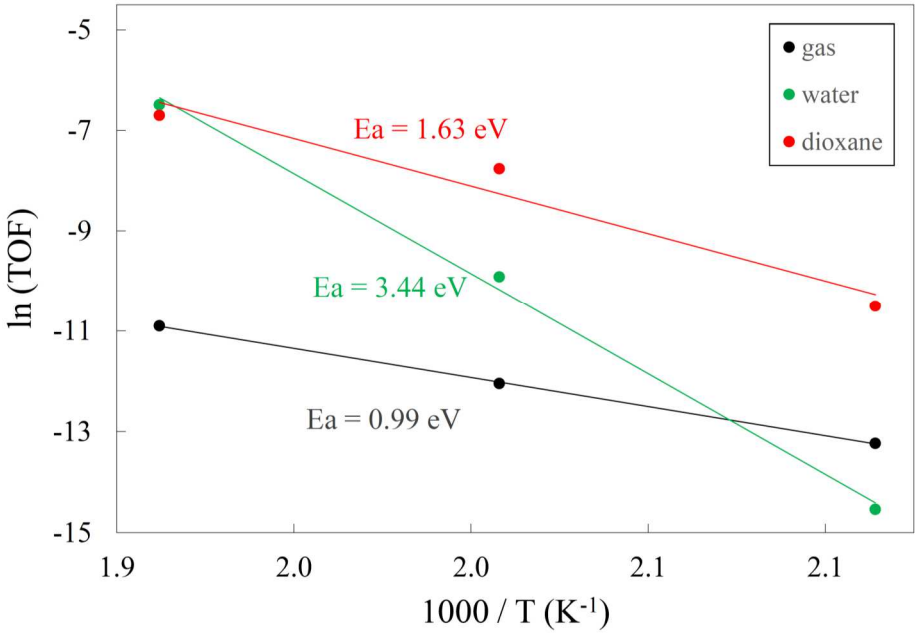

Figure A.8: Arrhenius plot for the HDO of propionic acid in the temperature range 473−523 K with a propionic acid gas phase partial pressure of 1 bar, a CO gas phase partial pressure of 0.001 bar and a hydrogen partial pressure of 0.1 bar, with 10% decrease in the default COMSO Pt cavity radius in the solvation calculations.

(a)

Number of atoms				
layers \ size	2 rings	3 rings	4 rings	5 rings
1	14	30	52	80
2	22	51	92	N/A
3	30	72	132	N/A
4	44	102	184	N/A

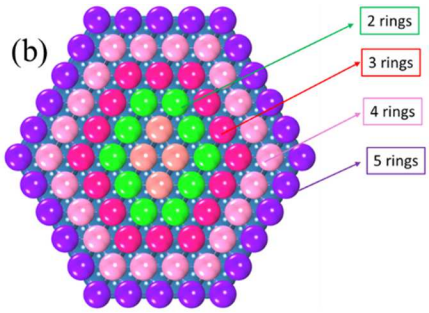

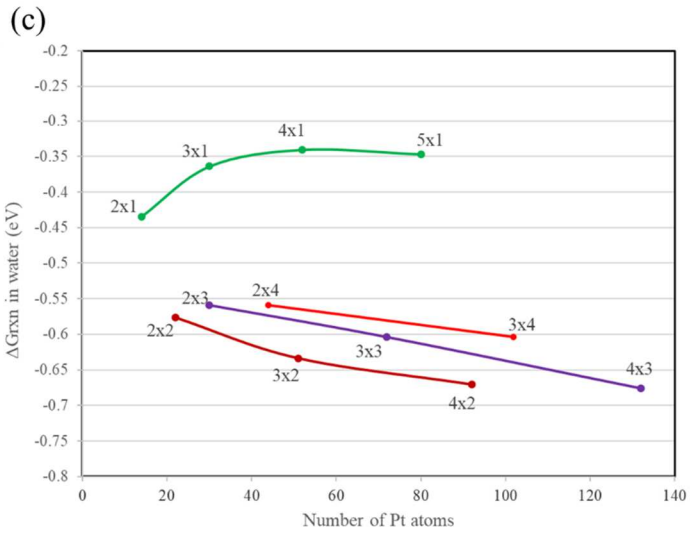

Figure A.9: CO adsorption in liquid water on a Pt (111) surface with different cluster sizes used in the solvent calculations. We built a ring-like cluster model that is used in the iSMS calculations, and we used MxN to represent our model with M and N corresponding to the number of rings in each layer and the number of metal atoms layers, respectively. For instance, 3x2 denotes a cluster model containing 3 rings and 2 metal atom layers. (a) list the total number of metal atoms of various clusters with different cluster size and layers. (b) displays the shape of different ring like clusters and (c) plot the reaction energies of CO adsorption versus metal atom numbers of the corresponding cluster. For 5 rings cluster, only 1 metal atom layer cluster model calculations were conducted since the computational cost for larger models increases dramatically. Since the 4x1 and 5x1 model lead to essentially equivalent adsorption free energies, we used a 4-ring model. Also, since the 4x2 and 4x3 cluster model lead to essentially equivalent adsorption free energies in liquid water, we used a 2-layer thick cluster model for all calculations.

`

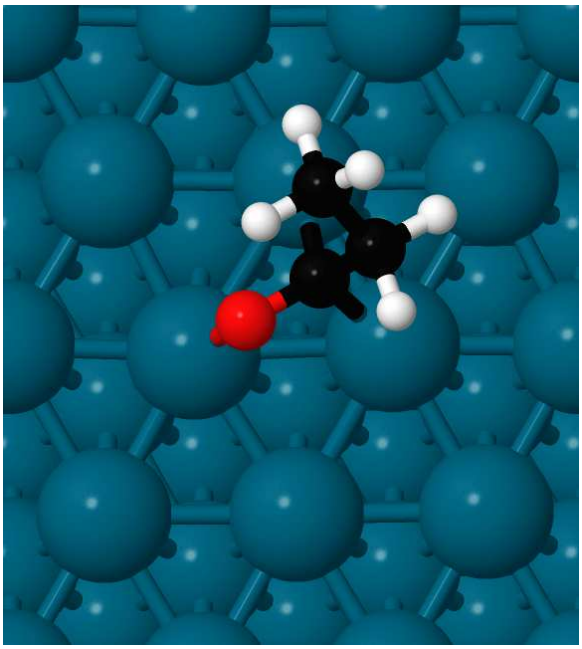

Figure A.10: Optimized $CH_3CH_2CO^{***}$ adsorption structure on Pt (111) used to illustrate how the number of occupied sites by a surface intermediate has been determined. The total number of active sites of the surface was defined to be the total number of Pt atoms on the surface. The number of occupied sites by a surface intermediate is estimated to be the number of Pt atoms that form strong bonds with the adsorbed species. For instance, for $CH_3CH_2CO^{***}$, the oxygen atom forms a strong bond with one Pt atom while one carbon atom interacts strongly with two Pt atoms. Thus, $CH_3CH_2CO^{***}$ occupies three sites on the surface.

`

APPENDIX B

SUPPORTING INFORMATION FOR INVESTIGATE THE REACTION MECHANISMS OF THE HYDRODEOXYGENATION OF PROPIONIC ACID ON RH (111) SURFACE: A FIRST PRINCIPLES STUDY [5]

[5] W. Yang, R.V. Solomon, J. Lu, O. Mamun, J.Q. Bond and A. Heyden. To be submitted to Journal of Catalysis,

`

Table B.1: Lateral interaction coefficient (α) of various surface species that were calculated with three H and CO molecules on the surface, respectively.

Species	α_H	α_{CO}
CH_2C***	0.213	-0.035
CH_2CH***	0.087	-0.027
CH_2CH_2**	0.080	-0.785
CH_2CHCO****	1.279	1.174
$CH_2CHCOOH$****	-0.251	-1.105
CH_3C***	0.107	-0.300
CH_3CCO****	0.304	0.326
CH_3CCOO***	0.718	0.553
CH_3CCOOH***	0.296	-0.838
CH_3CH***	0.104	-0.363
CH_3CH_2**	0.118	-0.317
$CH_3CH_2CH_2O$*	0.212	-0.629
$CH_3CH_2CH_2OH$*	-0.121	-1.655
$CH_3CH_2CH_3$*	0.025	-0.595
CH_3CH_2CHO*	0.183	-0.152
CH_3CH_2CHOH*	-0.025	-0.958
CH_3CH_2CO***	0.085	-0.332
CH_3CH_2COH*	-0.004	-0.492
CH_3CH_2COO**	0.062	-0.426
CH_3CH_2COOH*	-0.116	-1.122
CH_3CH_3*	0.070	-0.236
CH_3CHCH_2O***	0.365	0.606
CH_3CHCH_2OH**	0.187	-0.408
CH_3CHCHO***	0.260	0.583
$CH_3CHCHOH$**	0.461	-0.194
CH_3CHCO**	1.027	1.056
CH_3CHCOH***	0.136	-0.276
CH_3CHCOO***	0.385	1.101
$CH_3CHCOOH$**	0.334	-0.200
CHCH****	0.229	-0.198
CHCHCO****	0.389	0.460
CHCHCOOH****	0.727	-0.648
CO***	0.168	0.521
CO_2*	0.209	0.577
COOH**	-0.008	-0.306
H*	0.065	0.113
H_2O*	-0.011	-0.893
O*	0.276	0.493
$OCH_2CH_2OCH_2CH_2$**	-0.098	-1.533
OH*	0.132	-0.177

`

Table B.2: TOFs (s^{-1}) and surface coverage of the most abundant surface intermediates (divided by the corresponding number of sites occupied of the adsorption on the surface) during the HDO of Pac on Rh (111) surface at a temperature of 473 K under both vapor phase and liquid phase where water and 1, 4-dioanxe were used as the solvent, respectively, and the results from solvent calculations with ±10% of the default COSMO Rh cavity are also shown in the table, and 1 site was used for the adsorption of CO on the Rh (111) surface in the microkinetic model.

species	**gas phase**	**water (-10%)**	**water (d)**	**water (+10%)**	**dioxane (-10%)**	**dioxane (d)**	**dioxane (+10%)**
free site	5.17×10^{-4}	1.46×10^{-4}	3.16×10^{-5}	1.21×10^{-5}	2.78×10^{-4}	6.91×10^{-5}	4.21×10^{-5}
H*	8.08×10^{-3}	1.61×10^{-3}	2.81×10^{-4}	1.22×10^{-4}	4.92×10^{-3}	8.83×10^{-4}	4.97×10^{-4}
CO*	6.40×10^{-1}	6.89×10^{-1}	7.11×10^{-1}	7.08×10^{-1}	6.19×10^{-1}	6.63×10^{-1}	6.80×10^{-1}
CH_3C*	6.79×10^{-2}	9.99×10^{-2}	1.09×10^{-1}	1.11×10^{-1}	6.57×10^{-2}	8.86×10^{-2}	9.98×10^{-2}
CH_3CH_2COOH*	2.83×10^{-1}	2.09×10^{-1}	1.80×10^{-1}	1.81×10^{-1}	3.10×10^{-1}	2.47×10^{-1}	2.20×10^{-1}
TOF (s^{-1})	1.18×10^{-7}	2.14×10^{-9}	1.76×10^{-11}	1.92×10^{-12}	1.06×10^{-8}	1.04×10^{-10}	3.06×10^{-11}

Table B.3: Reaction free energies in eV of various elementary reaction steps in the HDO of Pac on Rh (111) surface at a temperature of 473 K under vapor phase and liquid phase with water and 1, 4-dioxane as solvent, respectively with 10% decrease of the default COSMO Rh cavity being used in the liquid phase calculations.

#	Reaction	Gas		Water		1-4-dioxane	
		ΔG_{rxn}	$\Delta G^{\ddagger}$	$\Delta\Delta G_{rxn}$	$\Delta\Delta G^{\ddagger}$	$\Delta\Delta G_{rxn}$	$\Delta\Delta G^{\ddagger}$
0	CH_3CH_2COOH + * -> CH_3CH_2COOH*	0.41	N/A	-0.01	N/A	-0.05	N/A
1	CH_3CH_2COOH* + 3* -> CH_3CH_2CO*** + OH*	0.08	0.65	-0.05	-0.04	0.06	0.03
2	CH_3CH_2COOH* + 2* -> $CH_3CHCOOH$** + H*	0.03	0.63	-0.04	-0.07	0.03	0.03
3	CH_3CH_2CO*** + 2* -> CH_3CH_2** + CO***	-0.51	1.15	-0.02	0.01	-0.03	0.00
4	CH_3CH_2CO*** -> CH_3CHCO** + H*	-0.11	0.82	-0.01	-0.02	0.01	0.03
5	$CH_3CHCOOH$** + * -> CH_3CHCO** + OH*	-0.06	0.76	-0.02	-0.02	0.05	-0.01
6	$CH_3CHCOOH$** + 3* -> $CH_2CHCOOH$**** + H*	-0.22	0.40	-0.01	-0.01	0.00	0.01
7	$CH_3CHCOOH$** + 2* -> CH_3CCOOH*** + H*	-0.32	0.26	-0.02	-0.02	0.00	-0.01
8	CH_3CHCO** + 4* -> CH_3CH*** + CO***	-0.84	0.66	-0.01	0.04	0.00	-0.01
9	CH_3CHCO** + 3* -> CH_3CCO**** + H*	-0.35	0.45	-0.01	-0.01	-0.03	-0.02
10	CH_3CHCO** + 3* -> CH_2CHCO**** + H*	-0.26	0.62	-0.02	0.00	-0.01	0.02
11	$CH_2CHCOOH$**** + * -> CH_2CHCO**** + OH*	-0.10	0.86	-0.04	-0.01	0.04	0.01
12	$CH_2CHCOOH$**** + * -> $CHCHCOOH$**** + H*	-0.33	0.23	-0.01	-0.01	0.01	0.02
13	CH_3CCOOH*** + 2* -> CH_3CCO**** + OH*	-0.09	0.86	-0.02	-0.01	0.02	0.02
14	CH_3CCO**** + 2* -> CH_3C*** +CO***'	-1.32	0.22	0.00	-0.01	0.01	0.01
15	CH_2CHCO**** + 2* -> CH_2CH*** + CO***	-0.63	0.80	0.01	0.01	-0.01	0.01
16	CH_2CHCO**** + * -> $CHCHCO$**** + H*	-0.06	0.43	0.00	0.00	0.01	0.02
17	$CHCHCOOH$**** + * -> $CHCHCO$**** + OH*	0.17	0.92	-0.03	-0.02	0.04	0.01
18	$CHCHCO$**** + 3* -> $CHCH$**** + CO***	-1.08	0.54	-0.02	0.02	-0.02	-0.03

`

19	$CH_2CH^{***} + 2^* \rightarrow CHCH^{****} + H^*$	-0.51	0.14	-0.04	-0.02	0.01	0.02
20	$CH_2CH_2^{**} + 2^* \rightarrow CH_2CH^{***} + H^*$	-0.10	0.42	0.01	-0.01	-0.02	0.00
21	$CH_2CH^{***} + ^* \rightarrow CH_2C^{***} + H^*$	-0.58	0.04	-0.05	-0.05	0.00	0.01
22	$CH_3C^{***} + ^* \rightarrow CH_2C^{***} + H^*$	0.20	0.85	-0.05	-0.03	-0.01	0.01
23	$CH_3CH^{***} + ^* \rightarrow CH_2CH^{***} + H^*$	-0.05	0.50	0.00	0.00	-0.02	0.01
24	$CH_3CH^{***} + ^* \rightarrow CH_3C^{***} + H^*$	-0.83	0.00	-0.01	0.00	-0.01	-0.01
25	$CH_3CH_2^{**} + 2^* \rightarrow CH_3CH^{***} + H^*$	-0.44	0.71	0.00	-0.02	0.04	0.04
26	$CH_3CH_3^* + 2^* \rightarrow CH_3CH_2^{**} + H^*$	0.09	0.62	0.00	0.00	0.01	0.02
27	$CH_3CH_2^{**} + ^* \rightarrow CH_2CH_2^{**} + H^*$	-0.39	0.31	-0.01	0.01	0.03	0.04
28	$CH_3CH_2COOH^* + 2^* \rightarrow CH_3CH_2COO^{**} + H^*$	-0.63	0.25	-0.01	-0.05	0.00	0.00
29	$CH_3CH_2COO^{**} + ^* \rightarrow CH_3CH_2^{**} + CO_2^*$	0.76	1.70	-0.07	-0.08	0.02	0.05
30	$CH_3CH_2COO^{**} + 2^* \rightarrow CH_3CHCOO^{***} + H^*$	0.32	0.93	-0.10	-0.08	0.03	0.05
31	$CH_3CHCOOH^{**} + 2^* \rightarrow CH_3CHCOO^{***} + H^*$	-0.33	0.42	-0.07	-0.05	0.00	0.00
32	$CH_3CHCOOH^{**} + 3^* \rightarrow CH_3CH^{***} + COOH^{**}$	-0.23	0.93	-0.02	-0.01	0.01	0.02
33	$CH_3CHCOO^{***} + ^* \rightarrow CH_3CH^{***} + CO_2^*$	0.00	0.95	0.02	0.02	0.02	0.02
34	$CH_3CHCOO^{***} + ^* \rightarrow CH_3CCOO^{***} + H^*$	0.07	1.02	0.00	0.03	0.05	0.03
35	$CH_3CCOOH^{***} + ^* \rightarrow CH_3CCOO^{***} + H^*$	0.06	0.83	-0.05	-0.04	0.05	0.03
36	$CH_3CCOOH^{***} + 2^* \rightarrow CH_3C^{***} + COOH^{**}$	-0.74	1.00	0.00	0.01	0.01	0.02
37	$CH_2CHCOOH^{****} + ^* \rightarrow CH_2CH^{***} + COOH^{**}$	-0.06	1.49	-0.01	0.00	-0.01	0.00
38	$CH_3CCOO^{***} + ^* \rightarrow CH_3C^{***} + CO_2^*$	-0.90	0.57	0.02	0.07	-0.04	-0.07
39	$COOH^{**} \rightarrow CO_2^* + H^*$	-0.10	0.71	-0.03	-0.01	0.01	0.00
40	$COOH^{**} + 2^* \rightarrow CO^{***} + OH^*$	-0.67	0.36	-0.01	0.00	0.03	0.00
41	$H_2O^* + ^* \rightarrow OH^* + H^*$	-0.03	0.76	0.00	-0.02	0.01	0.01
42	$CH_3CH_3 + ^* \rightarrow CH_3CH_3^*$	0.57	N/A	0.01	N/A	-0.05	N/A
43	$CH_2CH_2 + 2^* \rightarrow CH_2CH_2^{**}$	-0.10	N/A	-0.01	N/A	-0.01	N/A
44	$H_2O + ^* \rightarrow H_2O^*$	0.37	N/A	-0.01	N/A	0.03	N/A
45	$CO_2 + ^* \rightarrow CO_2^*$	0.68	N/A	-0.11	N/A	0.01	N/A
46	$CHCH + 4^* \rightarrow CHCH^{****}$	-1.78	N/A	-0.05	N/A	-0.01	N/A
47	$CO + 3^* \rightarrow CO^{***}$	-0.89	N/A	-0.07	N/A	-0.01	N/A
48	$H_2 + 2^* \rightarrow H^* + H^*$	-0.48	N/A	0.01	N/A	0.00	N/A
49	$CH_3CHCHO^{***} \rightarrow CH_3CHCO^{**} + H^*$	-0.41	0.12	0.00	-0.01	0.01	0.01
50	$CH_3CHCOH^{***} \rightarrow CH_3CHCO^{**} + H^*$	-0.49	0.99	-0.03	0.01	0.00	-0.02
51	$CH_3CH_2CHO^* + 3^* \rightarrow CH_3CH_2CO^{***} + H^*$	-0.75	0.10	-0.03	-0.01	0.01	0.00
52	$CH_3CH_2COH^* + 3^* \rightarrow CH_3CH_2CO^{***} + H^*$	-0.65	0.25	-0.07	-0.07	-0.02	-0.04
53	$CH_3CH_2CHO^* + 3^* \rightarrow CH_3CHCHO^{***} + H^*$	-0.45	0.21	-0.04	-0.04	0.00	0.02
54	$CH_3CHCH_2O^{***} + ^* \rightarrow CH_3CHCHO^{***} + H^*$	-0.86	0.12	-0.02	-0.02	-0.01	0.00
55	$CH_3CHCHOH^{**} + 2^* \rightarrow CH_3CHCHO^{***} + H^*$	-0.57	0.34	-0.03	-0.01	-0.01	0.00
56	$CH_3CH_2COH^* + 3^* \rightarrow CH_3CHCOH^{***} + H^*$	-0.27	0.66	-0.06	-0.03	-0.01	0.01
57	$CH_3CHCHOH^{**} + 2^* \rightarrow CH_3CHCOH^{***} + H^*$	-0.48	0.29	-0.01	0.01	0.00	0.00
58	$CH_3CH_2CH_2O^* + ^* \rightarrow CH_3CH_2CHO^* + H^*$	-0.25	0.47	-0.01	-0.02	-0.03	-0.01
59	$CH_3CH_2CHOH^* + ^* \rightarrow CH_3CH_2CHO^* + H^*$	-0.37	0.46	0.01	-0.01	0.00	0.00
60	$CH_3CH_2CHOH^* + ^* \rightarrow CH_3CH_2COH^* + H^*$	-0.47	0.26	0.04	0.01	0.02	0.01
61	$CH_3CH_2CH_2O^* + 3^* \rightarrow CH_3CHCH_2O^{***} + H^*$	0.15	0.83	-0.03	-0.06	-0.01	0.00
62	$CH_3CHCH_2OH^{**} + 2^* \rightarrow CH_3CHCH_2O^{***} + H^*$	-0.13	0.51	0.02	-0.02	0.00	0.00
63	$CH_3CH_2CHOH^* + 2^* \rightarrow CH_3CHCHOH^{**} + H^*$	-0.25	0.44	0.00	0.01	0.02	0.04
64	$CH_3CHCH_2OH^{**} + ^* \rightarrow CH_3CHCHOH^{**} + H^*$	-0.42	0.38	0.03	0.02	0.01	0.01
65	$CH_3CH_2CH_2OH^* + ^* \rightarrow CH_3CH_2CH_2O^* + H^*$	-0.28	0.63	-0.02	-0.05	-0.01	-0.02
66	$CH_3CH_2CH_2OH^* + ^* \rightarrow CH_3CH_2CHOH^* + H^*$	-0.17	0.49	-0.04	-0.02	-0.03	0.01
67	$CH_3CH_2CH_2OH^* + 2^* \rightarrow CH_3CHCH_2OH^{**} + H^*$	0.00	0.67	-0.08	-0.08	-0.02	0.00
68	$CH_3CH_2CH_2OH + ^* \rightarrow CH_3CH_2CH_2OH^*$	0.59	N/A	0.03	N/A	-0.01	N/A
69	$CH_3CH_2CHO + ^* \rightarrow CH_3CH_2CHO^*$	0.40	N/A	-0.01	N/A	-0.04	N/A
70	$C_4H_8O_2$ (dioxane) $+ 2^* \rightarrow C_4H_8O_2^{**}$	0.99	N/A	-0.09	N/A	-0.08	N/A

`

Table B.4: Reaction free energies in eV of various elementary reaction steps in the HDO of Pac on Rh (111) surface at a temperature of 473 K under vapor phase and liquid phase with water and 1, 4-dioxane as solvent, respectively with 10% increase of the default COSMO Rh cavity being used in the liquid phase calculations.

#	Reaction	Gas		Water		1-4-dioxane	
		ΔG_{rxn}	$\Delta G^{\ddagger}$	$\Delta\Delta G_{rxn}$	$\Delta\Delta G^{\ddagger}$	$\Delta\Delta G_{rxn}$	$\Delta\Delta G^{\ddagger}$
0	$CH_3CH_2COOH + * \rightarrow CH_3CH_2COOH*$	0.41	N/A	-0.10	N/A	-0.07	N/A
1	$CH_3CH_2COOH* + 3* \rightarrow CH_3CH_2CO*** + OH*$	0.08	0.65	-0.07	-0.05	0.01	-0.01
2	$CH_3CH_2COOH* + 2* \rightarrow CH_3CHCOOH** + H*$	0.03	0.63	-0.03	-0.11	0.03	-0.03
3	$CH_3CH_2CO*** + 2* \rightarrow CH_3CH_2** + CO***$	-0.51	1.15	-0.09	0.00	-0.06	0.00
4	$CH_3CH_2CO*** \rightarrow CH_3CHCO** + H*$	-0.11	0.82	-0.03	-0.05	-0.01	-0.02
5	$CH_3CHCOOH** + * \rightarrow CH_3CHCO** + OH*$	-0.06	0.76	-0.07	-0.02	-0.02	-0.01
6	$CH_3CHCOOH** + 3* \rightarrow CH_2CHCOOH**** + H*$	-0.22	0.40	-0.04	-0.04	-0.02	-0.02
7	$CH_3CHCOOH** + 2* \rightarrow CH_3CCOOH*** + H*$	-0.32	0.26	-0.05	-0.04	-0.05	-0.04
8	$CH_3CHCO** + 4* \rightarrow CH_3CH*** + CO***$	-0.84	0.66	-0.10	0.05	-0.07	0.03
9	$CH_3CHCO** + 3* \rightarrow CH_3CCO**** + H*$	-0.35	0.45	-0.03	-0.03	-0.02	-0.02
10	$CH_3CHCO** + 3* \rightarrow CH_2CHCO**** + H*$	-0.26	0.62	-0.04	-0.05	-0.01	-0.01
11	$CH_2CHCOOH**** + * \rightarrow CH_2CHCO**** + OH*$	-0.10	0.86	-0.07	0.00	-0.01	0.02
12	$CH_2CHCOOH**** + * \rightarrow CHCHCOOH**** + H*$	-0.33	0.23	-0.03	-0.01	-0.02	0.00
13	$CH_3CCOOH*** + 2* \rightarrow CH_3CCO**** + OH*$	-0.09	0.86	-0.05	-0.01	0.01	0.02
14	$CH_3CCO**** + 2* \rightarrow CH_3C*** + CO***'$	-1.32	0.22	-0.05	-0.02	-0.04	-0.01
15	$CH_2CHCO**** + 2* \rightarrow CH_2CH*** + CO***$	-0.63	0.80	-0.04	0.00	-0.04	-0.01
16	$CH_2CHCO**** + * \rightarrow CHCHCO**** + H*$	-0.06	0.43	-0.01	-0.01	0.00	0.00
17	$CHCHCOOH**** + * \rightarrow CHCHCO**** + OH*$	0.17	0.92	-0.05	-0.01	0.01	0.01
18	$CHCHCO**** + 3* \rightarrow CHCH**** + CO***$	-1.08	0.54	-0.09	0.04	-0.07	0.02
19	$CH_2CH*** + 2* \rightarrow CHCH**** + H*$	-0.51	0.14	-0.06	-0.04	-0.03	-0.02
20	$CH_2CH_2** + 2* \rightarrow CH_2CH*** + H*$	-0.10	0.42	0.01	-0.02	0.01	0.01
21	$CH_2CH*** + * \rightarrow CH_2C*** + H*$	-0.58	0.04	-0.08	-0.05	-0.05	-0.04
22	$CH_3C*** + * \rightarrow CH_2C*** + H*$	0.20	0.85	-0.07	-0.08	-0.04	-0.04
23	$CH_3CH*** + * \rightarrow CH_2CH*** + H*$	-0.05	0.50	0.02	-0.01	0.02	0.00
24	$CH_3CH*** + * \rightarrow CH_3C*** + H*$	-0.83	0.00	0.01	0.01	0.01	0.01
25	$CH_3CH_2** + 2* \rightarrow CH_3CH*** + H*$	-0.44	0.71	-0.03	-0.07	-0.01	-0.03
26	$CH_3CH_3* + 2* \rightarrow CH_3CH_2** + H*$	0.09	0.62	0.01	0.01	0.02	0.02
27	$CH_3CH_2** + * \rightarrow CH_2CH_2** + H*$	-0.39	0.31	-0.03	-0.01	-0.01	0.01
28	$CH_3CH_2COOH* + 2* \rightarrow CH_3CH_2COO** + H*$	-0.63	0.25	0.02	-0.05	0.03	-0.02
29	$CH_3CH_2COO** + * \rightarrow CH_3CH_2** + CO_2*$	0.76	1.70	-0.21	-0.14	-0.11	-0.05
30	$CH_3CH_2COO** + 2* \rightarrow CH_3CHCOO*** + H*$	0.32	0.93	-0.17	-0.13	-0.06	-0.05
31	$CH_3CHCOOH** + 2* \rightarrow CH_3CHCOO*** + H*$	-0.33	0.42	-0.11	-0.07	-0.06	-0.05
32	$CH_3CHCOOH** + 3* \rightarrow CH_3CH*** + COOH**$	-0.23	0.93	-0.08	-0.07	-0.04	-0.03
33	$CH_3CHCOO*** + * \rightarrow CH_3CH*** + CO_2*$	0.00	0.95	-0.08	0.00	-0.07	0.00
34	$CH_3CHCOO*** + * \rightarrow CH_3CCOO*** + H*$	0.07	1.02	-0.12	0.01	-0.07	0.01
35	$CH_3CCOOH*** + * \rightarrow CH_3CCOO*** + H*$	0.06	0.83	-0.18	-0.14	-0.07	-0.06
36	$CH_3CCOOH*** + 2* \rightarrow CH_3C*** + COOH**$	-0.74	1.00	-0.02	-0.02	0.01	0.02
37	$CH_2CHCOOH**** + * \rightarrow CH_2CH*** + COOH**$	-0.06	1.49	-0.02	0.00	0.00	0.01
38	$CH_3CCOO*** + * \rightarrow CH_3C*** + CO_2*$	-0.90	0.57	0.05	0.22	0.01	0.11
39	$COOH** \rightarrow CO_2* + H*$	-0.10	0.71	-0.11	-0.09	-0.08	-0.07
40	$COOH** + 2* \rightarrow CO*** + OH*$	-0.67	0.36	-0.08	0.01	-0.05	0.00
41	$H_2O* + * \rightarrow OH* + H*$	-0.03	0.76	0.00	-0.03	0.01	-0.01
42	$CH_3CH_3 + * \rightarrow CH_3CH_3*$	0.57	N/A	-0.01	N/A	-0.01	N/A
43	$CH_2CH_2 + 2* \rightarrow CH_2CH_2**$	-0.10	N/A	-0.03	N/A	0.00	N/A

`

44	H_2O + * -> H_2O*	0.37	N/A	-0.07	N/A	-0.02	N/A
45	CO_2 + * -> CO_2*	0.68	N/A	-0.29	N/A	-0.17	N/A
46	CHCH + 4* -> CHCH****	-1.78	N/A	-0.09	N/A	-0.03	N/A
47	CO + 3* -> CO***	-0.89	N/A	-0.18	N/A	-0.12	N/A
48	H_2 + 2* -> H* + H*	-0.48	N/A	0.01	N/A	0.01	N/A
49	CH_3CHCHO*** -> CH_3CHCO** + H*	-0.41	0.12	-0.01	-0.02	-0.01	-0.01
50	CH_3CHCOH*** -> CH_3CHCO** + H*	-0.49	0.99	-0.04	0.02	-0.01	0.01
51	CH_3CH_2CHO* + 3* -> CH_3CH_2CO*** + H*	-0.75	0.10	-0.04	-0.02	-0.02	-0.03
52	CH_3CH_2COH* + 3* -> CH_3CH_2CO*** + H*	-0.65	0.25	-0.06	-0.06	-0.04	-0.04
53	CH_3CH_2CHO* + 3* -> CH_3CHCHO*** + H*	-0.45	0.21	-0.06	-0.09	-0.02	-0.04
54	CH_3CHCH_2O*** + * -> CH_3CHCHO*** + H*	-0.86	0.12	-0.03	-0.04	-0.02	-0.02
55	$CH_3CHCHOH$** + 2* -> CH_3CHCHO*** + H*	-0.57	0.34	-0.01	0.02	0.00	0.02
56	CH_3CH_2COH* + 3* -> CH_3CHCOH*** + H*	-0.27	0.66	-0.06	-0.05	-0.03	-0.03
57	$CH_3CHCHOH$** + 2* -> CH_3CHCOH*** + H*	-0.48	0.29	0.01	0.05	-0.01	0.02
58	$CH_3CH_2CH_2O$* + * -> CH_3CH_2CHO* + H*	-0.25	0.47	0.00	-0.03	0.02	0.00
59	CH_3CH_2CHOH* + * -> CH_3CH_2CHO* + H*	-0.37	0.46	0.03	0.00	0.03	0.00
60	CH_3CH_2CHOH* + * -> CH_3CH_2COH* + H*	-0.47	0.26	0.05	0.04	0.05	0.03
61	$CH_3CH_2CH_2O$* + 3* -> CH_3CHCH_2O*** + H*	0.15	0.83	-0.02	-0.07	0.02	0.00
62	CH_3CHCH_2OH** + 2* -> CH_3CHCH_2O*** + H*	-0.13	0.51	0.07	0.01	0.05	0.01
63	CH_3CH_2CHOH* + 2* -> $CH_3CHCHOH$** + H*	-0.25	0.44	-0.02	-0.02	0.02	0.01
64	CH_3CHCH_2OH** + * -> $CH_3CHCHOH$** + H*	-0.42	0.38	0.04	0.00	0.03	0.01
65	$CH_3CH_2CH_2OH$* + * -> $CH_3CH_2CH_2O$* + H*	-0.28	0.63	0.00	-0.03	-0.01	-0.04
66	$CH_3CH_2CH_2OH$* + * -> CH_3CH_2CHOH* + H*	-0.17	0.49	-0.03	-0.01	-0.02	0.01
67	$CH_3CH_2CH_2OH$* + 2* -> CH_3CHCH_2OH** + H*	0.00	0.67	-0.09	-0.13	-0.04	-0.07
68	$CH_3CH_2CH_2OH$ + * -> $CH_3CH_2CH_2OH$*	0.59	N/A	-0.04	N/A	-0.02	N/A
69	CH_3CH_2CHO + * -> CH_3CH_2CHO*	0.40	N/A	-0.04	N/A	-0.02	N/A
70	$C_4H_8O_2$ (dioxane) + 2* -> $C_4H_8O_2$**	0.99	N/A	-0.21	N/A	-0.14	N/A

Table B.5: surface coverages of all the surface species (divided by the corresponding number of sites occupied of the adsorption on the surface) under gas and liquid phase conditions at a temperature of 473 K. Results from solvation calculations with ±10% of default COSMO Rh cavity are also shown for water and 1, 4-dioxane, and the surface coverage of free sites is also included and is shown as * in the table.

species	**gas phase**	**water (-10%)**	**water (d)**	**water (+10%)**	**dioxane (-10%)**	**dioxane (d)**	**dioxane (+10%)**
CH_2C***	5.61×10^{-16}	8.39×10^{-14}	1.34×10^{-12}	1.55×10^{-12}	8.39×10^{-16}	5.77×10^{-14}	1.45×10^{-13}
CH_2CH***	2.13×10^{-19}	4.67×10^{-18}	2.02×10^{-17}	2.56×10^{-17}	3.35×10^{-19}	2.97×10^{-18}	5.95×10^{-18}
CH_2CH_2**	2.16×10^{-17}	4.82×10^{-15}	5.93×10^{-14}	1.52×10^{-13}	2.40×10^{-17}	1.38×10^{-15}	6.12×10^{-15}
CH_2CHCO****	6.39×10^{-21}	1.34×10^{-17}	5.83×10^{-16}	8.68×10^{-16}	5.36×10^{-21}	4.66×10^{-18}	2.43×10^{-17}
$CH_2CHCOOH$****	3.61×10^{-11}	5.50×10^{-11}	2.83×10^{-11}	4.74×10^{-11}	3.72×10^{-11}	1.56×10^{-11}	2.33×10^{-11}
CH_3C***	9.25×10^{-11}	3.71×10^{-09}	2.87×10^{-08}	3.33×10^{-08}	1.06×10^{-10}	2.97×10^{-09}	6.76×10^{-09}
CH_3CCO****	1.99×10^{-18}	1.42×10^{-16}	1.40×10^{-15}	2.96×10^{-15}	2.88×10^{-18}	8.85×10^{-17}	3.02×10^{-16}
CH_3CCOO***	4.05×10^{-19}	3.91×10^{-17}	1.73×10^{-15}	8.73×10^{-15}	1.21×10^{-19}	1.93×10^{-17}	1.12×10^{-16}
CH_3CCOOH***	1.08×10^{-11}	2.76×10^{-10}	1.21×10^{-9}	3.08×10^{-9}	1.64×10^{-11}	1.83×10^{-10}	4.91×10^{-10}

`

CH_3CH^{***}	2.28×10^{-17}	7.74×10^{-16}	6.10×10^{-15}	1.11×10^{-14}	2.19×10^{-17}	6.14×10^{-16}	2.06×10^{-15}
$CH_3CH_2^{**}$	5.20×10^{-20}	1.70×10^{-18}	8.05×10^{-18}	1.78×10^{-17}	1.21×10^{-19}	6.67×10^{-19}	1.65×10^{-18}
$CH_3CH_2CH_2O^{*}$	1.43×10^{-18}	1.42×10^{-17}	6.59×10^{-17}	3.22×10^{-16}	2.26×10^{-18}	2.66×10^{-17}	9.43×10^{-17}
$CH_3CH_2CH_2OH^{*}$	2.73×10^{-16}	2.38×10^{-15}	1.84×10^{-14}	1.05×10^{-13}	4.06×10^{-16}	4.54×10^{-15}	1.60×10^{-14}
$CH_3CH_2CHO^{*}$	1.61×10^{-18}	9.47×10^{-18}	2.70×10^{-17}	7.81×10^{-17}	4.49×10^{-18}	1.34×10^{-17}	3.03×10^{-17}
$CH_3CH_2CHOH^{*}$	2.67×10^{-12}	1.32×10^{-11}	2.25×10^{-11}	3.40×10^{-11}	8.43×10^{-12}	1.61×10^{-11}	2.08×10^{-11}
$CH_3CH_2CO^{***}$	4.72×10^{-9}	2.02×10^{-8}	4.41×10^{-8}	5.94×10^{-8}	4.24×10^{-9}	1.10×10^{-8}	1.97×10^{-8}
$CH_3CH_2COH^{*}$	3.07×10^{-10}	3.59×10^{-10}	2.93×10^{-10}	6.06×10^{-10}	5.12×10^{-10}	3.80×10^{-10}	4.06×10^{-10}
$CH_3CH_2COO^{**}$	1.07×10^{-3}	2.21×10^{-3}	2.61×10^{-3}	3.07×10^{-3}	3.27×10^{-3}	2.93×10^{-3}	2.61×10^{-3}
$CH_3CH_2COOH^{*}$	2.39×10^{-4}	6.62×10^{-4}	2.45×10^{-3}	6.23×10^{-3}	8.20×10^{-4}	2.68×10^{-3}	3.44×10^{-3}
$CH_3CH_3^{*}$	9.29×10^{-27}	2.46×10^{-25}	7.59×10^{-25}	2.82×10^{-24}	4.73×10^{-26}	1.12×10^{-25}	3.57×10^{-25}
$CH_3CHCH_2O^{***}$	3.04×10^{-23}	3.01×10^{-22}	5.99×10^{-22}	9.24×10^{-22}	2.11×10^{-23}	1.49×10^{-22}	2.74×10^{-22}
$CH_3CHCH_2OH^{**}$	1.04×10^{-19}	8.08×10^{-19}	1.10×10^{-18}	1.23×10^{-18}	2.47×10^{-19}	3.04×10^{-19}	4.16×10^{-19}
CH_3CHCHO^{***}	1.52×10^{-15}	1.79×10^{-14}	3.41×10^{-14}	5.52×10^{-14}	1.32×10^{-15}	5.45×10^{-15}	1.20×10^{-14}
$CH_3CHCHOH^{**}$	2.28×10^{-17}	2.46×10^{-16}	6.14×10^{-16}	9.88×10^{-16}	4.50×10^{-17}	1.34×10^{-16}	2.30×10^{-16}
CH_3CHCO^{**}	2.62×10^{-16}	8.69×10^{-14}	2.98×10^{-12}	8.99×10^{-12}	2.16×10^{-16}	6.29×10^{-14}	2.84×10^{-13}
CH_3CHCOH^{***}	3.39×10^{-14}	8.87×10^{-14}	3.57×10^{-14}	3.01×10^{-14}	5.33×10^{-14}	2.75×10^{-14}	3.21×10^{-14}
CH_3CHCOO^{***}	2.43×10^{-15}	1.58×10^{-14}	1.90×10^{-14}	2.69×10^{-14}	2.69×10^{-15}	3.18×10^{-15}	4.05×10^{-15}
$CH_3CHCOOH^{**}$	1.64×10^{-12}	1.62×10^{-11}	4.21×10^{-11}	9.91×10^{-11}	2.61×10^{-12}	8.19×10^{-12}	1.48×10^{-11}
$CHCH^{****}$	2.35×10^{-18}	2.52×10^{-16}	1.79×10^{-15}	1.88×10^{-15}	2.89×10^{-18}	9.07×10^{-17}	2.29×10^{-16}
$CHCHCO^{****}$	1.97×10^{-16}	2.82×10^{-14}	1.58×10^{-13}	1.49×10^{-13}	8.79×10^{-17}	4.19×10^{-15}	1.55×10^{-14}
$CHCHCOOH^{****}$	9.85×10^{-16}	8.71×10^{-14}	9.11×10^{-13}	3.04×10^{-12}	1.05×10^{-15}	3.70×10^{-14}	1.87×10^{-13}
CO^{***}	1.61×10^{-1}	2.23×10^{-1}	2.68×10^{-1}	2.76×10^{-1}	1.65×10^{-1}	2.30×10^{-1}	2.46×10^{-1}
CO_2^{*}	4.44×10^{-26}	1.55×10^{-24}	1.73×10^{-23}	7.75×10^{-23}	1.12×10^{-25}	1.81×10^{-24}	7.70×10^{-24}
$COOH^{**}$	1.85×10^{-12}	3.72×10^{-12}	3.54×10^{-13}	3.14×10^{-13}	5.72×10^{-12}	9.97×10^{-13}	9.21×10^{-13}
H^{*}	5.00×10^{-1}	3.17×10^{-1}	1.81×10^{-1}	1.56×10^{-1}	4.84×10^{-1}	2.92×10^{-1}	2.48×10^{-1}
H_2O^{*}	8.76×10^{-16}	9.21×10^{-15}	4.32×10^{-14}	1.98×10^{-13}	5.31×10^{-16}	5.40×10^{-15}	2.35×10^{-14}
dioxane	8.42×10^{-11}	2.29×10^{-9}	8.64×10^{-9}	3.56×10^{-8}	5.42×10^{-10}	2.37×10^{-9}	6.70×10^{-9}
OH^{*}	9.90×10^{-11}	1.86×10^{-10}	2.11×10^{-10}	4.05×10^{-10}	1.17×10^{-10}	1.52×10^{-10}	2.66×10^{-10}
*	1.50×10^{-2}	9.57×10^{-3}	5.68×10^{-3}	4.23×10^{-3}	1.36×10^{-2}	8.30×10^{-3}	6.85×10^{-3}

`

Table B.6: Degrees of selectivity control of key species (including surface species and transition states) that have significant impact on the DCN path selectivity under gas and liquid phase conditions at a temperature of 473 K. Results from solvation calculations with ±10% of default COSMO Rh cavity are also shown for water and 1, 4-dioxane, and N/A in the table denotes that the value is smaller than 0.01.

species	**gas phase**	**water (-10%)**	**water (d)**	**water (+10%)**	**dioxane (-10%)**	**dioxane (d)**	**dioxane (+10%)**
Step 4	0.81	0.37	0.14	0.10	0.81	0.39	0.26
Step 9	N/A	N/A	0.02	0.01	N/A	N/A	N/A
Step 51	-0.43	-0.32	-0.38	-0.31	-0.41	-0.47	-0.46
Step 52	-0.42	-0.54	-0.56	-0.64	-0.31	-0.45	-0.48
Step 53	0.16	0.58	0.81	0.84	0.15	0.56	0.70
Step 60	-0.01	-0.02	N/A	N/A	-0.02	N/A	N/A
Step 66	-0.10	-0.09	-0.02	N/A	-0.22	-0.04	-0.02
H*	-1.13	-0.36	-0.04	-0.03	-1.10	-0.39	-0.19
CO***	0.53	0.13	N/A	N/A	0.41	0.18	0.09
CH_3CH_2COO**	0.02	0.03	0.02	0.03	0.06	0.03	0.03
CH_3CH_2COOH*	N/A	N/A	0.01	0.03	N/A	0.02	0.02

Table B.7: Reaction energies in eV (without zero-point energy correction) of various elementary reaction steps in the HDO of Pac on Rh (111) surface under vapor phase.

#	Reaction	ΔE_{rxn}	$\Delta E^{‡}$
0	CH_3CH_2COOH + * -> CH_3CH_2COOH*	-2.94	N/A
1	CH_3CH_2COOH* + 3* -> CH_3CH_2CO*** + OH*	0.20	0.70
2	CH_3CH_2COOH* + 2* -> $CH_3CHCOOH$** + H*	0.16	0.77
3	CH_3CH_2CO*** + 2* -> CH_3CH_2** + CO***	-0.36	1.23
4	CH_3CH_2CO*** -> CH_3CHCO** + H*	0.00	0.99
5	$CH_3CHCOOH$** + * -> CH_3CHCO** + OH*	0.04	0.87
6	$CH_3CHCOOH$** + 3* -> $CH_2CHCOOH$**** + H*	-0.15	0.49
7	$CH_3CHCOOH$** + 2* -> CH_3CCOOH*** + H*	-0.28	0.36
8	CH_3CHCO** + 4* -> CH_3CH*** + CO***	-0.63	0.70
9	CH_3CHCO** + 3* -> CH_3CCO**** + H*	-0.17	0.58
10	CH_3CHCO** + 3* -> CH_2CHCO**** + H*	-0.20	0.76
11	$CH_2CHCOOH$**** + * -> CH_2CHCO**** + OH*	-0.01	0.99
12	$CH_2CHCOOH$**** + * -> $CHCHCOOH$**** + H*	-0.19	0.35
13	CH_3CCOOH*** + 2* -> CH_3CCO**** + OH*	0.15	1.04
14	CH_3CCO**** + 2* -> CH_3C*** +CO***'	-1.24	0.27
15	CH_2CHCO**** + 2* -> CH_2CH*** + CO***	-0.45	0.92
16	CH_2CHCO**** + * -> $CHCHCO$**** + H*	0.10	0.58
17	$CHCHCOOH$**** + * -> $CHCHCO$**** + OH*	0.28	1.01
18	$CHCHCO$**** + 3* -> $CHCH$**** + CO***	-0.98	0.62
19	CH_2CH*** + 2* -> $CHCH$**** + H*	-0.43	0.21
20	CH_2CH_2** + 2* -> CH_2CH*** + H*	0.05	0.57
21	CH_2CH*** + * -> CH_2C*** + H*	-0.50	0.11
22	CH_3C*** + * -> CH_2C*** + H*	0.26	0.91

23	$CH_3CH^{***} + * \rightarrow CH_2CH^{***} + H^*$	-0.01	0.56
24	$CH_3CH^{***} + * \rightarrow CH_3C^{***} + H^*$	-0.78	0.01
25	$CH_3CH_2^{**} + 2^* \rightarrow CH_3CH^{***} + H^*$	-0.27	0.90
26	$CH_3CH_3^* + 2^* \rightarrow CH_3CH_2^{**} + H^*$	0.15	0.68
27	$CH_3CH_2^{**} + * \rightarrow CH_2CH_2^{**} + H^*$	-0.34	0.42
28	$CH_3CH_2COOH^* + 2^* \rightarrow CH_3CH_2COO^{**} + H^*$	-0.53	0.45
29	$CH_3CH_2COO^{**} + * \rightarrow CH_3CH_2^{**} + CO_2^*$	0.96	1.85
30	$CH_3CH_2COO^{**} + 2^* \rightarrow CH_3CHCOO^{***} + H^*$	0.46	1.10
31	$CH_3CHCOOH^{**} + 2^* \rightarrow CH_3CHCOO^{***} + H^*$	-0.23	0.59
32	$CH_3CHCOOH^{**} + 3^* \rightarrow CH_3CH^{***} + COOH^{**}$	-0.08	1.00
33	$CH_3CHCOO^{***} + * \rightarrow CH_3CH^{***} + CO_2^*$	0.23	1.08
34	$CH_3CHCOO^{***} + * \rightarrow CH_3CCOO^{***} + H^*$	0.23	1.26
35	$CH_3CCOOH^{***} + * \rightarrow CH_3CCOO^{***} + H^*$	0.29	1.12
36	$CH_3CCOOH^{***} + 2^* \rightarrow CH_3C^{***} + COOH^{**}$	-0.58	1.15
37	$CH_2CHCOOH^{****} + * \rightarrow CH_2CH^{***} + COOH^{**}$	0.06	1.62
38	$CH_3CCOO^{***} + * \rightarrow CH_3C^{***} + CO_2^*$	-0.78	0.64
39	$COOH^{**} \rightarrow CO_2^* + H^*$	0.08	0.97
40	$COOH^{**} + 2^* \rightarrow CO^{***} + OH^*$	-0.51	0.46
41	$H_2O^* + * \rightarrow OH^* + H^*$	0.01	0.91
42	$CH_3CH_3 + * \rightarrow CH_3CH_3^*$	-2.15	N/A
43	$CH_2CH_2 + 2^* \rightarrow CH_2CH_2^{**}$	-2.29	N/A
44	$H_2O + * \rightarrow H_2O^*$	-0.91	N/A
45	$CO_2 + * \rightarrow CO_2^*$	-0.32	N/A
46	$CHCH + 4^* \rightarrow CHCH^{****}$	-3.21	N/A
47	$CO + 3^* \rightarrow CO^{***}$	-1.76	N/A
48	$H_2 + 2^* \rightarrow H^* + H^*$	-1.35	N/A
49	$CH_3CHCHO^{***} \rightarrow CH_3CHCO^{**} + H^*$	-0.31	0.21
50	$CH_3CHCOH^{***} \rightarrow CH_3CHCO^{**} + H^*$	-0.38	1.17
51	$CH_3CH_2CHO^* + 3^* \rightarrow CH_3CH_2CO^{***} + H^*$	-0.58	0.18
52	$CH_3CH_2COH^* + 3^* \rightarrow CH_3CH_2CO^{***} + H^*$	-0.47	0.46
53	$CH_3CH_2CHO^* + 3^* \rightarrow CH_3CHCHO^{***} + H^*$	-0.27	0.39
54	$CH_3CHCH_2O^{***} + * \rightarrow CH_3CHCHO^{***} + H^*$	-0.68	0.28
55	$CH_3CHCHOH^{**} + 2^* \rightarrow CH_3CHCHO^{***} + H^*$	-0.41	0.56
56	$CH_3CH_2COH^* + 3^* \rightarrow CH_3CHCOH^{***} + H^*$	-0.09	0.82
57	$CH_3CHCHOH^{**} + 2^* \rightarrow CH_3CHCOH^{***} + H^*$	-0.34	0.45
58	$CH_3CH_2CH_2O^* + * \rightarrow CH_3CH_2CHO^* + H^*$	-0.13	0.70
59	$CH_3CH_2CHOH^* + * \rightarrow CH_3CH_2CHO^* + H^*$	-0.26	0.66
60	$CH_3CH_2CHOH^* + * \rightarrow CH_3CH_2COH^* + H^*$	-0.37	0.41
61	$CH_3CH_2CH_2O^* + 3^* \rightarrow CH_3CHCH_2O^{***} + H^*$	0.28	1.04
62	$CH_3CHCH_2OH^{**} + 2^* \rightarrow CH_3CHCH_2O^{***} + H^*$	0.00	0.73
63	$CH_3CH_2CHOH^* + 2^* \rightarrow CH_3CHCHOH^{**} + H^*$	-0.13	0.57
64	$CH_3CHCH_2OH^{**} + * \rightarrow CH_3CHCHOH^{**} + H^*$	-0.27	0.54
65	$CH_3CH_2CH_2OH^* + * \rightarrow CH_3CH_2CH_2O^* + H^*$	-0.17	0.82
66	$CH_3CH_2CH_2OH^* + * \rightarrow CH_3CH_2CHOH^* + H^*$	-0.04	0.67
67	$CH_3CH_2CH_2OH^* + 2^* \rightarrow CH_3CHCH_2OH^{**} + H^*$	0.11	0.81
68	$CH_3CH_2CH_2OH + * \rightarrow CH_3CH_2CH_2OH^*$	-3.25	N/A
69	$CH_3CH_2CHO + * \rightarrow CH_3CH_2CHO^*$	-2.87	N/A
70	$C_4H_8O_2$ (dioxane) $+ 2^* \rightarrow C_4H_8O_2^{**}$	-3.19	N/A

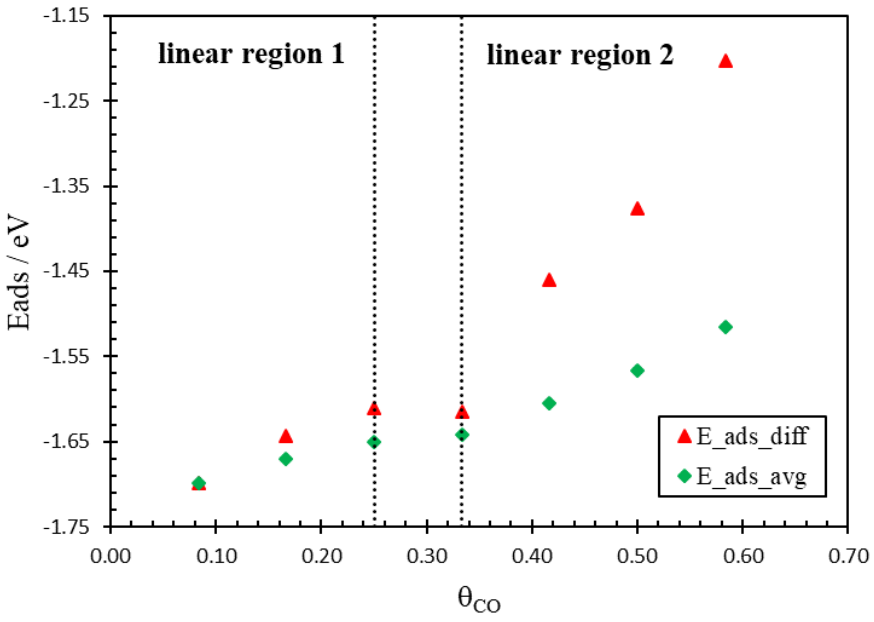

Figure B.1: Coverage dependent adsorption energy for CO adsorption on Rh (111) surface. In the plot, E_ads_avg = ($E_{slab+n\cdot CO}$ - n·E_{CO} - E_{slab}) / n and E_ads_diff = $E_{slab+n\cdot CO}$ - E_{CO} - $E_{slab+\ n-1\cdot CO}$, where n is the total number of CO molecules on the surface, E_{slab} is the total energy of the clean slab, $E_{slab+n\cdot CO}$ is the total energy of the slab with n CO on the surface and E_{CO} is the total energy of the gas phase CO. The surface coverage of CO θ_{CO} used in the plot was calculated by n/N, where N is the total number of surface sites of the surface which is 12 in this work. There is a threshold coverage of θ^0, and below which the adsorption energy of CO on Rh (111) surface is linearly dependent on the surface coverage of CO (linear region 1) while above which there is another linear relationship between the adsorption energy and the surface coverage with different slop (linear region 2).

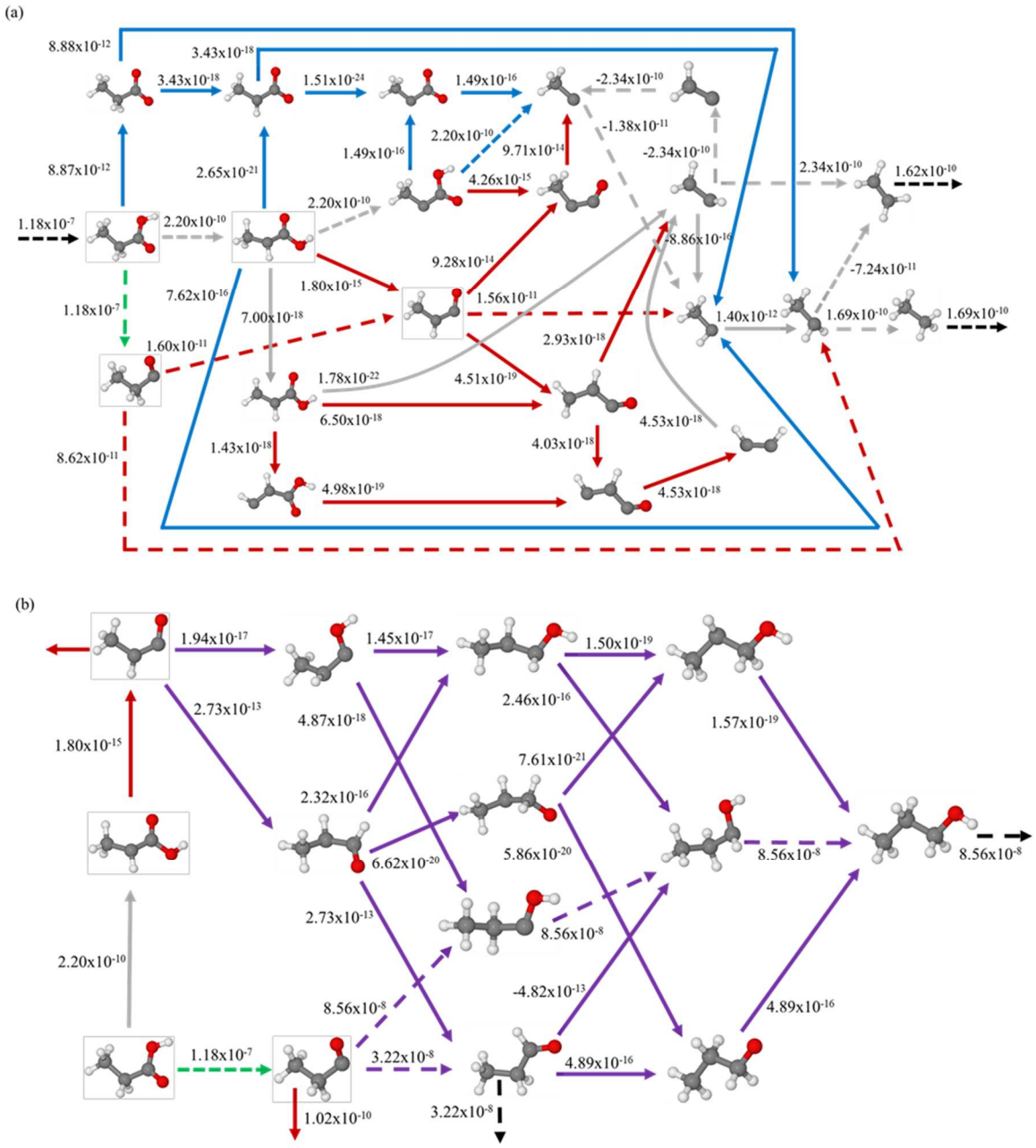

Figure B.2: TOFs (s^{-1}) of various elementary steps in the vapor phase with CO adsorption occupy 1 site on the Rh (111) surface at a temperature of 473 K with the same gas phase partial pressure set as that in the vapor phase model with CO occupy 3 sites on the surface. Dominate pathways are also shown in dashed arrows. TOFs (s^{-1}) of reaction steps involved in DCX and DCN are shown in (a) while the TOFs (s^{-1}) for propanol and propionaldehyde production steps are shown in (b).

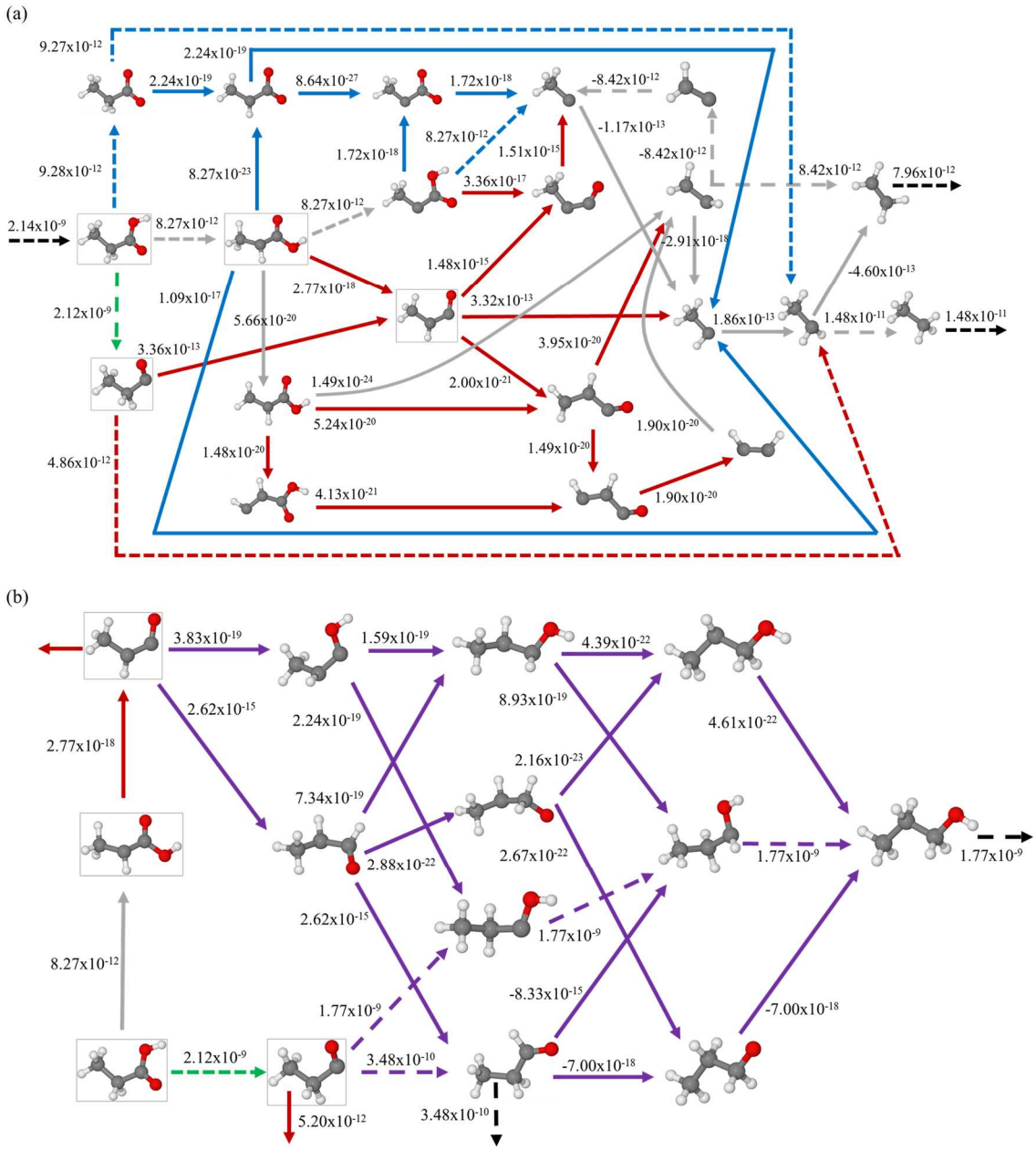

Figure B.3 TOFs (s^{-1}) of various elementary steps in the presence of water as solvent (10% decrease of the default Rh cavity in COSMO calculations) with CO adsorption occupy 1 site on the Rh (111) surface at a temperature of 473 K with the same gas phase partial pressure set as that in the vapor phase. Dominate pathways are also shown in dashed arrows. TOFs (s^{-1}) of reaction steps involved in DCX and DCN are shown in (a) while the TOFs (s^{-1}) for propanol and propionaldehyde production steps are shown in (b).

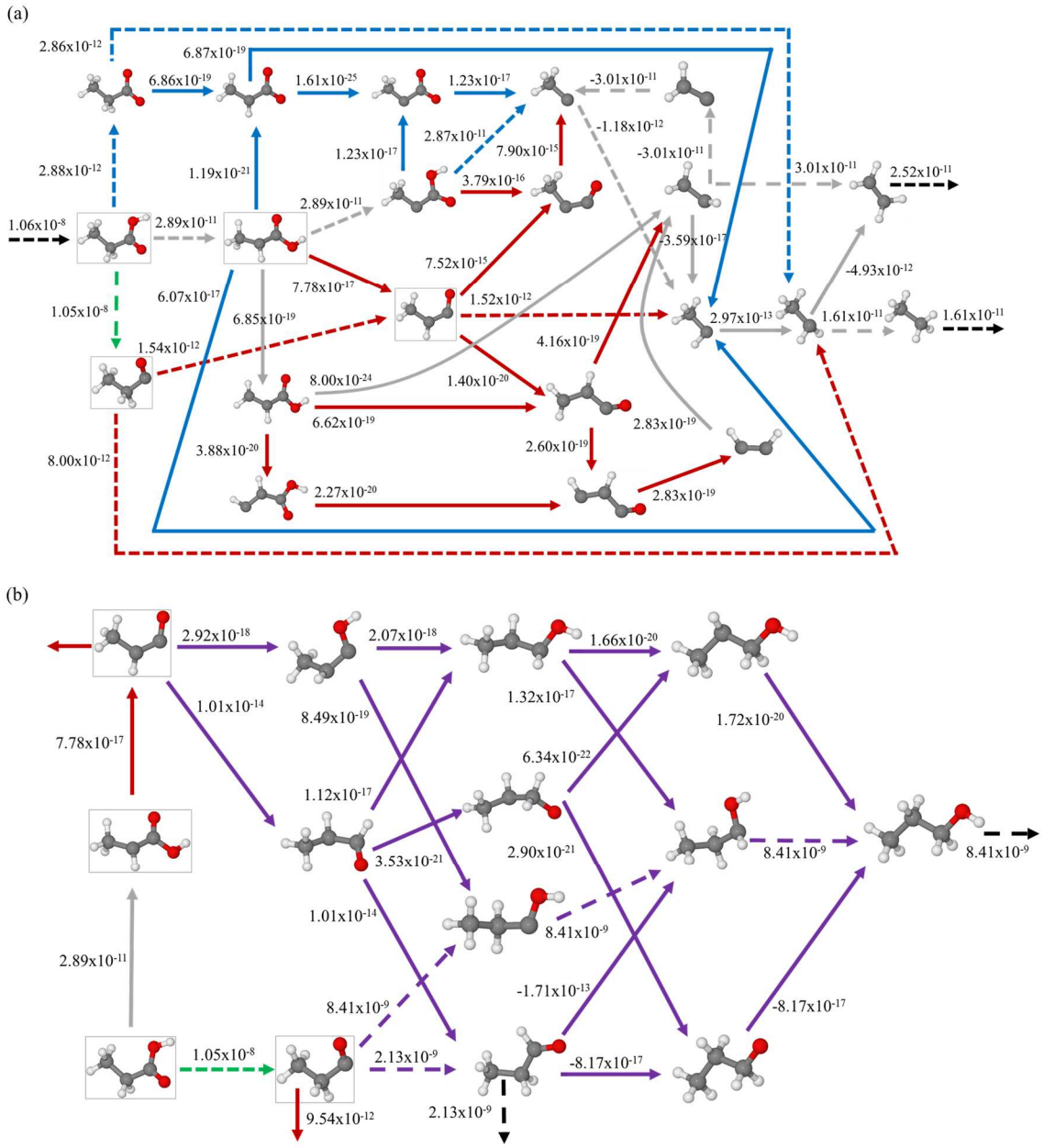

Figure B.4: TOFs (s^{-1}) of various elementary steps in the presence of dioxane as solvent (10% decrease of the default Rh cavity in COSMO calculations) with CO adsorption occupy 1 site on the Rh (111) surface at a temperature of 473 K with the same gas phase partial pressure set as that in the vapor phase. Dominate pathways are also shown in dashed arrows. TOFs (s^{-1}) of reaction steps involved in DCX and DCN are shown in (a) while the TOFs (s^{-1}) for propanol and propionaldehyde production steps are shown in (b).

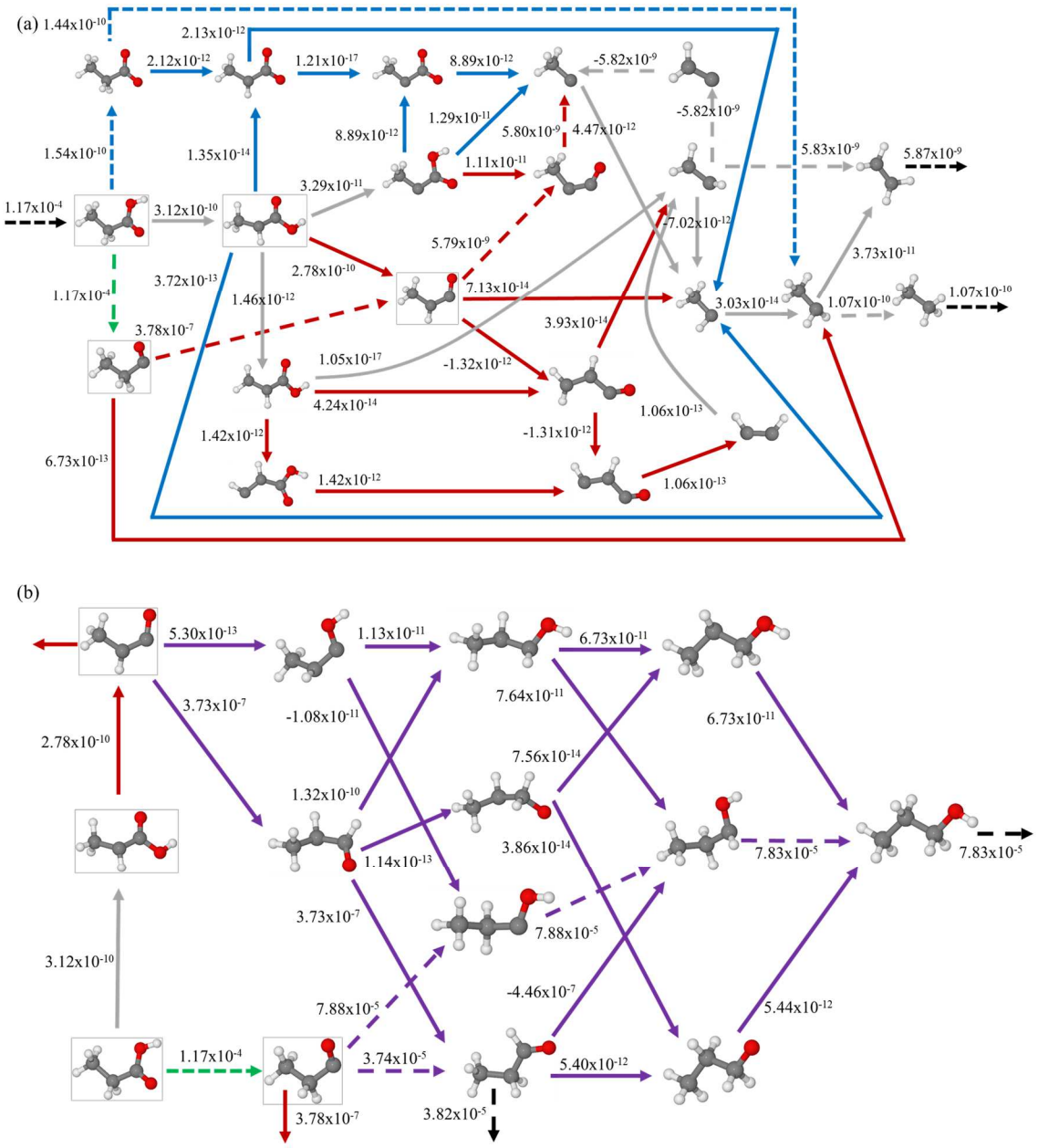

Figure B.5: TOFs (s^{-1}) of various elementary steps in the presence of water as solvent (10% increase of the default Rh cavity in COSMO calculations) with CO adsorption occupy 3 sites on the Rh (111) surface at a temperature of 473 K with the same gas phase partial pressure set as that in the vapor phase. Dominate pathways are also shown in dashed arrows. TOFs (s^{-1}) of reaction steps involved in DCX and DCN are shown in (a) while the TOFs (s^{-1}) for propanol and propionaldehyde production steps are shown in (b).

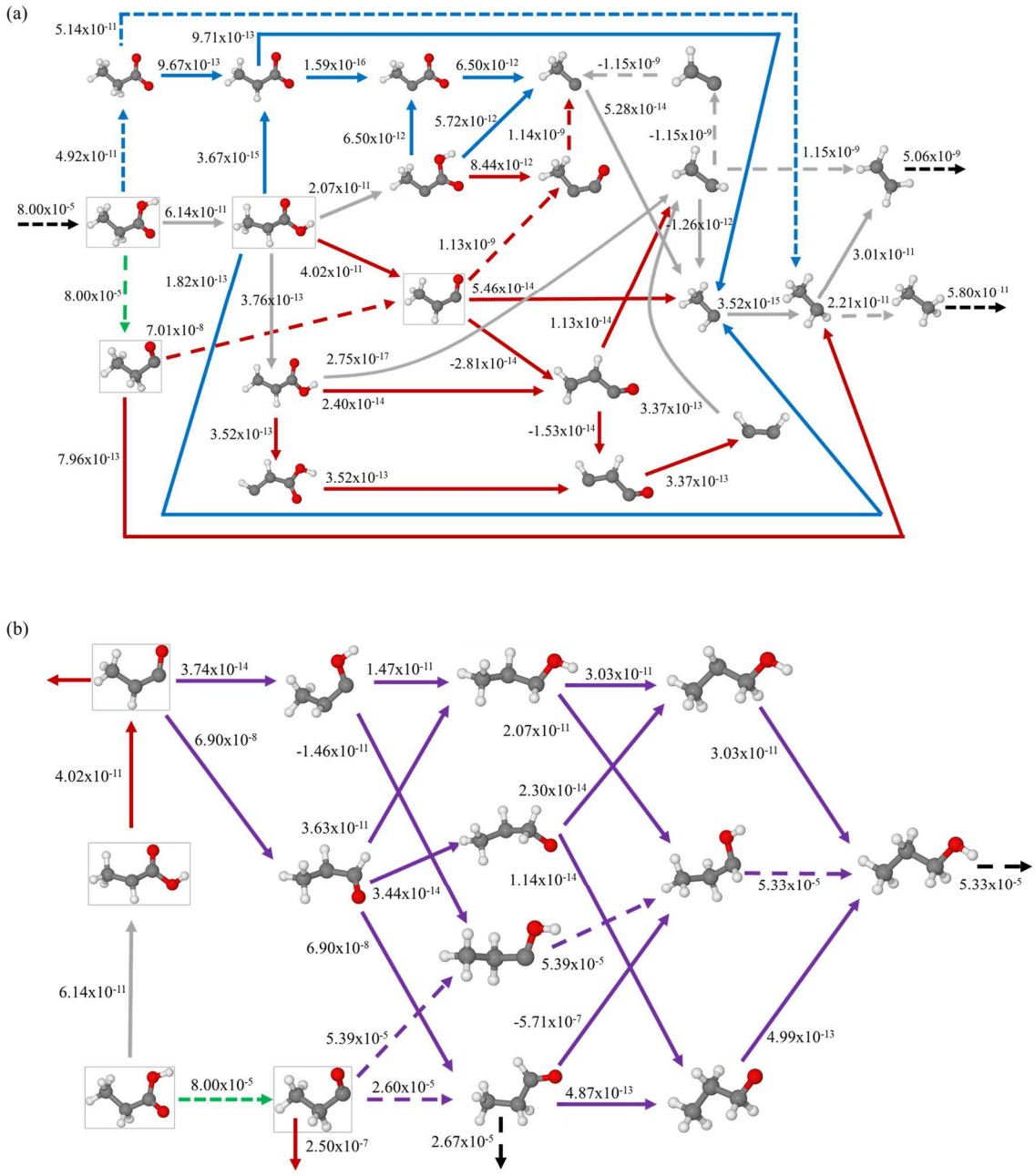

Figure B.6: TOFs (s^{-1}) of various elementary steps in the presence of water as solvent (10% decrease of the default Rh cavity in COSMO calculations) with CO adsorption occupy 3 sites on the Rh (111) surface at a temperature of 473 K with the same gas phase partial pressure set as that in the vapor phase. Dominate pathways are also shown in dashed arrows. TOFs (s^{-1}) of reaction steps involved in DCX and DCN are shown in (a) while the TOFs (s^{-1}) for propanol and propionaldehyde production steps are shown in (b).

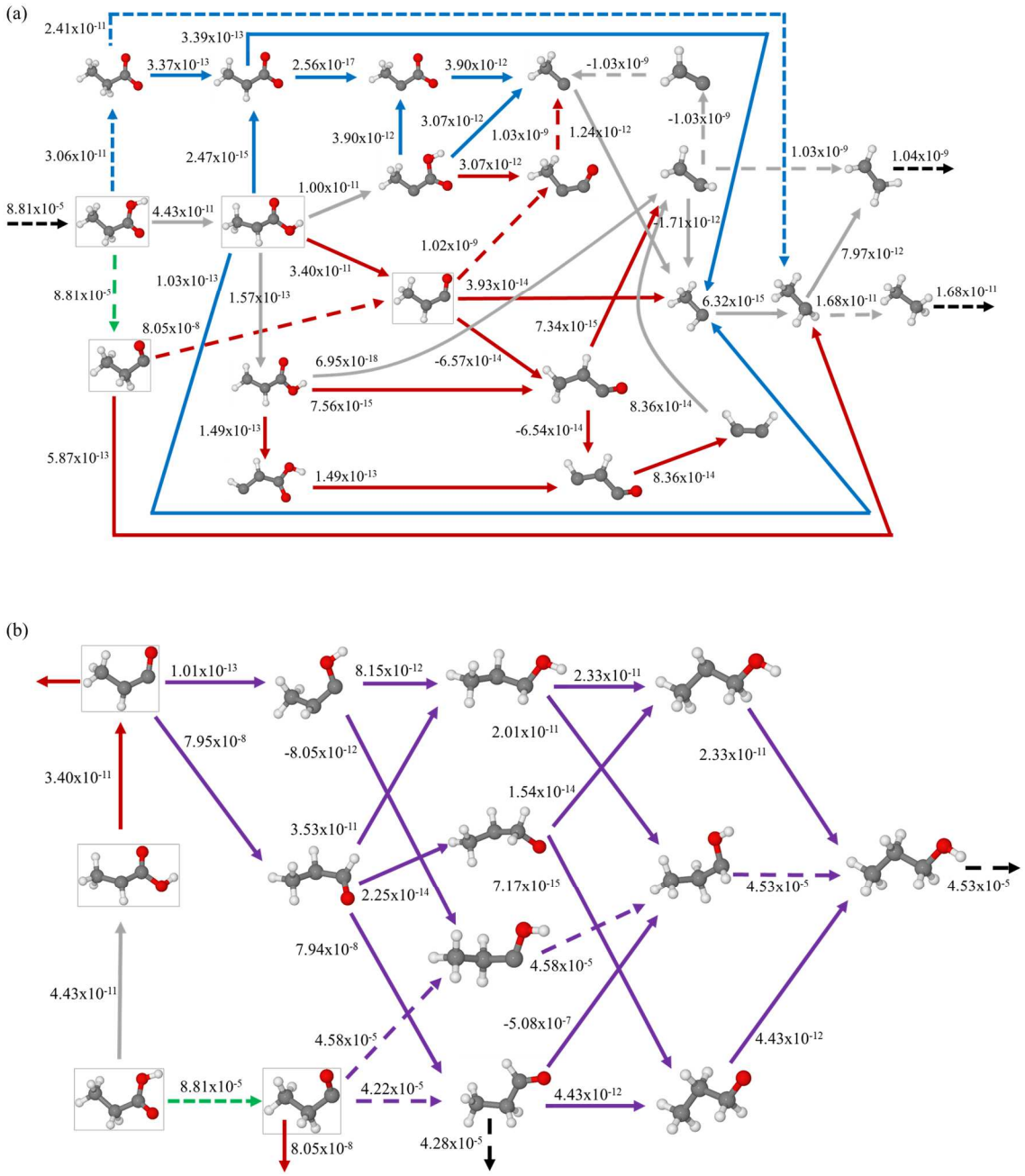

Figure B.7: TOFs (s^{-1}) of various elementary steps in the presence of dioxane as solvent (10% increase of the default Rh cavity in COSMO calculations) with CO adsorption occupy 3 sites on the Rh (111) surface at a temperature of 473 K with the same gas phase partial pressure set as that in the vapor phase. Dominate pathways are also shown in dashed arrows. TOFs (s^{-1}) of reaction steps involved in DCX and DCN are shown in (a) while the TOFs (s^{-1}) for propanol and propionaldehyde production steps are shown in (b).

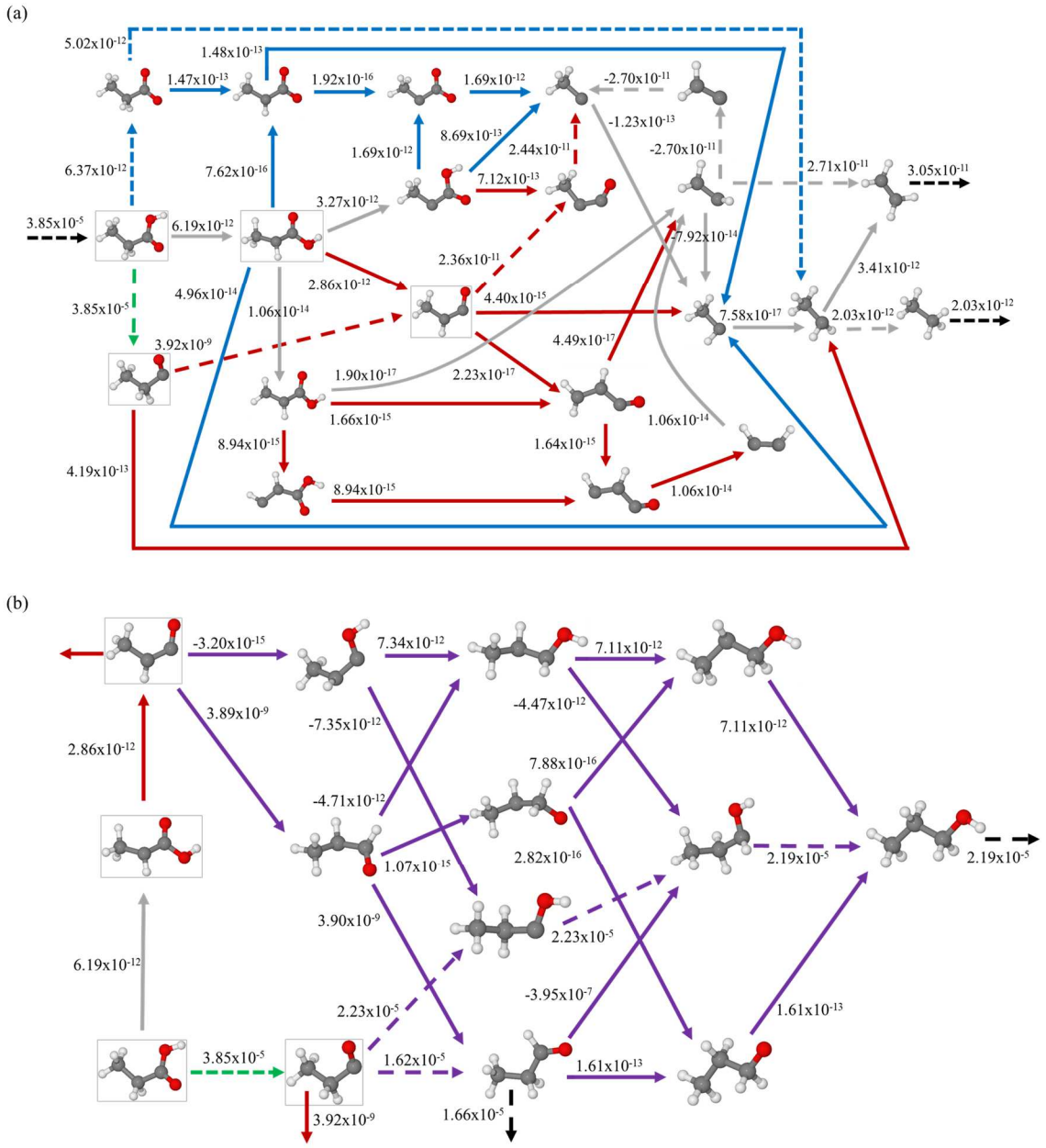

Figure B.8: TOFs (s^{-1}) of various elementary steps in the presence of dioxane as solvent (10% decrease of the default Rh cavity in COSMO calculations) with CO adsorption occupy 3 sites on the Rh (111) surface at a temperature of 473 K with the same gas phase partial pressure set as that in the vapor phase. Dominate pathways are also shown in dashed arrows. TOFs (s^{-1}) of reaction steps involved in DCX and DCN are shown in (a) while the TOFs (s^{-1}) for propanol and propionaldehyde production steps are shown in (b).

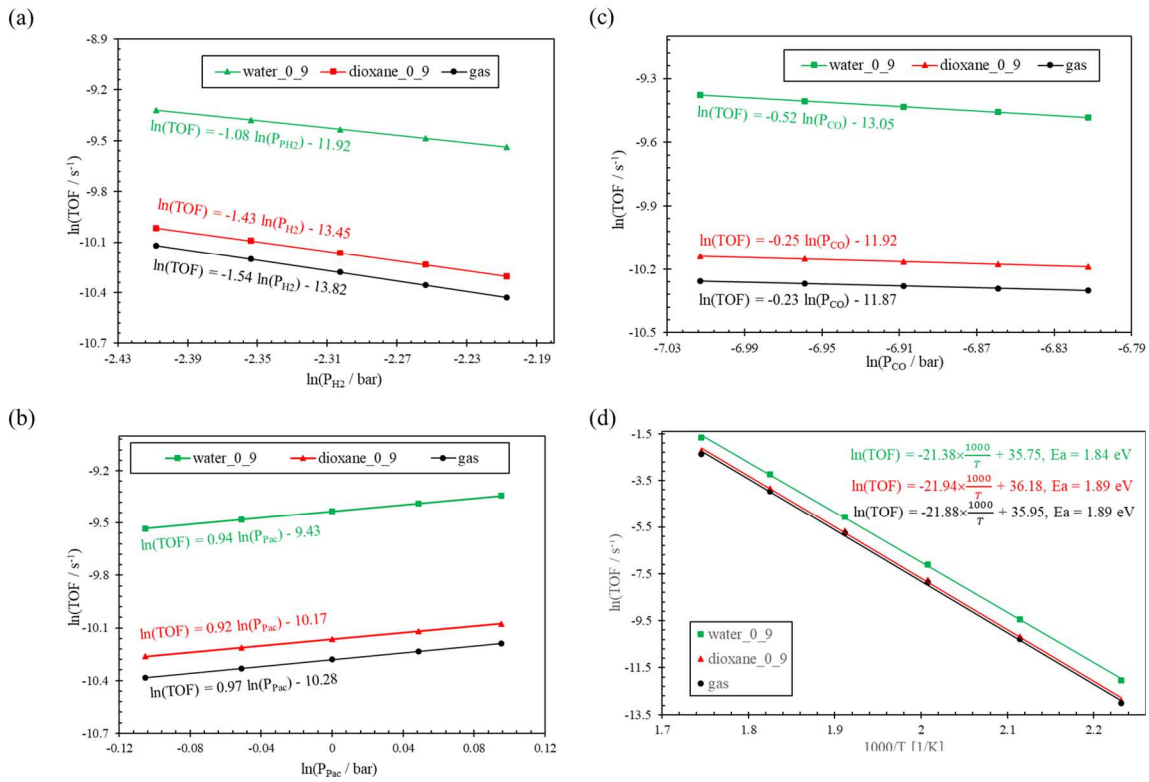

Figure B.9: Reaction orders of (a) H_2, (b) propionic acid and (c) CO at a temperature of 473 K and (d) Arrhenius plot for the HDO of propionic acid in the temperature range of 448 - 573 K with a 10% decrease of the default COSMO Rh cavity in the solvation calculations.

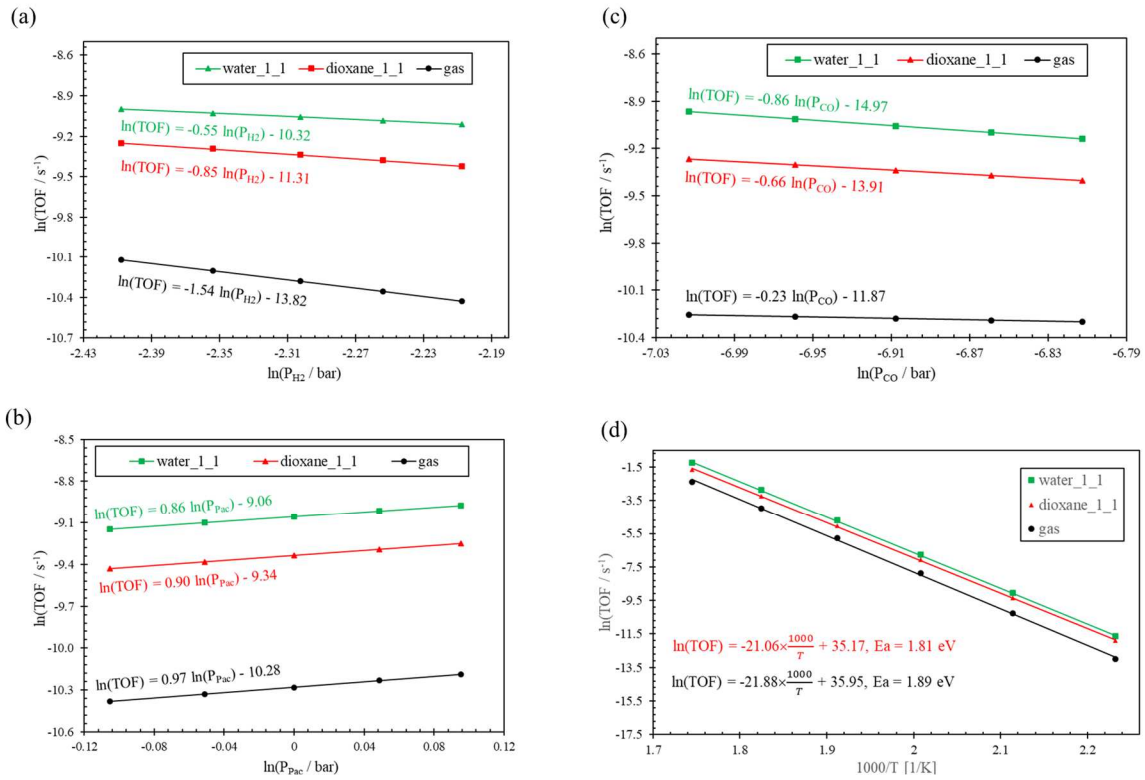

Figure B.10: Reaction orders of (a) H_2, (b) propionic acid and (c) CO at a temperature of 473 K and (d) Arrhenius plot for the HDO of propionic acid in the temperature range of 448 - 573 K with a 10% increase of the default COSMO Rh cavity in the solvation calculation.

`

APPENDIX C

COPYRIGHT PERMISSIONS

Copyright Clearance Center RightsLink®

Home | Help | Email Support | Sign in | Create Account

Unraveling the mechanism of the hydrodeoxygenation of propionic acid over a Pt (1 1 1) surface in vapor and liquid phases

Author:
Wenqiang Yang,Rajadurai Vijay Solomon,Jianmin Lu,Osman Mamun,Jesse Q. Bond,Andreas Heyden

Publication: Journal of Catalysis

Publisher: Elsevier

Date: January 2020

© 2019 Elsevier Inc. All rights reserved.

Please note that, as the author of this Elsevier article, you retain the right to include it in a thesis or dissertation, provided it is not published commercially. Permission is not required, but please ensure that you reference the journal as the original source. For more information on this and on your other retained rights, please visit: https://www.elsevier.com/about/our-business/policies/copyright#Author-rights

BACK CLOSE WINDOW

© 2020 Copyright - All Rights Reserved | Copyright Clearance Center, Inc. | Privacy statement | Terms and Conditions
Comments? We would like to hear from you. E-mail us at customercare@copyright.com